



저작자표시-비영리-변경금지 2.0 대한민국

이용자는 아래의 조건을 따르는 경우에 한하여 자유롭게

- 이 저작물을 복제, 배포, 전송, 전시, 공연 및 방송할 수 있습니다.

다음과 같은 조건을 따라야 합니다:



저작자표시. 귀하는 원저작자를 표시하여야 합니다.



비영리. 귀하는 이 저작물을 영리 목적으로 이용할 수 없습니다.



변경금지. 귀하는 이 저작물을 개작, 변형 또는 가공할 수 없습니다.

- 귀하는, 이 저작물의 재이용이나 배포의 경우, 이 저작물에 적용된 이용허락조건을 명확하게 나타내어야 합니다.
- 저작권자로부터 별도의 허가를 받으면 이러한 조건들은 적용되지 않습니다.

저작권법에 따른 이용자의 권리는 위의 내용에 의하여 영향을 받지 않습니다.

이것은 [이용허락규약\(Legal Code\)](#)을 이해하기 쉽게 요약한 것입니다.

[Disclaimer](#)

MANIPULATION OF RESONANT MODES
AND MODE COUPLING IN
MICROMECHANICAL DEVICE BY
ELECTRICAL FIELD GRADIENT

SUNGWAN CHO

UNDER THE SUPERVISION OF
PROFESSOR YUN DANIEL PARK

A DISSERTATION
SUBMITTED TO THE GRADUATE FACULTY OF
SEOUL NATIONAL UNIVERSITY
IN PARTIAL FULFILLMENT OF THE REQUIREMENTS
FOR THE DEGREE OF
DOCTOR OF PHILOSOPHY

DEPARTMENT OF PHYSICS AND ASTRONOMY
THE GRADUATE SCHOOL OF NATURAL SCIENCES
SEOUL NATIONAL UNIVERSITY
SEOUL, KOREA

AUGUST 2013

© Copyright by Sungwan Cho, 2013.

All rights reserved.

Abstract

Nano- and Micro-mechanical resonator is basic component of NEMS (Nano-ElectroMechanical System) and MEMS (Micro-ElectroMechanical System) which can transduce input signal into different type of output signal or physical energy. Mechanical resonator with high mechanical Quality factor(Q -factor) can have advantages such as sensitive response to external excitation, low energy loss in transduction process. In order to realize micromechanical and nanomechanical resonator with highest Q -factor, much interest have been given to silicon nitride whose mechanical stress can be tuned over 1 GPa. Such a high mechanical stress can also allow operation of mechanical resonator at higher resonant frequency than silicon compatible materials with less or without stress. And to precisely investigate mechanical resonators' dynamics even without actuation or pumping signal while preserving their Q -factor in ambient condition, sensitive optical technique was adopted for non-invasive measurement. In this thesis, mechanical resonators from high-stress silicon nitride with a shape of doubly-clamped beam and square membrane were fabricated with conventional microfabrication process and their resonant responses were investigated by optical measurement technique. Doubly-clamped beam and square membrane mechanical resonator was actuated by electrical field gradient force to oscillate at high frequency with high Q -factor. To amplify the oscillation amplitude for enhancement of optical detection, nonlinear parametric amplification of mechanical resonator was investigated. With $2f$ signal applied with resonant frequency f of mechanical resonator, resonant amplitude was amplified without external amplification techniques. With improved optical and rf measurement technique, thermal oscillations of mechanical resonator was studied. At thermal equilibrium, mechanical component can oscillate at

its structural resonant mode without external actuation and their resonant frequencies were detected. While measuring their resonant frequencies, resonant mode were also reconstructed by mapping power spectral density on the geometry of mechanical resonator. With measured thermal oscillation modes, mechanical resonators' response to mechanical sidebands(red-, blue-) were investigated. By applying their red-detuned sideband which is the frequency equal to the difference of 1st and 2nd resonant mode, resonant amplitude of 1st resonant mode in mechanical resonator was damped and that of 2nd resonant mode was amplified. With blue-detuned sideband, both 1st and 2nd resonant mode was amplified more than 20 dB.

Keywords : Micromechanical resonator, Nanomechanical resonator, Optical measurement, Parametric amplification, Thermal self-oscillation, Mechanical sideband

Contents

Abstract	iii
List of Figures	viii
List of Symbols	xiv
1 Introduction	1
1.1 Outline of Thesis	5
1.2 Chapter Outline	8
2 Doubly-clamped beam and membrane mechanical resonator from stoichiometric silicon nitride	11
2.1 Introduction to NEMS and mechanical resonators	12
2.2 Doubly-clamped mechanical resonator with high-stress stoichiometric silicon nitride	19
2.3 Membrane mechanical resonator with high-stress stoichiometric silicon nitride	26
3 Optical measurement and electrical field gradient actuation technique	35
3.1 Optical measurement of mechanical resonator	36
3.2 Noise in optical measurement	48
3.3 Field gradient actuation of doubly-clamped mechanical oscillator with on-chip electrode	54

3.4	Field gradient actuation of doubly-clamped mechanical oscillator with off-chip electrode	57
3.5	Field gradient actuation of membrane mechanical oscillator with on-chip electrode	60
4	Nonlinear parametric amplification of mechanical resonator with high quality factor by electrical field gradient pumping	63
4.1	Introduction	63
4.2	Mechanical Resonator with double electrode geometry	65
4.3	Actuation and measurement scheme of oscillation in mechanical resonator	70
4.4	Theoretical background for nonlinear parametric oscillation of mechanical resonator	74
4.5	Pumping power dependence of parametric amplification	80
4.6	Phase dependence of parametric amplification	84
5	Observation of thermal self-oscillation with optical technique	87
5.1	Introduction to self-oscillation	87
5.2	Optical measurement of mechanical modes in thermal equilibrium	91
5.3	Construction of power-spectral image of thermal self-oscillation	103
5.4	Investigation of relative displacement of thermal modes in mechanical oscillator driven by Langevin force	109
6	Mode-splitting of thermal oscillatory mode in micromechanical resonator by mechanical sideband	112
6.1	Micromechanical resonator as a signal mixer and mechanical sideband	114
6.2	Control of mechanical system by sideband scheme	117

6.3	Mode-splitting of 1st mode by red-detuned mechanical sideband	120
6.4	Mode-splitting of 2nd mode by red-detuned mechanical sideband	131
7	Mechanical amplification of thermal motion in micromechanical resonator by mechanical sideband	137
7.1	Mechanical amplification of 1st mode by blue-detuned sideband	140
7.2	Mechanical amplification of 2nd mode by blue-detuned sideband	146
8	Summary and outlook	151
	Bibliography	154

List of Figures

2.1	Mechanical system as a transducer between different system . . .	13
2.2	Mechanical resonators for scientific research and applications . . .	14
2.3	Resonant mode of doubly-clamped mechanical resonator	19
2.4	Fundamental resonant frequency vs thickness	22
2.5	Fundamental resonant frequency vs stress	23
2.6	First 4 modes of doubly-clamped mechanical resonator	24
2.7	Scanning electron micrograph of doubly-clamped mechanical resonator	25
2.8	Fundamental vibration mode of membrane calculated by Finite Element Analysis (COMSOL 4.3b)	28
2.9	Superimposed vibrational mode of membrane with index number $(m, n) = (2,1)$ and $(1, 2)$	29
2.10	2nd vibrational mode of membrane calculated by Finite Element Analysis (COMSOL 4.3b)	30
2.11	Scanning electron micrograph of membrane mechanical resonator of 20 micron width	32
2.12	Scanning electron micrograph of membrane mechanical resonator of 40 micron width	33
2.13	Optical image of membrane mechanical resonator of 40 micron width	34

3.1	Optical image of doubly-clamped micromechanical resonator without probing laser (a) and with probing laser (b)	35
3.2	Schematic diagram of optical measurement	37
3.3	Schematic diagram of laser focus on sample and out	40
3.4	Reflectance of silicon nitride (a) and sensitivity of photo- detector (b) to wavelength of light	41
3.5	Design of chamber components	42
3.6	Optical image of sample mount	43
3.7	Optical image of electrical and optical measurement set-up . .	44
3.8	Detailed optical image of sample chamber and laser beam path	44
3.9	Numerical simulation of laser intensity at focal point	45
3.10	Numerical simulation of laser beam intensity on mechanical resonator after reflection	45
3.11	Numerical simulation of laser intensity at focal point	46
3.12	Numerical simulation of laser beam intensity on mechanical resonator after reflection	46
3.13	Numerical simulation of laser intensity at focal point	47
3.14	Numerical simulation of laser beam intensity on mechanical resonator after reflection	47
3.15	Electrical noise without detector and without laser beam . . .	48
3.16	Electrical noise with detector and without laser beam	49
3.17	Electrical noise with detector and laser beam	50
3.18	Electrical noise with detector and laser beam without amplifier	51
3.19	Electrical noise with detector, laser beam and amplifier	52
3.20	Detailed noise with full electrical and optical measurement set-up	53

3.21	Fabrication process for on-chip electrode and mechanical resonator	54
3.22	Numerical simulation of electrical field by on-chip electrode	55
3.23	Resonant motion of doubly-clamped mechanical resonator actuated by on-chip electrode	56
3.24	Fabrication process for off-chip electrode and mechanical resonator	57
3.25	Numerical simulation of electrical field by off-chip electrode	58
3.26	Resonant response of fundamental mode of mechanical resonator to applied pumping rf-signal by off-chip electrode	59
3.27	Fabrication process of membrane resonator with electrodes for electrical field gradient actuation	60
3.28	Numerical simulation of electrical field by on-chip electrode on membrane mechanical resonator	61
3.29	Resonant response of membrane mechanical resonator	62
4.1	Fabrication step for mechanical resonator with 2 sets of in-plane electrode	66
4.2	Cross-sectional and top view of sample	67
4.3	Scanning electron micrograph of fabricated sample	68
4.4	Schematic diagram of excitation of mechanical resonator	70
4.5	Schematic diagram of realized mechanical device and device actuation	71
4.6	Actuation and measurement strategy to excite mechanical oscillator by nonlinear parametric amplification	73
4.7	Gain of nonlinear parametric amplification in parameter space of phase θ and $Q \cdot dk_o/k_o$	76
4.8	Gain of parametric amplification on phase different phase	78

4.9	Deamplification by nonlinear parametric oscillation	79
4.10	Resonant response of mechanical resonator with DC -20 V bias	80
4.11	Quadratic tuning of resonant frequency of mechanical resonator by applied DC voltage	81
4.12	Tuning of resonant frequency of mechanical resonator by change of 1 V DC voltages	82
4.13	Amplification of displacement amplitude of mechanical resonator by pumping power	83
4.14	Pumping power vs amplification gain with different relative phase θ	84
4.15	Relative phase vs amplification gain with different pumping power of $2f$ frequency	86
5.1	Introduction to self-oscillation	89
5.2	Set-up for optical measurement of thermal self-oscillation	91
5.3	Resonant response investigation by driven oscillation	93
5.4	Resonant frequency vs probing laser power	94
5.5	Resonant frequency of 1st mode thermal self-oscillation	96
5.6	Resonant frequency of 2nd mode thermal self-oscillation	97
5.7	Resonant frequency of 3rd mode thermal self-oscillation	98
5.8	Resonant frequency of 4th mode thermal self-oscillation	99
5.9	Resonant frequency of 5th mode thermal self-oscillation	100
5.10	Q-factor vs Probing laser power	102
5.11	Mode image of 1st mode thermal self-oscillation	105
5.12	Mode image of 2nd mode thermal self-oscillation	106
5.13	Mode image of 3rd mode thermal self-oscillation	107
5.14	Mode image of 4th mode thermal self-oscillation	108

5.15	Comparison of relative displacement of thermal self-oscillation by experiment vs theory	109
6.1	Mechanical sideband by thermal self-oscillation	115
6.2	Graphpic illustration for the control of mechanical resonator by optical sideband	118
6.3	Schematic diagram for control of mechanical resonator by red- detuned sideband	120
6.4	Stability of 1st mode in thermal oscillation	125
6.5	Measurement and sideband actuation set-up for sideband con- trol of mechanical modes	126
6.6	Mode-splitting by red-detuned sideband 1 dBm power	127
6.7	Mode-splitting by red-detuned sideband 4 dBm power	128
6.8	Mode-splitting by red-detuned sideband 8 dBm power	129
6.9	Mode-splitting by red-detuned sideband 12 dBm power	130
6.10	Stability of 2nd mode in thermal oscillation	131
6.11	Mode-splitting by red-detuned sideband 1 dBm power	133
6.12	Mode-splitting by red-detuned sideband 4 dBm power	134
6.13	Mode-splitting by red-detuned sideband 8 dBm power	135
6.14	Mode-splitting by red-detuned sideband 12 dBm power	136
7.1	Schematic diagram of amplification by blue-detuned sideband	138
7.2	Amplification by blue-detuned sideband of -4 dBm	142
7.3	Amplification by blue-detuned sideband of -1 dBm	143
7.4	Amplification by blue-detuned sideband of 2 dBm	144
7.5	Amplification by blue-detuned sideband of 4 dBm	145
7.6	Amplification by blue-detuned sideband of -4 dBm	147
7.7	Amplification by blue-detuned sideband of -1 dBm	148

7.8	Amplification by blue-detuned sideband of 2 dBm	149
7.9	Amplification by blue-detuned sideband of 4 dBm	150

List of Symbols

NEMS	Nano-Electro-Mechanical Systems
MEMS	Micro-Electro-Mechanical Systems
Q	Mechanical quality factor
γ_c	Damping rate of cavity
γ_m	Damping rate of mechanical resonant mode
f_r	Frequency of red-detuned sideband
f_b	Frequency of blue-detuned sideband
f_0	Frequency of fundamental or 1st resonant mode of mechanical resonator
f_n	Frequency of n-th resonant mode of mechanical resonator
PD	Photo-Detector
M	Mirror
BS	Beam-Splitter
Un-BS	Unpolarized Beam-Splitter
AR	Anti-Reflective
ω_0	Radius of probing laser beam
$\omega(x)$	Radius of probing laser beam at x
NA	Numerical Aperture
V_{DC}	DC voltage
RF(rf)	Radio Frequency
SA	Spectrum Analyzer
NA	Network Analyzer
PR	Photo-resist
RIE	Reactive Ion Etching

Chapter 1

Introduction

From the invention of transistor and integrated circuits, numerous microfabrication techniques for various micron and sub-micron scale electrical devices such as FET(Field Effect Transistor), diodes, capacitors, and inductors have been developed. Now at the edge of the fabrication technology, the smallest gap in the electrical devices is only 20 nm and expected to become smaller than 10 nm size in near future. This rapid advancement of technology related to materials and fabrication encouraged researchers to realize mechanical devices whose dimension is smaller than what is visible to the eye of human. And researchers have been also able to fashion micron- and nanoscale movable machines like beam, cantilever, and membranes combined with electrical and optical components to control and measure the system which is called as MEMS and NEMS. Mechanical resonator has the most important role in MEMS and NEMS where oscillating component transduce input signal to different types of output signal by coupling with another system like charge [1], spin [2], atom [3], photon momentum [4] et al. In many researches such as gravitational wave detection [5], photon shot noise [6], [7], phonon ground state [8] [9], spin-transfer torque measurement [10], nitrogen vacancy

measurement and control [11], mechanical resonators have shown their potentials in precise measurement and control of of mechanical resonator in basic researches. And also in applications like mechanical memory [12], electro-mechanical amplifier [13], mechanical devices have presented possibilities to replace electrical components and devices.

To fully exploit the mechanical resonator in both basic research and applications with sensitive response to external excitation, low energy loss in transduction process, it is of importance to realize mechanical resonator with high Q -factor. Furthermore, it is also necessary to incorporate precise measurement and control method with mechanical resonator without loss in Q -factor in measurement and control procedure. To suspend the resonating structure with highest mechanical Q -factor, numerous researches have been done on different materials [14], [15], [16] and structures [17]. Recently, stoichiometric silicon nitride became the center of interest to realize mechanical devices with high Q -factor for doubly-clamped beam and membrane resonator. Tension by residual stress in silicon nitride stores elastic energy of structure under vibration and its energy is not dissipated out of the mechanical resonator [18]. Furthermore, tension makes the distribution of mode frequencies to become integer multiples of fundamental frequency, $f_n = n \cdot f_1$ with n indicating the mode number. In this case, mode frequency strongly depends the length of suspended structure and less depends on the other dimension like width and thickness.

With fabrication technique and material for suspended structure with high Q -factor, measurement scheme which do not deteriorate the oscillatory motion of mechanical resonator should be also considered while precisely measuring imperceptible signals. Many technical approaches such as magnetomotive [19], capacitive [20], piezoelectric [21] and optical [22] methods

have been attempted to measure the smallest displacement of mechanical resonator. Among these techniques listed above, optical measurement has some advantages above other techniques; Measurement without additional component on mechanical resonator can prevent damping or dissipation induced by added components. [23] This non-invasive measurement can also be applied to various mechanical resonators with different geometry and from different materials.

In addition to non-invasive measurement of mechanical resonator, actuation scheme which can incorporate driven oscillation of mechanical resonator with high Q -factor. Many techniques including magneto-motive [19], capacitive [22], photothermal [24], piezoelectric [25], and electro-thermal [26] method have been tested but shown limitation for combining high Q -factor with high-frequency operation at ambient condition. Electrical field gradient actuation scheme is based on dielectric gradient forces by local electrical field. Mechanical resonator from dielectric material is polarized by local electrical field. Small RF signal is combined with local electrical field and mechanical resonator is subject to attractive force. [27] [28] This scheme separates the driving component from mechanical resonator, thus, allow ultra-low dissipation from actuation scheme.

For amplification of output signal of mechanical resonator, instead of signal amplification with external amplifier or electrical component, enhancement of displacement has been of high interest. Parametric amplification in mechanical resonator was first demonstrated by Rugar and Grutter's report. [30] Following this seminal research, many different attempts to adopt parametric amplification for small responses of mechanical resonator have been reported. [31] [33] [34] [35] By applying $f_{pumping} = 2 \cdot f_1$ where f_1 is the frequency of fundamental mode and $f_{pumping}$ is the frequency of applied

pumping signal, displacement signal of mechanical resonator can be both amplified and suppressed. This technique can enhance the sensitivity of mechanical resonator's responses and even realize noise squeezing of mechanical resonator. In thermal equilibrium at certain temperature, every movable component can oscillate at its resonant frequencies which is determined its material property and geometry. Although amplitude of displacement of thermal resonant motion is imperceptible, sensitive measurement technique for mechanical resonator can detect motion and additional technique could cool down its motion to mechanical ground state. [1], [8] Optical techniques also has provided sufficient sensitivity to measure the thermal motion of mechanical resonator in coupling with interferometry [36] and optical cavity [37]. As a non-invasive measurement technique, optical method can offer very sensitive and precise measurement of motion in mechanical resonator in thermal equilibrium without limitation of material and geometry of structure. With elaborate optical set-up and electrical devices to amplify and discriminate noises, optical set-up can easily detect thermal motion of mechanical resonator and there responses can be used to reconstruct the mode shape to higher modes.

Mechanical resonator can be act as a signal mixing device. This character enables micro- and nano-mechanical resonator suitable for signal transducer combined with signal mixer [38]. Using this scheme, mechanical sidebands correspond to frequency equals to sum and difference of different mechanical modes. By applying this sideband, we can approach the mechanical mode without directly driving the mechanical mode [39]. With mechanical sideband by thermal motion of mechanical resonator, thermal oscillation modes of resonator are coupled each other by sideband and energy can be transferred from one mechanical mode to another mode which can store energy of

mechanical vibration as a phonon cavity. Amplitude of thermal oscillation is decreases by transferring its vibrationa energy to other mode and amplitude of the other mode rises. Mode splitting in thermal mode can be observed by competition between thermal mode and mechanical sideband which transfers energy to phonon cavity of mechanical resonator,

1.1 Outline of Thesis

In this thesis, firstly, optical measurement of driven oscillation of mechanical resonator with high mechanical Q -factor is investigated. Doubly-clamped type micromechanical resonator and membrane resonators are fabricated from stoichiometric silicon nitride with residual high-stress. By using the commercial finite element analysis package (COMSOL 4.3b and previous versions), mode shapes and their resonant frequencies are estimated and shows good consistency with experimental results. Doubly-clamped beam resonator are driven by electrical field gradient actuation technique. Electrical field gradient actuation technique does not require additional component like electrode on oscillating component and driving source which invite additional damping and degradation of mechanical property like laser. Doubly-clamped mechanical resonators driven by this scheme shows fundamental resonant frequency of approximately 7.0 MHz for 40 micron long samples with mechanical quality factor up to 50,000 in best case. 80 micron long mechanical resonator shows resonant frequency of 3.5 MHz for fundamental mode and Q -factor of 70,000. Resonant frequency of higher modes are also measured to have approximately integer multiples of frequency of their fundamental mode. Furthermore, resonant frequency of mechanical resonator can be easily tuned by DC voltage. Tuning range of resonant frequency is approx-

imately 5 kHz which is about $20 \cdot FWHM$ (Full-Width at Half-Maximum) of resonant spectrum by applying 30 V between electrode. Resonant motion of membrane resonator by electrical field gradient is also investigated. Membrane resonator which is fully suspended and is accessible from both top and bottom side along normal axis to the membrane. Electrode beside the membrane resonator also make it possible to be actuated by field gradient force and resonant frequency of fundamental mode is more than 11 MHz for 40 micron wide square-type membrane.

Nonlinear parametric amplification of doubly-clamped beam resonator with high- Q is also investigated. To amplify infinitesimal displacement signal from mechanical resonator without external amplifier, nonlinear parametric oscillation phenomenon is applied to micromechanical resonator to amplify its motional displacement. Rf signal of $2\omega + \theta$ frequency is applied with ω signal where $\omega = 2\pi \cdot f$ is the resonant frequency of mechanical resonator and θ is the phase difference between signal of 2ω and ω frequency. At relative phase of π , displacement amplitude of mechanical resonator is amplified. To incorporate two signal with different frequency, two sets of electrodes which are isolated from the other electrodes are aligned next to the mechanical resonator. To verify the modulation of resonant frequency with applied DC voltage, resonant frequency shift are investigated. In the linear regime where resonant frequency change linearly to the applied DC voltage, rf-signal with different power is applied to mechanical resonator to excite resonant motion. Optical measurement reveals that resonant amplitude of mechanical resonator driven by rf-signal of both 2ω and ω frequency is amplified with real gain of approximately 9.62 (~ 19 dB) at the relative phase of $\pi/2$ between 2ω pumping and ω driving signal. With the frequency with $\pi = 0$, amplitude of resonant motion is decreased to about half of the original amplitude.

To observe the small displacement amplitude and response of mechanical resonator, thermal motion of mechanical resonator is investigated by optical measurement. Mechanical devices shows resonant motion with periodic driving force by external signal. But at finite temperature, by the random forces from the environment, or Langevin force, mechanical devices can oscillate without periodic excitation. As Langevin force is much smaller than periodic actuation from various signal source such as signal generator, laser and so on. To measure the tiny resonant amplitude of mechanical oscillator by Langevin force with optical technique, additional optical and electrical components are considered to amplify the signal and sensitivity. Amplified optical signal shows higher modes of thermal self-oscillation up to 5th mode at resonant frequency of approximately 17.5 MHz. By mapping the power spectral density of optical signal from the surface of mechanical resonator, modal shape of mechanical resonator at thermal equilibrium can be reconstructed up to their 4th resonant mode. By comparing the relative displacement among the mechanical modes from 1st to 4th, we could verify the validity of optical measurement technique for constructing mode shape and displacement.

Finally, resonant response of mechanical resonator by mechanical sideband is studied. mechanical resonator can operate as a nonlinear circuit device. Thus mechanical resonator can make sideband by mixing input signal with mechanical resonator's resonant frequency. Mechanical resonant modes can be mixing signals to make sideband of upper- and lower-sideband of one mechanical mode. In this case, one mechanical mode is a baseband and the other mode is a mixing signal. The difference frequency of two mechanical mode become a lower-sideband or red-detuned sideband. The frequency equal to the sum of two mechanical mode frequency become a

higher-sideband, or blue-detuned sideband. By using multiple modes of thermal motion in mechanical resonator, we can make use of multiple sidebands around specific mechanical modes. On the other way, we can control the motion of mechanical resonator by applying signal corresponding to mechanical sideband of one mode. When mechanical resonator is in thermal equilibrium without periodic excitation signal, or thermal resonant motion, mechanical sideband is not observable by using optical measurement technique which is used through all experiment covering this thesis. But, Thermal modes of mechanical resonator respond to rf signal which is composed of two frequencies each of which corresponds to different thermal mode of mechanical resonator. By applying red-detuned sideband of fundamental and second mode of thermal oscillation in mechanical oscillator, both fundamental and second mode show mode splitting by sideband and mechanical mode. For fundamental mechanical mode, amplitude of displacement measured by optical technique shows decreases. In case of second mechanical mode, displacement amplitude shows enhancement during mode splitting. With blue-detuned sideband, both fundamental and 2nd mode mode show amplification of displacement amplitude. From analysis of mechanical Q -factor of the fundamental and 2nd thermal mode, difference in gain of amplification or amplification efficiency is attributed to different Q -factor between different modes.

1.2 Chapter Outline

Experimental results and related materials covered by this thesis will be presented as follows

Chapter 2 is a introduction of micro- and nano-mechanical resonator and and description of mechanical resonator under test including fabrication pro-

cess and mechanical properties. Characteristics of resonant motion in doubly-clamped and membrane mechanical resonators such as resonant frequency, mechanical Q -factor, electrical and optical properties which should be considered in experiment is discussed.

Chapter 3 presents the experimental technique for optical measurement and electrical field gradient actuation of mechanical resonator. Free-space optical measurement for precise measurement of higher mode thermal motion and actuation of mechanical resonator with high- Q is introduced.

Chapter 4 investigate the parametric nonlinear oscillation in micromechanical resonator by electrical field gradient pumping. By using mechanical resonator with mechanical high- Q , signal amplification of displacement amplitude is realized by parametric amplification phenomenon. Gain dependence on phase and pumping amplitude is also discussed.

Chapter 5 gives a detailed experimental result on measurement of thermal motion in mechanical oscillator. Free-space optical measurement combined with or without external electrical amplifier resolve the thermal motion of mechanical resonator up to higher mode. Measurement of power spectral density, or noise spectral density is converted to displacement spectral density of mechanical resonator. By mapping mechanical resonator's displacement spectral density on different position on the surface of mechanical resonator at finite temperature. Modal shape of mechanical resonator is reconstructed from mapped power spectral density on the mechanical resonator. Higher mode of thermal self-oscillation in mechanical resonator is also reconstructed. Displacement amplitude of mechanical resonator in different mechanical mode is investigated both in experimentally and theoretically.

Chapter 6 investigate the modal splitting and sideband cooling by mechanical sideband. By using mechanical resonator as a nonlinear signal mixer,

we can assume mechanical sideband. By applying electrical field gradient force at red-detuned sideband ($f_2 - f_1$) sideband, Fundamental mechanical mode and second mechanical mode are coupled. Modal splitting in both fundamental and second mode is investigated.

Chapter 7 shows the experimental results on amplification of displacement amplitude by blue-detuned ($f_2 + f_1$) sideband. Fundamental and second mode are amplified by applied blue-detuned sideband from electrical field gradient actuation technique. Amplification threshold is lowered by thermal motion amplitude and their saturation point is also observed. By measuring the quality factor of fundamental and second mode, some characteristics in mechanical amplification by mechanical sideband is investigated.

Chapter 8 show brief summary of present research and perspective topics from this research. By using the optical measurement technique, resonant motion of mechanical resonator with mechanical high- Q factor is investigated. To elucidate mechanical oscillation with mechanical high- Q factor, electrical field gradient actuation technique is adopted. To amplify the displacement amplitude of mechanical resonator, nonlinear parametric oscillation phenomenon is applied to mechanical resonator under test. To investigate the small oscillation of mechanical resonator without external periodic excitation, external amplification of electrical signal and enhancement of optical technique is done. With optical measurement of thermal motion of mechanical resonator, modal shape of thermal oscillation is reconstructed. By applying electrical field gradient rf signal at the frequency of red- and blue-detuned mechanical sideband, modal splitting, sideband cooling of mechanical mode, and amplification is observed.

Chapter 2

Doubly-clamped beam and membrane mechanical resonator from stoichiometric silicon nitride

The creation of movable structures with dimensions ranging from a few nanometers to a micrometer opened up a new world in basic research and applications. These structures can be realized from various materials such as semiconductors, [40] [41] [42] nanowires, [43] [44] carbon materials [45] [46] [47] and metallic materials [48] [49] [50] by both top-down or bottom-up fabrication processes. Many mechanical resonators combined with electronic, [51] [52] optical, [53] and magnetic functionality [54] provide more sensitive and more accurate control and measurement. Thus these NEMS and mechanical resonators can give us a chance to use future technology such as nanoelectronics, photonic circuits, ultrasensitive sensors, quantum information processing, and so on. To realize these applications in

near future, we should accumulate knowledge for properties of nanomechanical devices and the mechanism behind full control and manipulation of the system. For this goal, we should be able to understand and make use of a measurement and control system. And more efficient actuation and precise measurement should be developed to elucidate conversion of information and energy from object into measurable signals or vice versa.

As a basic and fundamental NEMS and mechanical resonator, doubly-clamped and membrane electromechanical system has been studied from the beginning of NEMS. In this chapter, I'll briefly introduce the recent researches on NEMS and mechanical resonators. Then I'll give an introduction of doubly-clamped mechanical resonator from Si_3N_4 to get higher Q and f_0 . Finally I'll give a presentation for membrane resonator with Si_3N_4 and their oscillatory motions.

2.1 Introduction to NEMS and mechanical resonators¹

NEMS have some intrinsic and interesting properties. Their resonant frequency is in the range of microwave, high Q compared with electrical system at room temperature, very small mass down to \sim femtograms. These properties offered mass sensitivity of single molecule and force sensitivity in the atto-newton range. They also have heat capacities far below a yoctocalorie. These properties shed a light on the ideas of new experiment and applications. Although many researchers have tried to get fully understand and use

¹Numerous research articles and review papers to review NEMS and mechanical resonators have been published. This introductory section is based on two review papers, "Nanoelectromechanical systems" by K. L. Ekinici and M. L. Roukes, published in *Review of scientific instruments* and "Nanomechanical resonators" by Y. S. Greenberg, Y. A. Pashkin and E. Il'ichev, published in *Physics-Uspekhi*

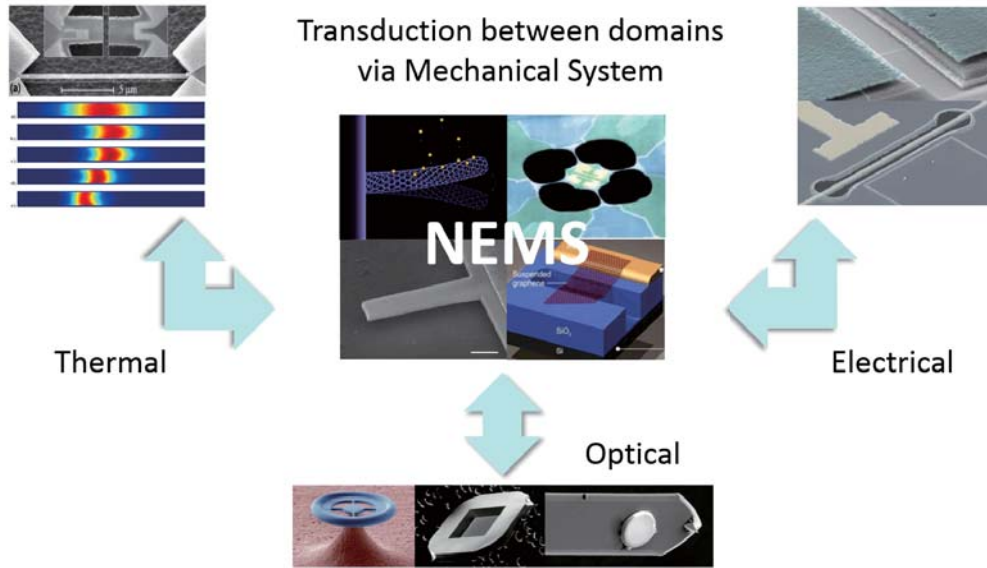


Figure 2.1: Mechanical system as a transducer between different system. Nanoelectromechanical system become versatile transducer between systems with different types of energy.

this device, NEMS, still there are many challenging problems for us to solve to get ability for optimal controlling and engineering these small systems.

Recently, many success and important progress have been achieved in the NEMS. They include nanomechanical resonators ranging in size from tens to hundreds of nanometers and having unique characteristics, The fundamental frequency of NEMS operation varies from MHz to tens of GHz. Meanwhile, a mechanical quality factor, Q , approached to one million for doubly-clamped mechanical resonator even at room temperature. Thus far, the following sensitivities of NEMS operation have been acquired; Displacements sensitivity $\sim 2 \times 10^{-15} \text{ m/Hz}^{1/2}$, [55] mass sensitivity $10^{-18} - 10^{-19} \text{ g/Hz}^{1/2}$, [56] [57] force $10^{-16} \text{ N/Hz}^{1/2}$, [58] electric charge $10^{-1} e/\text{Hz}^{1/2}$ (e is electron charge). [20] From these experimental results, it is probed that the unique properties of NEMS can allow us to realize ultra-sensitive measurement instruments for use in quantum metrology, more precise scanning force

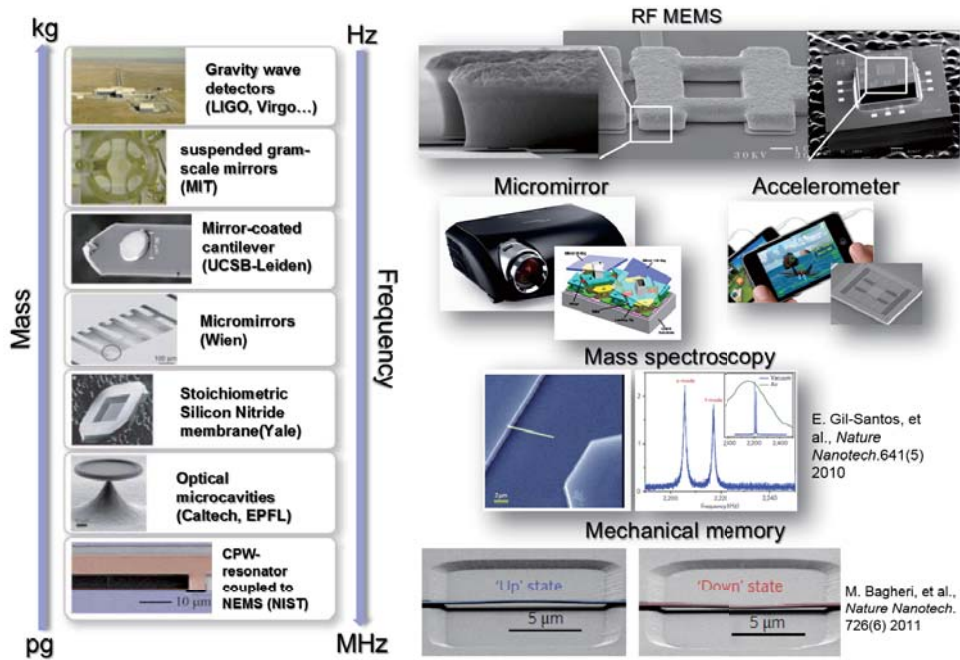


Figure 2.2: Examples of mechanical resonators for scientific research (optomechanics) and applications (switch, sensor, memory, et al.). Mechanical resonators with various dimensions are used to precisely measure the physical quantities. From mechanical resonators to measure gravitational wave (LIGO, Virgo project) to mechanical resonators coupled to CPW (Co-Wlanar Waveguide) of microwave photonic circuit, mechanical resonators with various dimensions are substantial research tool for precise measurement. Mechanical resonators have widely used in applications for mechanical switch, accelerometer and micromirrors. For future applications, mass spectrometer and mechanical memories can be useful applications for their high-sensitivity to mass-load and low-energy consumption for operation

microscopy, [59] magnetic resonance imaging (MRI), [60] etc. Moreover, developments in near future will offer the possibility to elucidate the electronic structure of individual molecules and controlling their motion using NEMS. With these discoveries, there are great amount of ideas and proposals for interesting experiments and NEMS applications, from the search for gravitational waves (LIGO projects et al.) [61] to the manipulation of biomolecule structure (bioMEMS, bioNEMS et al.). [62] At the same time, NEMS researches have raised a number of fundamental questions which should be

solved for further advancement or improvement. They are including technological issues (reproducibility, material properties at surface and bulk state) and development of more precise measurement tools to study the mechanics and properties of micro- and nano-scale particles. From the theoretical standpoint, it is important to analyze the applicability of the continuum mechanics of macroscopic objects to the calculation of mechanical characteristics of these miniature resonator.

While focusing our concern solely on the mechanical components, nanomechanical resonators also have drawn attention because they can become more sensitive and energy-saving detectors than their micromechanical analogs. The integration of an nanomechanical resonator with SET (Single Electron Transistor) [63] [64], superconducting circuits, [65] [66] charge and flux qubits, [67] [68] CPW resonators [69] give us great possibilities to investigate into the dynamics of integrated electro-mechanical systems. Historically, the first nanomechanical resonator in the radio-frequency regime was made from single-crystal silicon and their resonant frequency of fundamental mode was about 70 MHz with $Q = 1.8 \times 10^4$. [70] Another silicon nanomechanical resonator with reduced dimensions showed operation at frequency of 380 MHz. [71] However, Q -factors of these nanomechanical resonators have shown smaller values than expected. Specifically, it was shown that an increase of surface-to-volume ratio can decrease the Q -factor in operation of nanomechanical resonator. For high-frequency operation of nanomechanical resonator in the GHz range, silicon carbide-based nanomechanical resonator operated at the fundamental resonant frequency above 1 GHz with $Q \sim 10^4$. [72] Nanomechanical resonators from various different materials have been also studied for the same purpose (high-frequency, high- Q factor) and they include gallium arsenide (GaAs), [73] silicon nitride Si_3N_4 , [74],

aluminium nitride (AlN), [75] nanocrystalline diamond (NCD), [76] carbon nanotube (CNT), [77] and graphene. [78] [79]

To present the theoretical calculation of resonant response of mechanical resonator, we describe the motion of doubly-clamped mechanical resonator of length L using Euler-Bernoulli theory. The displacement of the mechanical resonator $U(z, t)$ from the equilibrium position in the absence of external force is described by the following equation. [80] [81]

$$\rho A \frac{\partial^2 U}{\partial t^2}(z, t) + EI \frac{\partial^4 U}{\partial z^4}(z, t) = 0 \quad (2.1)$$

where ρ is the density of a material, A is the cross-sectional area, E is Young's modulus, I is the moment of inertia along the longitudinal axis. By rewriting the displacement as $U(z, t) = U(z) \exp(-i\omega t)$, displacement should satisfy the following equation.

$$\frac{\partial^4 U}{\partial z^4}(z) = \left(\frac{\rho A}{EI}\right) \omega^2 U(z) \quad (2.2)$$

Then general solution which satisfies the equation has the form as follows

$$U(z, t) = a \cdot \cos(\beta z) + b \cdot \sin(\beta z) + c \cdot \cosh(\beta z) + d \cdot \sinh(\beta z) \quad (2.3)$$

where $\beta = (\rho A/EI)^{1/4} \omega^{1/2}$. For boundary condition for doubly-clamped mechanical resonator ($U(0) = U(L) = 0, dU(z=0)/dz = dU(z=L)/dz = 0$), it follows that $a = -c$ and $b = -d$ while β takes discrete values for the relation

$$\cos \beta_n L \cosh \beta_n L - 1 = 0 \quad (2.4)$$

By numerical calculation for eq. 2.4, $\beta_n L = 0, 4.730, 7.853, 10.996, 14.137, \dots$. Only using the nontrivial solution for $\beta_n L$, we can have the solution for displacement of n -th mode:

$$U_n = a_n[\cos(\beta_n z) - \cosh(\beta_n z)] + b_n[\sin(\beta_n z) - \sinh(\beta_n z)] \quad (2.5)$$

where the amplitude ratio a_n/b_n for the first few modes is found from the boundary conditions ($a_n/b_n = 1.018, 0.999, 1.000, \dots$). The values for $U_n(z)$ satisfy the normalization condition

$$\int_0^L U_n(z)U_m(z)dz = L^3\delta_{nm} \quad (2.6)$$

This condition yields $a_n = L$, while b_n can be found from the above relation. The resonant frequencies to corresponding modes are

$$\omega_n = \sqrt{\frac{EI}{\rho A}}\beta_n^2 \quad (2.7)$$

For the fundamental mode, $\beta_1 = 4.73/L$. Therefore, its resonance frequency is given by

$$f_1 = \frac{1}{2\pi} \frac{(4.73)^2}{L^2} \sqrt{\frac{EI}{\rho A}} \approx \frac{3.56}{L^2} \sqrt{\frac{EI}{\rho A}} \quad (2.8)$$

As cross sectional area $A = wt$, and moment of inertia $I = wt^3/12$, resonant frequency of fundamental mode is

$$f_1 = 1.03 \sqrt{\frac{E}{\rho}} \frac{t}{L^2} \quad (2.9)$$

The frequencies of higher modes are from the relation $f_n/f_1 = 2.756, 5.404, 8.933$ for $n = 2, 3, 4$.

From this relation, we can expect the relation of mechanical modes. In general case, mechanical resonator have resonant frequency of fundamental mode proportional to the thickness of mechanical resonator and inversely proportional to L^2 . In addition to the consideration of geometrical parameters, we can find that resonant frequency is proportional to the square-root of Young's modulus and inversely proportional to the square-root of density of material.

2.2 Doubly-clamped mechanical resonator with high-stress stoichiometric silicon nitride



Figure 2.3: Resonant mode of doubly-clamped mechanical resonator

Mechanical stress can significantly affect the properties of mechanical resonator in resonant frequency and Q -factor. Different from the general case of mechanical resonator without internal stress, we can derive the equation for elastic deformation of mechanical resonator with consideration of internal stress. [82] [83]

Based on the assumption that the beam material is linearly elastic, the shear deformation and rotary inertia are negligible, the differential equation for small deflection is

$$EI \frac{\partial^4 U(z)}{dz^4} - A\sigma_{int} \frac{\partial^2 U(z)}{\partial z^2} - \rho A \omega^2 U(z) = 0 \quad (2.10)$$

where $U(z)$ is the displacement from the equilibrium position of mechanical resonator at the position of z from one end, E is the Young's modulus, I is the moment of inertia, A is the cross-sectional area, ρ is the density of material and ω is the circular natural frequency. By introducing the dimensionless beam co-ordinate $\zeta = z/L$, where $0 \leq \zeta \leq 1$, the solution of eq. 2.10 may be written as

$$U(z) = c_1 \sinh(M\zeta) + c_2 \cosh(M\zeta) + c_3 \sin(N\zeta) + c_4 \cos(N\zeta) \quad (2.11)$$

in which c_1, c_2, c_3 and c_4 indicate the constant coefficients, and M and N are defined as

$$\begin{aligned} M &= l((\sigma_{int}A/2EI) + [(\sigma_{int}A/2EI)^2 + (\rho A/EI)\omega^2]^{1/2})^{1/2} \\ &= (Y + \sqrt{Y^2 + \Omega^2})^{1/2} \end{aligned} \quad (2.12)$$

$$\begin{aligned} N &= l(-(\sigma_{int}A/2EI) + [(\sigma_{int}A/2EI)^2 + (\rho A/EI)\omega^2]^{1/2})^{1/2} \\ &= (-Y + \sqrt{Y^2 + \Omega^2})^{1/2} \end{aligned} \quad (2.13)$$

where $Y = \sigma_{int}A/2EI$ is the dimensionless parameter for stress, $\Omega = \omega l^2/\alpha$ is the dimensionless natural frequency parameter and $\alpha = \sqrt{EI/\rho A}$.

Considering the doubly-clamped beam, boundary conditions are $U(0) = U(L) = 0$, $\partial U(z=0)/\partial z = \partial U(z=L)/\partial z = 0$. With these conditions on equation eq. 2.11 will result in the following relationship:

$$\Omega + Y \cdot \sinh(Y + \sqrt{Y^2 + \Omega^2})^{1/2} \cdot \sin(-Y + \sqrt{Y^2 + \Omega^2})^{1/2}$$

$$-\Omega \cdot \cosh(Y + \sqrt{Y^2 + \Omega^2})^{1/2} \cdot \cos(-Y + \sqrt{Y^2 + \Omega^2})^{1/2} = 0 \quad (2.14)$$

$$U_{mi} = \frac{(i+1)^2 \pi^2}{2} \quad (2.15)$$

$$\sigma_{cr} = \frac{4\pi^2 EI}{Al^2} \quad (2.16)$$

$$\Omega_i = \left[(4i-1) \frac{\pi}{4} \right]^2 \quad (2.17)$$

$$c_1 = 1 \quad (2.18)$$

$$c_2 = \frac{M(\cosh(M) - \cos(N))}{M \sin(M) + N \sin(N)} \quad (2.19)$$

$$c_3 = -\frac{M}{N} \quad (2.20)$$

$$c_4 = \frac{M(\cosh(M) - \cos(N))}{M \sin(M) + N \sin(N)} \quad (2.21)$$

Where σ_{cr} is the critical stress, Ω_i is the i -th mode natural frequency parameter, c_1, c_2, c_3, c_4 is the mode shape coefficients, U_I is the critical buckling load.

From this result and resonant frequency of mechanical resonator without stress, we can conclude that resonant frequency of fundamental mode under tensile stress is given as follows.

$$f(\sigma_{int}) = f_0 \sqrt{1 + \frac{\rho_{int} L^2}{3.4 E w^2}} \quad (2.22)$$

where f_0 is the fundamental resonant frequency of mechanical resonator without tensile stress.

In case of high-stress doubly-clamped mechanical resonator, we can observe some different characteristics compared to mechanical resonators realized from stress-less or stress-free materials. First, with doubly-clamped mechanical resonator from high-stress Si_3N_4 , resonant frequency of n-th higher modes become n-time the resonant frequency of fundamental mode with similar vibration mode (in-plane, out-of-plane, torsional...), which can be observed in the case of string. For case of 2nd mode of flexural or out-of-plane vibrational mode, measured frequency of fundamental mode is ~ 3.5 MHz and resonant frequency of 2nd mode is ~ 7.01 MHz which is approximately twice the resonant frequency of fundamental mode. In case of the doubly-clamped mechanical resonator made from Si, which has much less intrinsic stress, 2nd mode resonant frequency is inversely proportional to the square of frequency of fundamental mode.

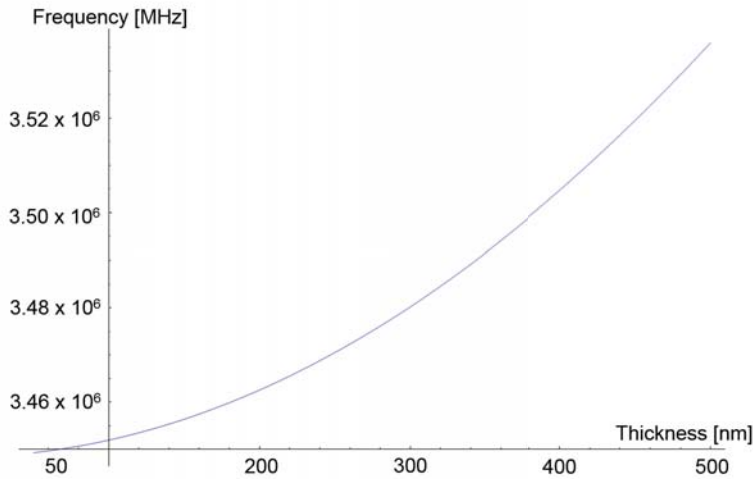


Figure 2.4: Fundamental resonant frequency vs thickness

Second, for mechanical resonators with high-stress material, resonant frequency is less dependent on the geometry or thickness of resonant structure.

For high-stress material, resonant frequency, resonant frequency of 50 nm thickness is expected to be 3.45 MHz. But for the same structure with thickness of 500 nm, resonant frequency is 3.54 MHz from the theoretical calculation, which is only ~ 2.6 percent increase. For mechanical resonators with Si, resonant frequency of mechanical resonator is inversely proportional to the square-root of thickness of moving structure. Thus, mechanical resonator from high-stress material can have high-frequency operation functionality with reduced thickness or smaller dimensions.

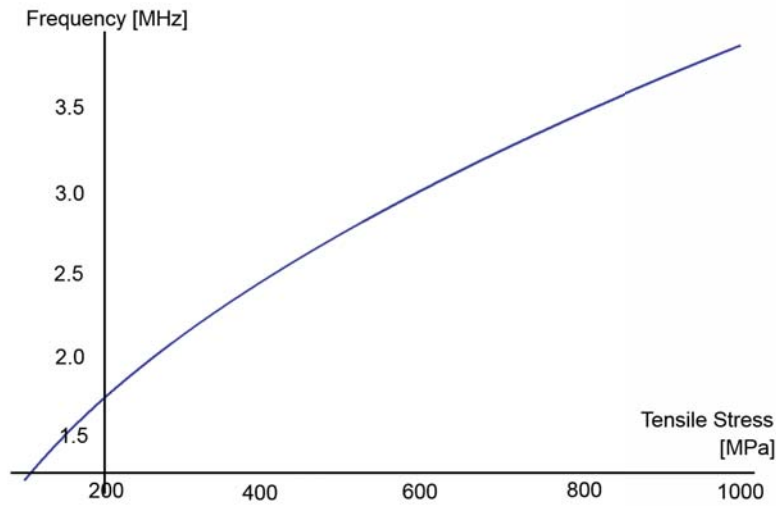


Figure 2.5: Fundamental resonant frequency vs stress

Third, with tuning the stress of material, we can tune the resonant frequency of mechanical resonator in wide range. By tuning the resonant frequency from 200 MPa to 800 MPa, resonant frequency, resonant frequency of mechanical resonator of 80 micron length is tuned from ~ 1.75 MHz to ~ 3.8 MHz(fig. 2.5). When compared the resonant frequency of mechanical with same dimensions from Si, same structure from high-stress(~ 800 MPa) Si_3N_4 has approximately 5 times higher resonant frequency.

Four, mechanical resonator from high-stress material can have high- Q . Due to the high-stress in mechanical structure, elastic energy can be stored in the resonant structure with less dissipation to substrate or clamping structure. Using this advantages, doubly-clamped mechanical resonator from high-stress Si_3N_4 have shown high- Q above 200,000 [17] and square-type membrane shows more than $Q \sim 10 \times 10^6$. [84] This high- Q makes membrane from high-stress as a most potential candidate for observation of quantum-mechanical properties in real-mechanical systems.

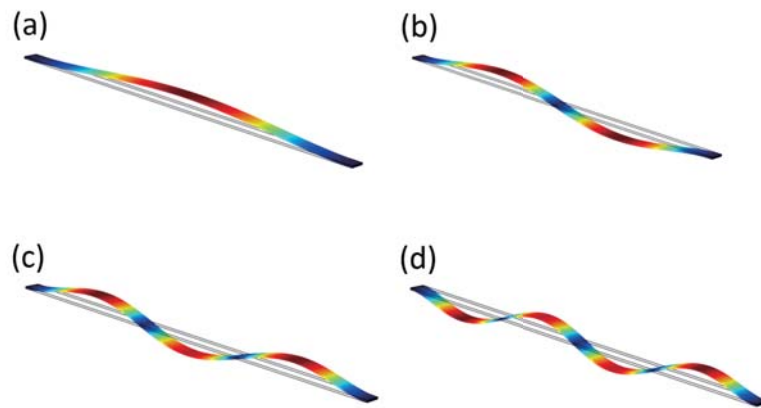


Figure 2.6: Four out-of-plane flexural modes of doubly-clamped mechanical resonator constructed by Finite Element Analysis (COMSOL version 4.3b). As mode number increases, number anti-nodal points increase

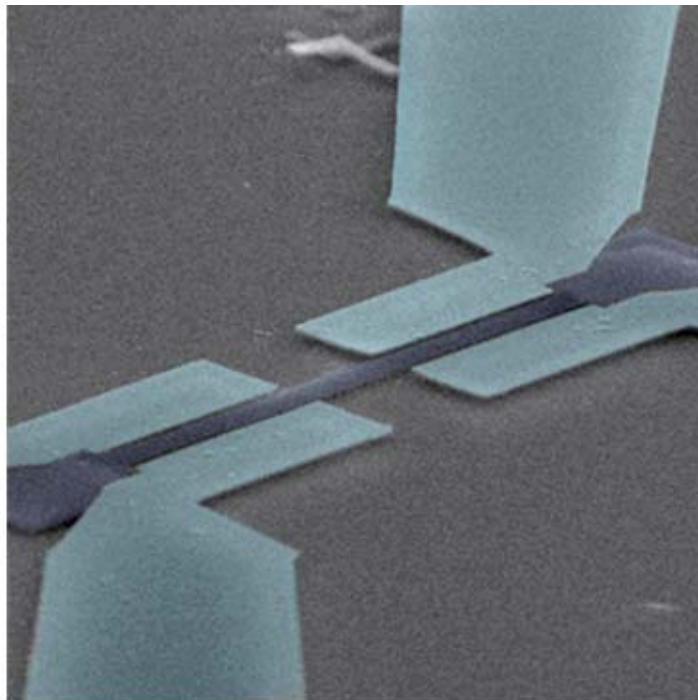


Figure 2.7: Scanning electron micrograph of doubly-clamped mechanical resonator. Electrodes are patterned next to the mechanical resonator to apply V_{dc} for polarization of dielectric mechanical resonator and V_{rf} for actuation

2.3 Membrane mechanical resonator with high-stress stoichiometric silicon nitride

To estimate the vibrational mode and the frequency of motional state, first, we should start from the theoretical calculation of vibration of membrane. It is assumed in the membrane dynamics that membrane is perfectly flexible from uniform material. And membranes are stretched uniformly during the stretching and fluctuations in tension by stretched motion is infinitesimal. By this assumption, we define the global parameters, s as the displacement of any point of the membrane at right angles to $x - y$ plane, S is the uniform tension per unit length of the boundary, and w is the weight of the membrane per unit area.

The area of the surface of the membrane in a deflected position will be [85]

$$A = \iint \sqrt{1 + \left(\frac{\partial v}{\partial x}\right)^2 + \left(\frac{\partial v}{\partial y}\right)^2} dx dy \quad (2.23)$$

When the deflections during vibration are very small, then equation 2.23 become

$$A = \iint \left(1 + \frac{1}{2}\left(\frac{\partial v}{\partial x}\right)^2 + \frac{1}{2}\left(\frac{\partial v}{\partial y}\right)^2\right) dx dy \quad (2.24)$$

Then, the increase in potential energy will be given

$$V = \frac{S}{2} \iint \left(1 + \left(\frac{\partial v}{\partial x}\right)^2 + \left(\frac{\partial v}{\partial y}\right)^2\right) dx dy \quad (2.25)$$

and kinetic energy of membrane is

$$T = \iint \frac{w}{2g} \dot{v}^2 dx dy \quad (2.26)$$

If we set a and b as the length of the sides of the membrane, or length of axis x and y , it always can be represented within the limits of the rectangle by the double series.

$$v = \sum_{m=1}^{m=\infty} \sum_{n=1}^{n=\infty} q_{m,n} \sin \frac{m\pi x}{a} \sin \frac{n\pi y}{b} \quad (2.27)$$

the coefficients $q_{m,n}$ is taken as the generalized coordinates for this case. As a boundary conditions, $v = 0$ for $x = 0, x = a$ and $v = 0$ for $y = 0, y = b$.

Using equation 2.25 and 2.27, we can obtain following equation.

$$V = \frac{S\pi^2}{2} \int_0^a \int_0^b \left(\sum \sum q_{m,n} \frac{m}{a} \cos \frac{m\pi x}{a} \sin \frac{n\pi y}{b} \right)^2 + \left(\sum \sum q_{m,n} \frac{n}{b} \sin \frac{m\pi x}{a} \cos \frac{n\pi y}{b} \right)^2 dx dy \quad (2.28)$$

Integrating this expression over the area the area of the membrane, we find the formula for potential energy of membrane as

$$V = \frac{S}{2} \frac{ab\pi^2}{4} \sum_{m=1}^{m=\infty} \sum_{n=1}^{n=\infty} n = \infty \left(\frac{m^2}{a^2} + \frac{n^2}{b^2} \right) q_{m,n}^2 \quad (2.29)$$

and kinetic energy of membrane

$$T = \frac{w}{2g} \frac{ab}{4} \sum \sum \dot{q}_{m,n}^2 \quad (2.30)$$

Using the potential and kinetic energy expression and generalized coordinate $q_{m,n}$, the differential equation of a normal vibration will be

$$\frac{w}{g} \frac{ab}{4} \ddot{q}_{m,n} + S \frac{ab\pi^2}{4} \left(\frac{m^2}{a^2} + \frac{n^2}{b^2} \right) q_{m,n} = 0 \quad (2.31)$$

From which,

$$f_{m,n} = \frac{1}{2} \sqrt{\frac{gS}{w} \left(\frac{m^2}{a^2} + \frac{n^2}{b^2} \right)} \quad (2.32)$$

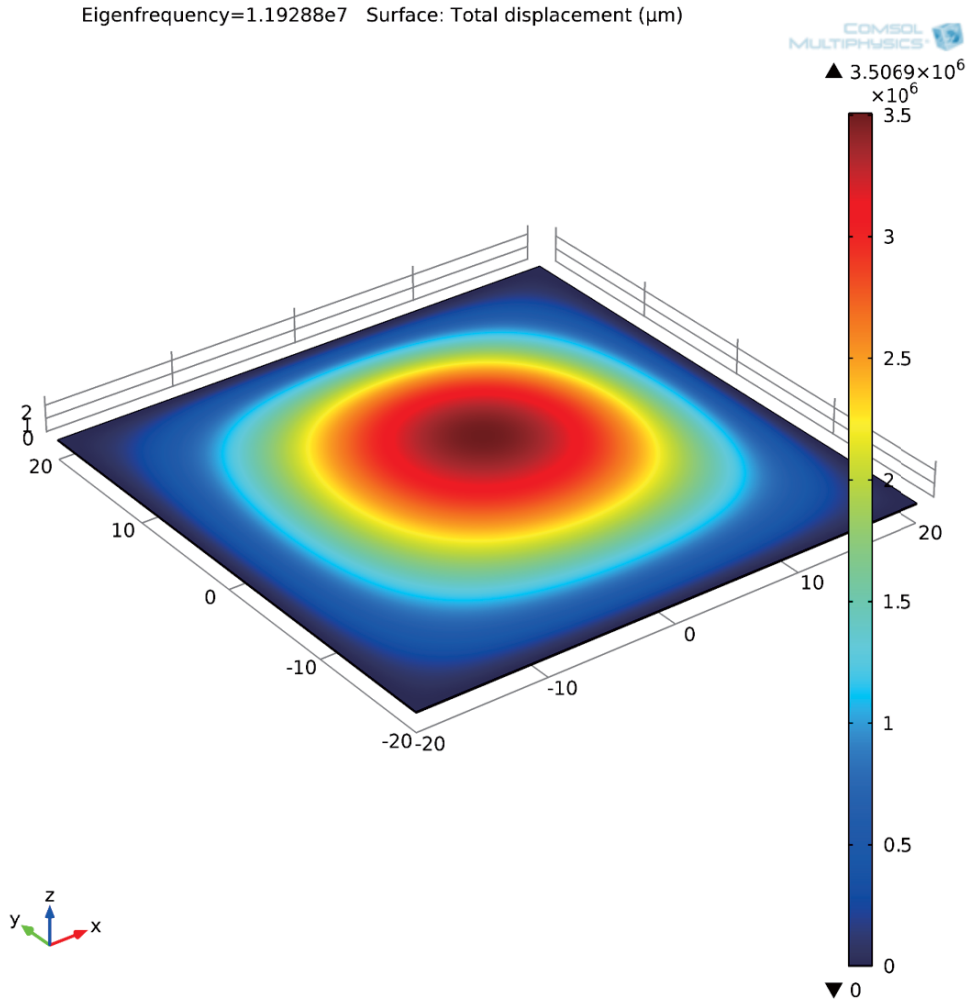


Figure 2.8: Fundamental vibration mode of membrane calculated by Finite Element Analysis (COMSOL 4.3b. Maximum amplitude of deflection of membrane can be observed at the center of membrane.)

The lowest mode of vibration will be obtained by putting $m = n = 1$.

Then

$$f_{1,1} = \frac{1}{2} \sqrt{\frac{gS}{w} \left(\frac{1}{a^2} + \frac{1}{b^2} \right)} \quad (2.33)$$

The deflection surface of the membrane in this case is

$$v = C \sin \frac{\pi x}{a} \sin \frac{\pi y}{b} \quad (2.34)$$

In the same manner, the higher modes of vibration can be obtained. For square membrane, when $a = b$, the frequency of the lowest mode is

$$f_{1,1} = \frac{1}{\sqrt{2}} \sqrt{\frac{gS}{w}} \quad (2.35)$$

The frequency is directly proportional to the square root of the tension S and the inversely proportional to the length of sides of the membrane and to square root of the load per unit area.

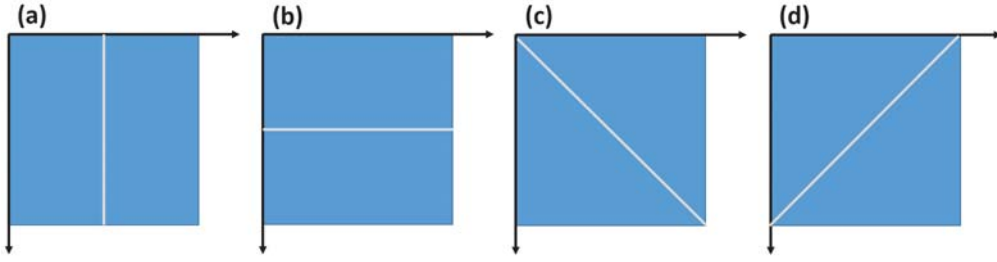


Figure 2.9: Superimposed vibrational mode of membrane with index number m and n , one of which is 2 and the other is equal to 1. (a) $D = 0$, (b) $C = 0$, (c) $C = D$, (d) $C = -D$. As different two modes have the same resonant frequency, we can express the mode shape of 2nd membrane mode as the superposition of two different mode with same frequency.

The next two higher modes of vibration will be obtained by taking one of the numbers m, n equal to 2 and the other to 1. These two modes have the same frequency, but different shapes of mode. Due to the same resonant mode frequency, it is possible to superimpose these two surfaces on each other in any ratio of their maximum deflections.

$$v = \left(C \sin \frac{2\pi x}{a} \sin \frac{\pi y}{a} + D \sin \frac{\pi x}{a} \sin \frac{2\pi y}{a} \right) \quad (2.36)$$

where C and D are arbitrary quantities.

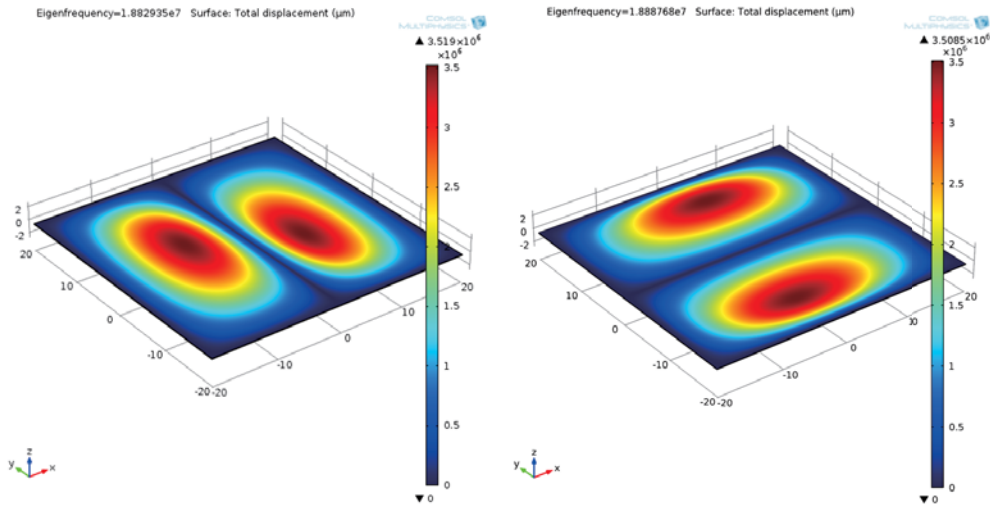


Figure 2.10: 2nd vibrational mode of membrane calculated by Finite Element Analysis (COMSOL 4.3b). At the 2nd mode, two different modes can have same resonant frequency ($(m, n) = (2, 1)$ and $(1, 2)$). The other mode shape of 2nd membrane mode can be presented as the mode shape by 90 degree rotation to clockwise or counter-clockwise direction to one mode shape.

Four particular cases of such a combined vibration are as shown in fig. 2.9. The membrane, while in vibration, is divided into two equal parts by a vertical nodal line (white line in each vibration mode (a), (b), (c), and (d) of fig. 2.9

For example, when $C = 0$, the membrane is sub-divided by a horizontal nodal line as in fig. 2.9. When $C = D$, we can obtain

$$\begin{aligned}
 v &= C \sin \frac{2\pi x}{a} \sin \frac{\pi y}{a} + C \sin \frac{\pi x}{a} \sin \frac{2\pi y}{a} \\
 &= 2C \sin \frac{\pi x}{a} \sin \frac{\pi y}{a} \left(\cos \frac{\pi x}{a} + \cos \frac{\pi y}{a} \right)
 \end{aligned} \tag{2.37}$$

In the case of forced vibration of the membrane the differential equation of motion (f) becomes

$$\frac{w}{g} \frac{ab}{4} \ddot{q}_{m,n} + S \frac{ab\pi^2}{4} \left(\frac{m^2}{a^2} + \frac{n^2}{b^2} \right) q_{m,n} = Q_{m,n} \quad (2.38)$$

in which $Q_{m,n}$ is the generalized disturbing force corresponding to the coordinate $q_{m,n}$.

To realize the membrane structure which can be accessed from both normal direction of surface, we fabricated the membrane structure which is widely used for TEM grid(Norcada Co.). First, double-layer of Si_3N_4 (~100 nm)/ SiO_2 (~100 nm) is deposited on the Si wafer. By removing Si_3N_4 and SiO_2 layer on the backside of Si wafer, square shape is patterned and Si is etched until SiO_2 is met. After etching process of sacrificial layer (SiO_2), only Si_3N_4 membrane is suspended. To pattern the electrode, electrode pattern is transferred on the surface next the the suspended structure by conventional E-beam lithography technique.

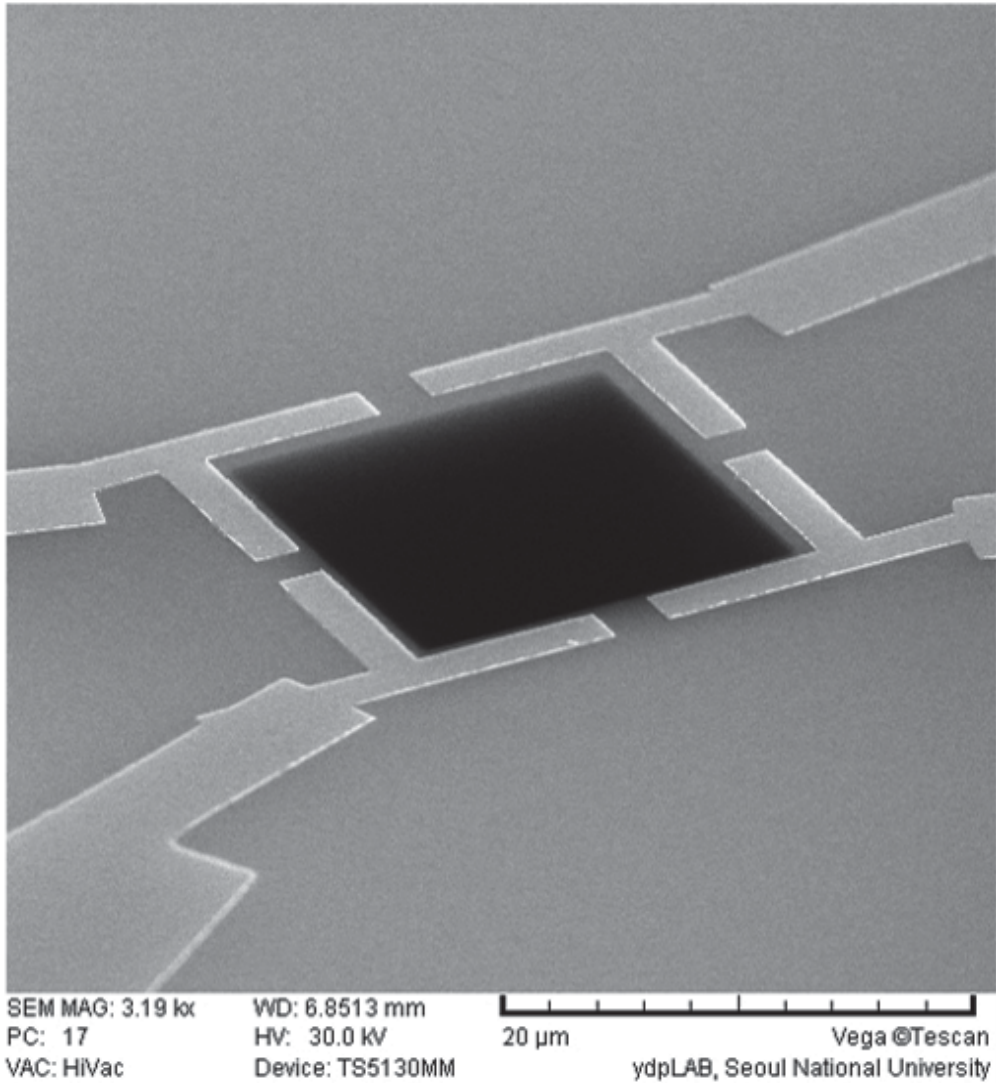


Figure 2.11: Scanning electron micrograph of membrane mechanical resonator of 20 micron width. As silicon nitride(Si_3N_4) membrane is dielectric which do not make secondary electron, membrane is shown as black color. Electrodes which are deposited in the vicinity of membrane structure can apply DC and rf signal to membrane structure.

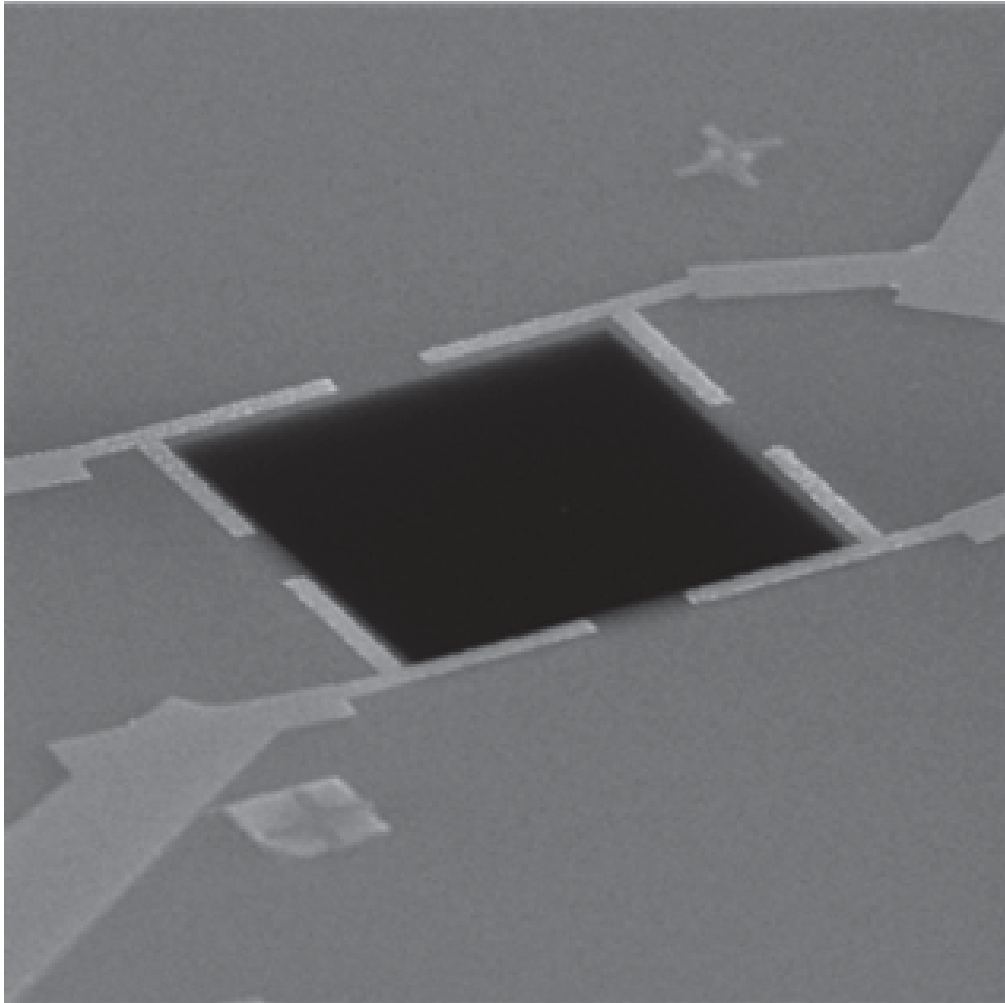


Figure 2.12: Scanning electron micrograph of membrane mechanical resonator of 40 micron width. As silicon nitride(Si_3N_4) membrane is dielectric which do not make secondary electron, membrane is shown as black color. Electrodes which are deposited in the vicinity of membrane structure can apply DC and rf signal to membrane structure.

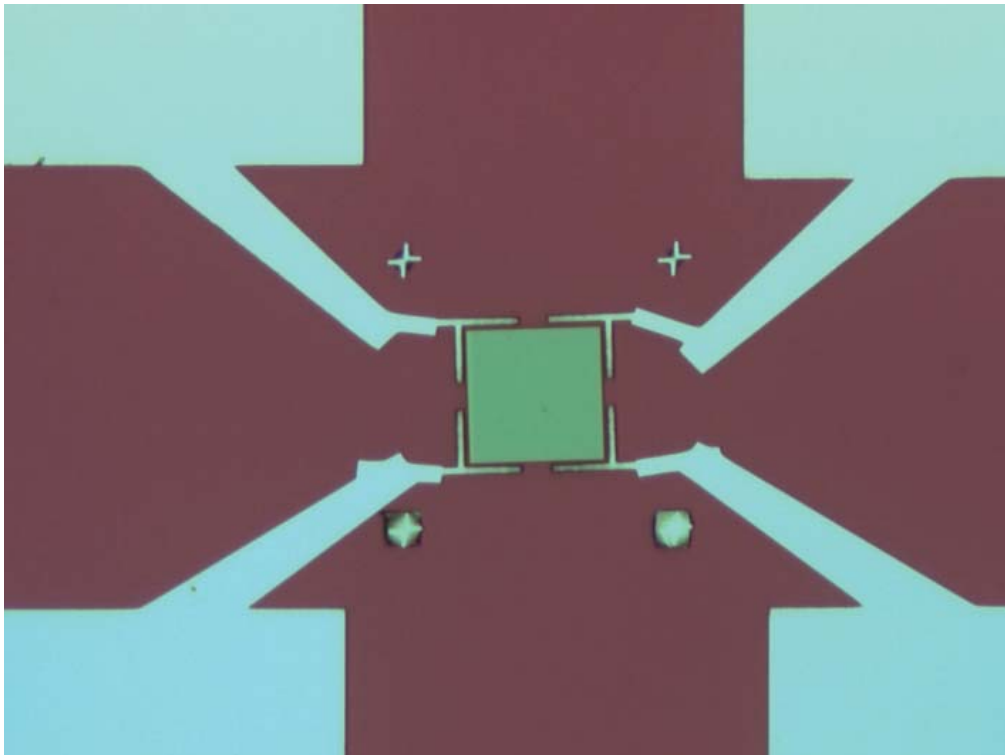


Figure 2.13: Optical image of membrane mechanical resonator of 40 micron width. Silicon nitride(Si_3N_4) membrane(green) is fabricated by etching the Si wafer and SiO_2 layer on the backside. After suspend the square membrane by etching process, electrodes which are surrounding the membrane structure is patterned to apply electrical field for electrical field gradient actuation.

Chapter 3

Optical measurement and electrical field gradient actuation technique

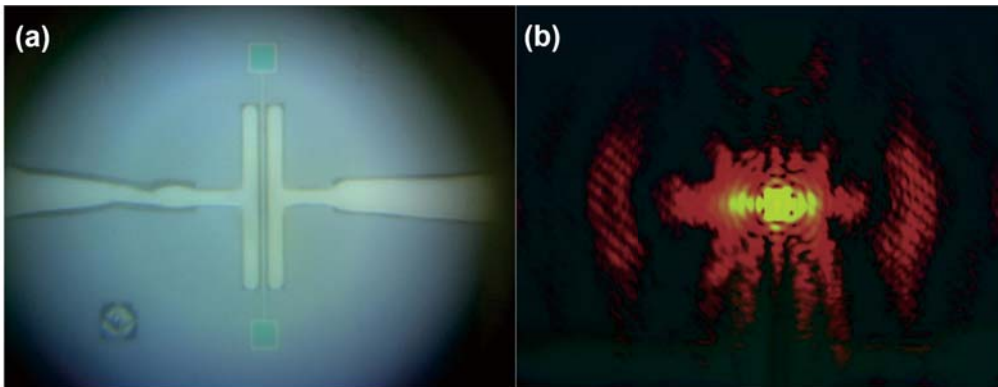


Figure 3.1: Optical image of doubly-clamped micromechanical resonator without probing laser (a) and with probing laser (b). Optical image is captured using CCD camera attached to optical set-up and sample is mounted in the vacuum chamber.

To actuate and measure the motion of mechanical resonator, we need to adopt actuation and measurement technique which do not degrade the Q during the experimental steps. Electrical field gradient actuation technique

is known to have advantages in realization of resonant motion with high- Q and high-frequency operation. [28] Using a set of separated electrodes, we polarize and actuate a dielectric resonator under a electrical field gradient with simple voltage tuning of the mechanical resonance and applied rf-signal of small amplitude. Optical measurement technique do not need additional components to the movable structures. Thus, except the dissipation by thermal heating by incident probing optical beam or laser, Q is not affected or degraded by measurement process.

In this chapter, I'll review the optical measurement technique which has been used to measure the motion of mechanical resonator, set-up for optical measurement, and induced noises. Then, electrical field gradient actuations for high-mechanical resonator will be reviewed. Doubly-clamped mechanical resonator with on-chip [86] and off-chip electrode with sample fabrication process will be presented followed by membrane resonator with on-chip electrode.

3.1 Optical measurement of mechanical resonator

Optical measurement technique was used from the first realization of nanomechanical resonator and have shown its potential in versatility to many different types of resonators. Recently, optical measurement technique such as path-stabilized *Michelson* interferometry, [22] *Fabry – Perot* interferometry, [87] and *optical – fiber* technique [88] have been extended to measurement of micro- and nano-mechanical systems. A probing laser-beam is focused on the surface of mechanical resonator which is in motion and is reflected back to the PD. For *Michelson-interferometry* geometry, reflected

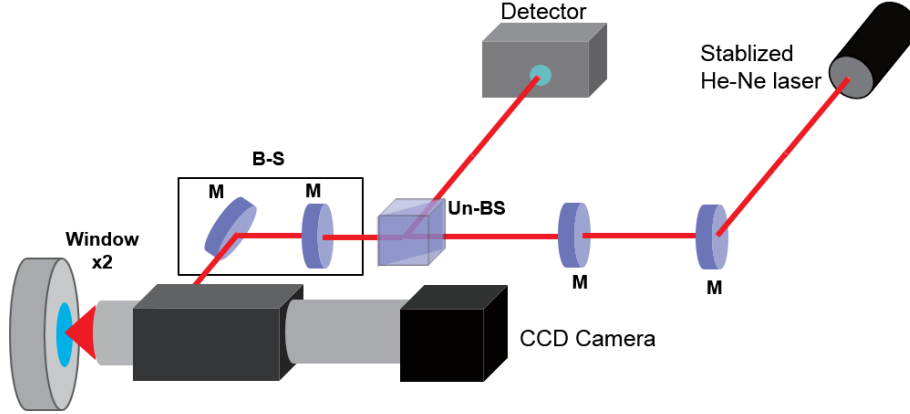


Figure 3.2: Schematic diagram of optical measurement. He-Ne laser as a probing beam is directed to the surface of mechanical resonator while half of optical power is splitted by beam-splitter. Using objective lens with relatively long working-distance, collimated laser beam is focused on the surface of mechanical resonator in the vacuum chamber. Reflected beam is re-collected by objective laser and directed to PD. Modulated laser beam is measured by PD. CCD is used to observe the laser spot on the sample.

beam and reference beam which is splitted by beam-splitter in front of the objective lens interfere each other and amplitude modulation is measured by PD. In case of Fabry-Perot interferometry, optical cavity formed by mechanical resonator and substrate modulates the optical signal as the mechanical resonator is driven or in thermal motion. Optical reflectance measurement is done in which optical property of substrate and oscillating component do not matches the suitable optical cavity or reference beam cannot be stabilized by experimental limitation.

To apply reflectance measurement to mechanical resonator, laser beam is assumed to have gaussian waveform. Then, gaussian intensity distribution of probing He-Ne laser is [89]

$$I(r) = I_0 \exp\left(-\frac{2r^2}{\omega_0^2}\right) \quad (3.1)$$

where ω_0 is gaussian beam radius, which is the radius at which the intensity has decreased to $1/e^2$, or 0.135 of its axial, or peak value. r is the radius of gaussian beam, I_0 is the intensity of laser beam.

The power contained within a radius r , $P(r)$ is obtained by integrating the intensity distribution from 0 to r .

$$P(r) = P(\infty) \left[1 - \left(-\frac{2r^2}{\omega_0^2} \right) \right] \quad (3.2)$$

When normalized to the total power of the beam, $P(\infty)$ in watts, the curve is the same as that for intensity. Nearly 100% of the power is contained in a radius $r = 2\omega_0$. One-half the power is contained within $0.59\omega_0$, and only about 10% is contained with $0.23\omega_0$.

For laser beam diverging from the focal point, gaussian beam radius ω at a distance x from the focal point is described as

$$\omega^2(x) = \omega_0^2 \left[1 + \left(\frac{\lambda x}{\pi \omega_0^2} \right)^2 \right] \quad (3.3)$$

where ω_0 is the radius of laser spot on focal point, which is defined as

$$2\omega_0 = \left[\frac{4\lambda}{\pi} \right] \left[\frac{F}{D} \right] \quad (3.4)$$

with D is the diameter of the laser beam which is measured at the objective lens which is facing the sample, F is the focal length or working distance of objective lens.

Then, difference of optical power of probing laser beam reflected on the mechanical resonator is the difference of power at focal point and x , which is the displacement of mechanical resonator from the equilibrium position. Thus the difference of power is as follows.

$$\begin{aligned}
dP = P_0 - P(x) &= P(r) \left[1 - \exp\left(-\frac{2r^2}{\omega_0^2}\right) \right] - P(r) \left[1 - \exp\left(-\frac{2r^2}{\omega^2(x)}\right) \right] \\
&= P(r) \left[-\exp\left(-\frac{2r^2}{\omega_0^2}\right) + \exp\left(-\frac{2r^2}{\omega^2(x)}\right) \right] \quad (3.5)
\end{aligned}$$

With $\omega^2(x)$, which is defined in eq. 3.3, we can find the full equation for the power difference by the displacement of mechanical resonator, x

$$\begin{aligned}
dP &= P(r) \left[-\exp\left(-\frac{2r^2}{\omega_0^2}\right) + \exp\left(-\frac{2r^2}{\omega_0^2(1 + (\lambda x/\pi\omega_0^2)^2)}\right) \right] \\
&= P(r) \left[-\exp\left(-\frac{2r^2}{\omega_0^2}\right) + \exp\left(-\frac{2r^2\pi^2\omega_0^2}{\pi^2\omega_0^4 + \lambda^2x^2}\right) \right] \quad (3.6)
\end{aligned}$$

Where $P(r)$ is the power of incident laser on the mechanical resonator. In this approach, we assume that $x^2 + y^2 = r^2$ for circular coordinate. Thus in real calculation, r^2 should be transformed for the coordinate and area of mechanical resonator where probing laser is incident.

For selection of wavelength of probing laser or PD(Si, InGaAs, et al.), we should consider the optical property of material for mechanical resonator. Si_3N_4 has reflectivity of approximately 12% for wavelength of 633 nm and reflectivity decrease as the wavelength become shorter. [90] For photodiode on the PD made from Si, sensitivity is maximized at the wavelength of ~ 800 nm. [91] Thus, for visible light or wavelength, longer wavelength is better for sensitive measurement, as reflectivity does not change significantly compared to the change of sensitivity of photodiode. With the free-space optical set-up to guide the probing laser beam, vacuum chamber was designed to reduce the reflected laser light on the surface of optical window and scattering of light inside the chamber. Optical window designed for use of 633 nm He-

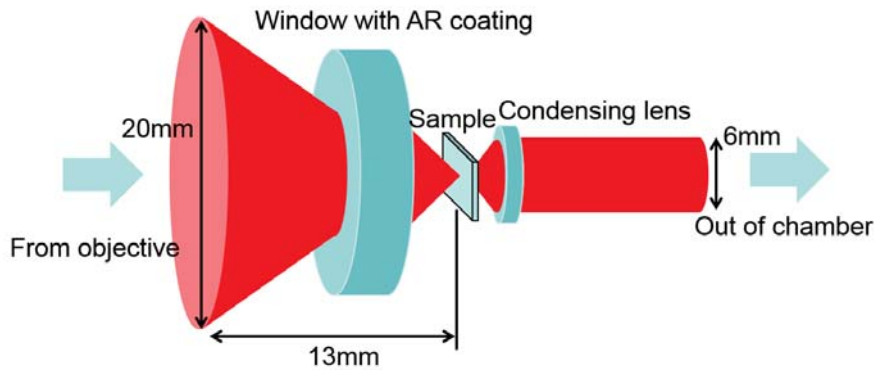


Figure 3.3: Schematic diagram of laser focus on sample. In vacuum chamber for optical measurement, laser beam of 20 mm width is focused by the objective lens. AR-coated optical window with 2 mm thickness is used to access laser beam onto the sample and maintain the vacuum of chamber. After focused on the surface of mechanical resonator, laser beam diverges and re-focused by condensing laser to collimate diverging beam into parallel beam. Collimated laser beam is guided to outside of optical chamber through 2nd optical window to prevent internal reflection inside the chamber, which can be a noise source for optical measurement.

The laser was mounted on top of the vacuum chamber and o-ring was also placed to sustain the vacuum inside the chamber between optical window and chamber.

Laser light is incident on the sample through the larger optical window. Refractive constant of optical window refract the laser beam, but as of the thickness of optical window ($\sim 2\text{mm}$), change of optical property and spot size of incident laser beam is relatively small. Laser beam reflected on the surface of mechanical resonator or substrate is collected by the objective lens and transferred to the PD. Other laser light which penetrate the mechanical resonator and substrate is guided to the high-NA condensing lens for collimation of laser beam. As photons which are not reflected on the surface or not absorbed by the mechanical resonator and substrate is collected and guided to outside of vacuum chamber through the optical window at the bottom

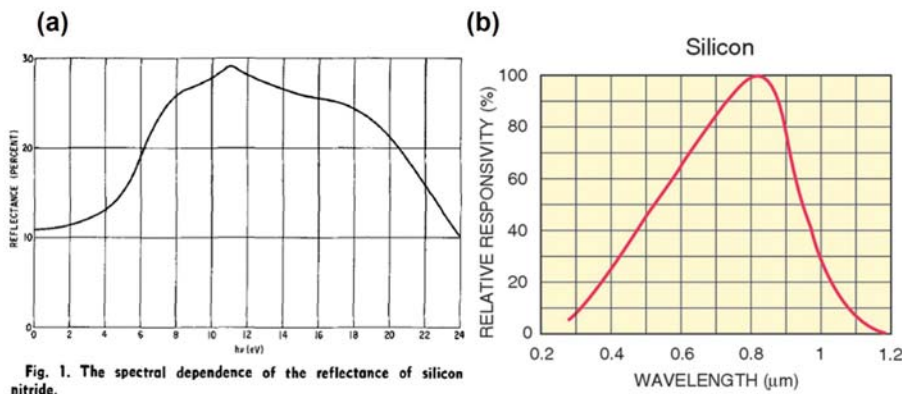


Figure 3.4: Reflectance of silicon nitride (a) and sensitivity of photo-detector (b) to wavelength of light. As the wavelength become longer, reflectivity of Si_3N_4 become smaller but does not change significantly. For Si which is used for photodiode in PD, sensitivity is maximized at the wavelength of ~ 800 nm and decreases proportional to the wavelength of laser. As the sensitivity changes more rapidly to the wavelength of laser, in the visible range, laser with 633 nm or longer wavelength is more suitable for sensitive measurement.(figure from webpage of Newport Corporation)

of the vacuum chamber, scattering effect inside the vacuum chamber can be neglected.

To accommodate rf-signal and V_{DC} to actuate and polarize the Si_3N_4 mechanical resonator, SMA-type rf connector is attached to the bottom of vacuum chamber. Ground-line of vacuum chamber is connected to the body of vacuum chamber. From the connector to the electrode, semi-rigid rf-cable is transmitting applied rf-signal.



Figure 3.5: Design of chamber components. For vacuum and optical window (one for laser-in, the other for laser-out), vacuum chamber was designed to have two window cover, three o-ring, one sample stand, one anodized-sample mount, and one bottom-cover with rf-connector. Each components are assembled into one chamber for optical measurement.

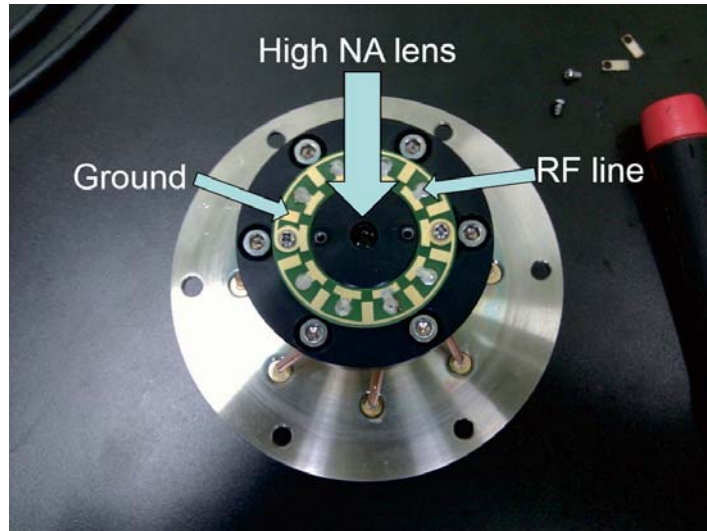


Figure 3.6: Optical image of sample mount. Sample is placed on the sample mount which is anodized to prevent the scattering of incident laser. PCB circuit is designed to accommodate eight-rf signal line for actuation. One high NA condensing lens under the sample mount is used to collect the laser beam which have penetrated the mechanical resonator and substrate and prevent reflection from the surface of chamber component

To reduce the vibrational noise or acoustic noise from the environment, all free-space optical set-up is mounted on the optical table and optical table is floated by the compressed air or nitrogen gas for vibration isolation from the floor (Fig. 3.7). From the measurement of acoustic noise which can possibly affect the optical measurement, we could not find any significant and permanent noise signal in the \sim MHz region, where we investigated the resonant motion of mechanical resonator. In case of stability of optical measurement, we could easily get stability for single-shot measurement of resonant motion and frequency- and power-sweep measurement which takes up to 1 hour. But because of the temperature change during the measurement which can affect the measurement stability, measurement for long-time is allowed only when temperature does not change more than 0.1 K.

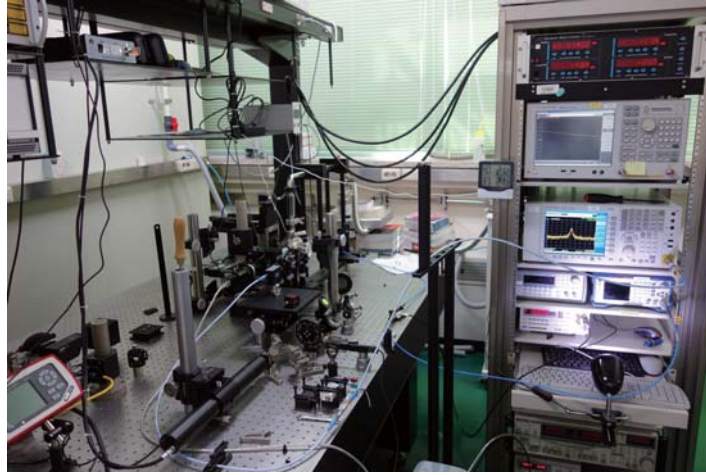


Figure 3.7: Optical image of electrical and optical measurement set-up. Free-space optical set-up is mounted on the optical table which is isolated from the acoustic noise by external vibration of environment.

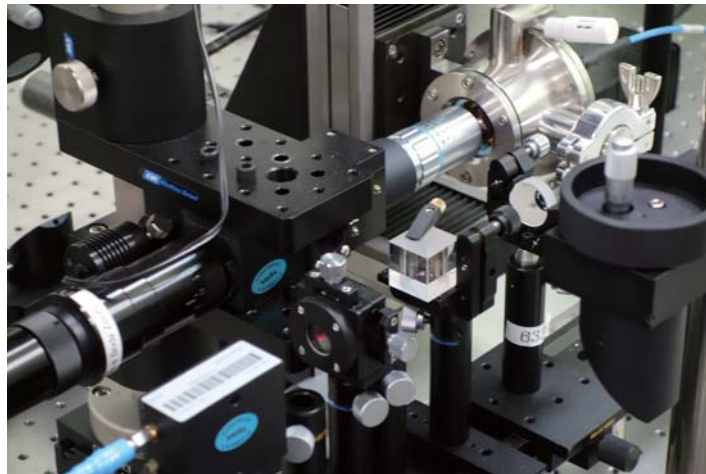


Figure 3.8: Detailed optical image of sample chamber and laser beam path. Collimated laser beam from stabilized He-Ne laser is guided to the objective lens. Reflected laser beam is re-collected by the objective lens and transferred to the optical detector through the plano-convex lens to increase the sensitivity. Because of the stability, laser beam splitted by the beam splitter is not used as a reference beam for inteferometric measurement.

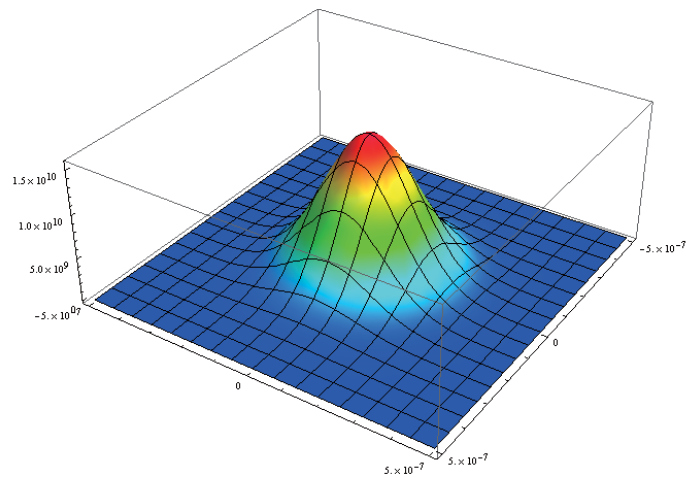


Figure 3.9: Numerical simulation of laser intensity at focal point. Beam waist is assumed to be 250 nm. We used the Mathematica 9.0 for numerical calculation of intensity profile.

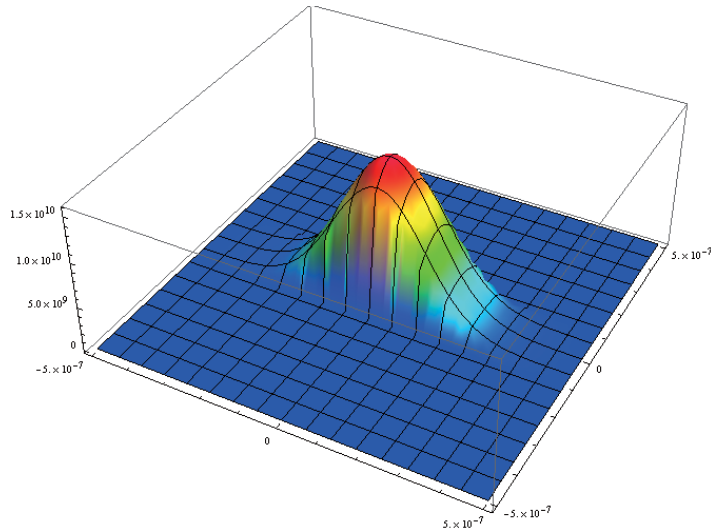


Figure 3.10: Numerical simulation of laser beam intensity on mechanical resonator after reflection on the surface of mechanical resonator of 200 nm width. Because of the small width of mechanical resonator, much of the laser beam is lost on the mechanical resonator and cause the small optical signal recorded by PD

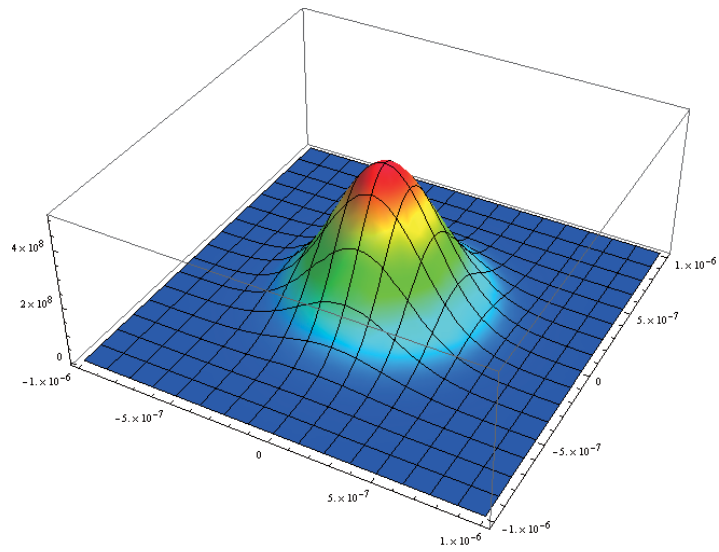


Figure 3.11: Numerical simulation of laser intensity at focal point. Beam waist is assumed to be 500 nm

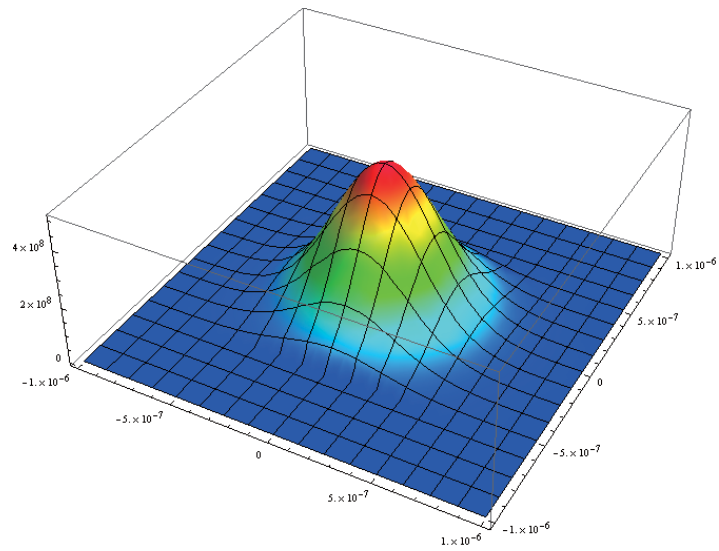


Figure 3.12: Numerical simulation of laser beam intensity on mechanical resonator after reflection on resonator of 1 micron width. Due to large width compared to the beam waist, we can observe only small loss in optical intensity after reflection

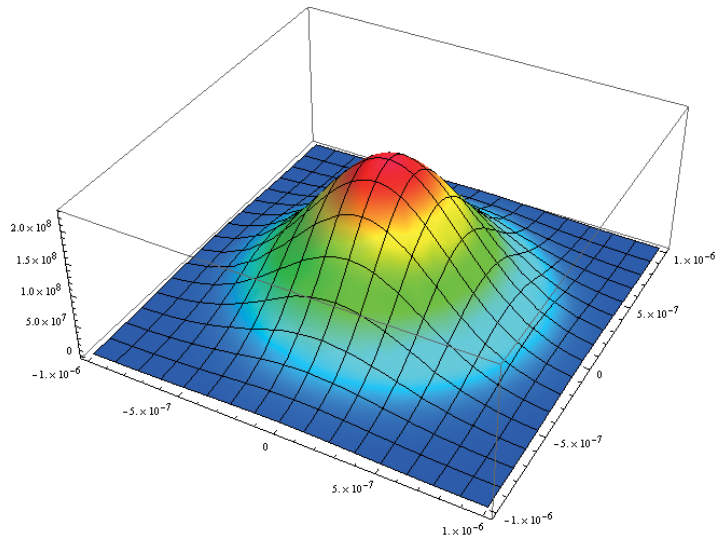


Figure 3.13: Numerical simulation of laser intensity at focal point. Beam waist is assumed to be 750 nm

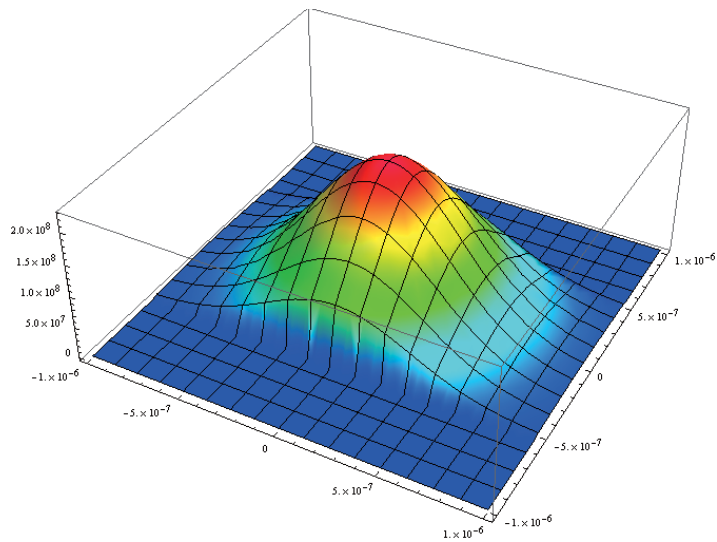


Figure 3.14: Numerical simulation of laser beam intensity on mechanical resonator after reflection on resonator of 1 micron width. Due to larger beam waist compared to the width of mechanical resonator, relatively large loss of optical intensity can be observed.

3.2 Noise in optical measurement

Before measurement process, we should take steps to exclude external noise such as laser frequency noise, laser intensity noise, vibrational noise, amplifier-added noise, electrical noise from function generator or rf-signal generator and so on. To identify the exact resonant signal from mechanical resonator which is transferred reflected laser beam, we took several steps to discriminate the measured noise signal.

First, we measured the noise with laser, but PD is off (electrical line from PD is connected to SA, but PD is turned-off). We could not find any significant signal or spurious peaks from the SA measurement (Fig. 3.15). In this measurement, we can observe the intrinsic spectral noise in the PD.

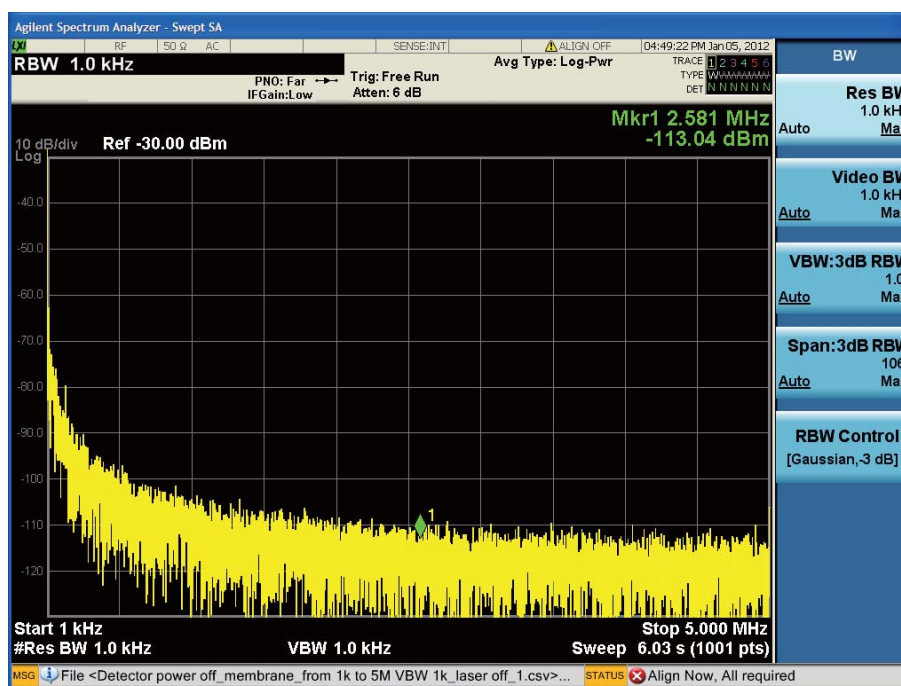


Figure 3.15: Electrical noise with laser and without detector. As laser beam is not guided to PD, only scattered photons from external light sources can be measured. And we cannot observe frequency or intensity noise from laser.

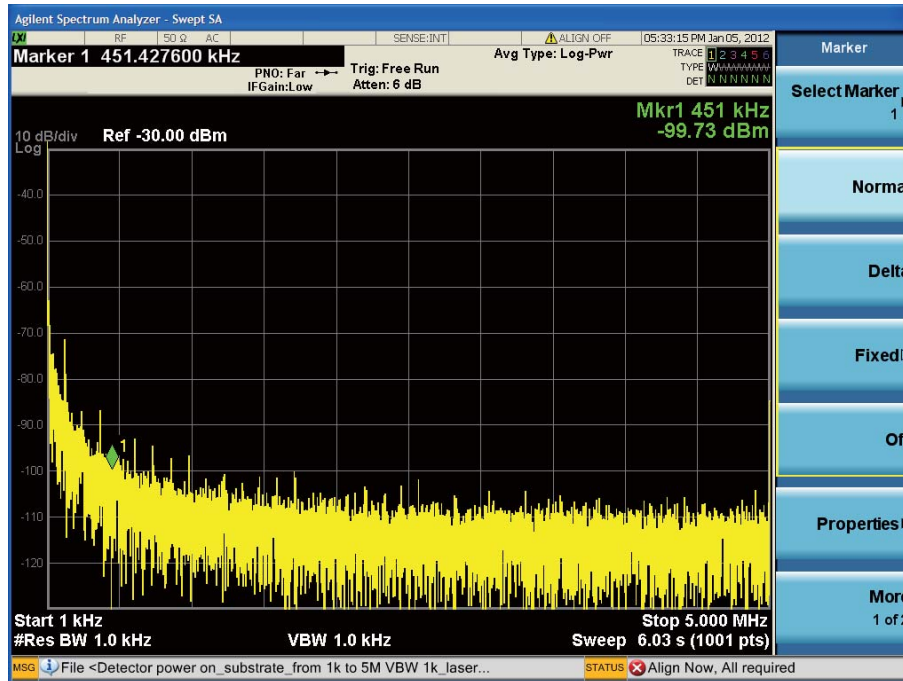


Figure 3.16: Electrical noise with detector and without laser beam. As we turn-on the PD, some spurious noise peaks can be observed in the noise spectral density measurement. As the amplitude of spectral noise is relatively small, we can attribute these spectral noise to scattered photon from stabilized He-Ne laser. To identify the source of these peaks we compared this measurement with other measurement done with laser

As a next step, to find the electrical noise from PD, we turned on the PD, but we blocked the incident laser to the PD(Fig. 3.16). With PD connected to SA, we could find some spurious peaks in the low frequency regime below the ~ 3 MHz. From this measurement, we could find the spectral noise due to frequency or intensity noise of He-Ne laser. Spectral noises with regular interval are considered to be from rf signal sources.

Then, we measured the spectrum from the PD with probing laser reflected on the surface of Si_3N_4 membrane resonator to discriminate the external noise. In this measurement we could find multiple peaks which is attributed to the laser frequency noise(Fig. 3.17).

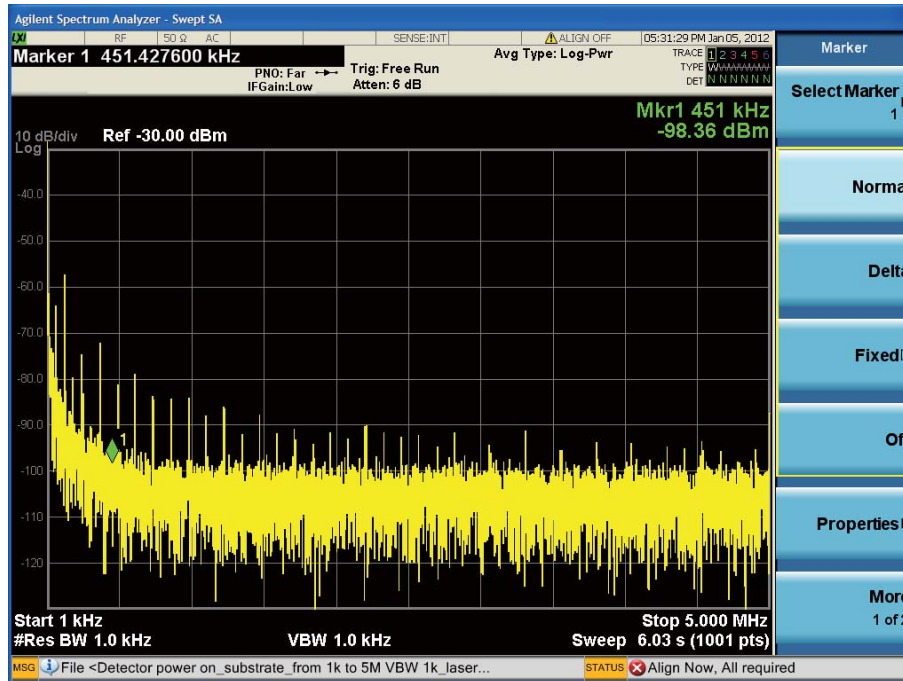


Figure 3.17: Electrical noise with detector and laser beam on membrane resonator. Spectral noises with large amplitude can be seen by noise spectral measurement. we can observe the spectral peaks with higher amplitude at the same frequency of spectral noise peaks measured in previous measurement done without directly incident laser beam on PD

To observe the effect by substrate in measurement of doubly-clamped mechanical resonator, we measured the noise peaks within the range from 10 Hz to 15 MHz. In this case, probing laser is focused on the surface of mechanical resonator at the clamping point. Thus, intensity of reflected laser beam is reduced compared to the noise measurement using Si_3N_4 membrane resonator. In this case, we can observe the increased intensity fluctuation in the noise floor and small peaks in the low-frequency region which are also attributed to the laser intensity or frequency noise(Fig. 3.18). In case of measurement of signal with infinitesimal amplitude, to find the exact frequency of mechanical mode of resonator and precise measurement spectral response, we should identify and discriminate these peaks after measurement

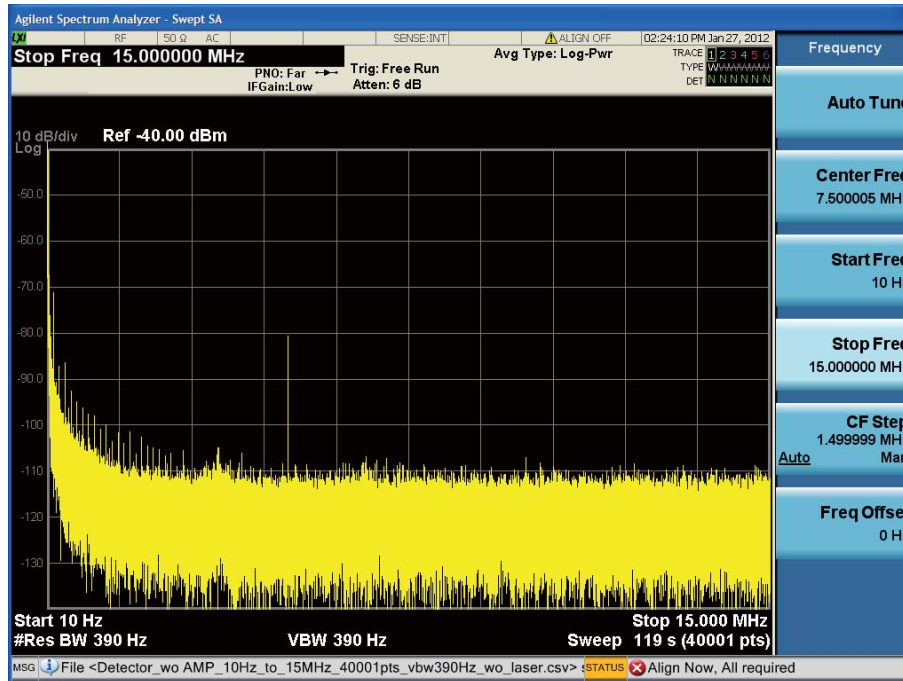


Figure 3.18: Electrical noise with detector and laser beam on substrate. By measuring the spectral noise from PD, we can find that electrical noise from PD and frequency(or intensity) noise exist. To find the exact resonant frequency of mechanical resonator and precise measurement with small amplitude by infinitesimal displacement of mechanical resonator such as thermal motion, we should identify and discriminate these peaks after measurement of spectral responses of mechanical resonator.

of spectral responses of mechanical resonator. During the measurement of thermal self-oscillation, mode-splitting, and mode-amplification which will be described at different chapter of this thesis, optical measurement was done after confirming these spectral noises.

To investigate the effect by electrical amplifier, we measured the noise spectrum by using with electrical amplifier. Due to the amplification of electrical signal, noise floor is also increased and become flat compared to the case without electrical amplifier. In the low-frequency region, noise signals from He-Ne lasers are amplified and clearly identified when compared to the measurement done without electrical amplifier(Fig. 3.19). In case of exper-

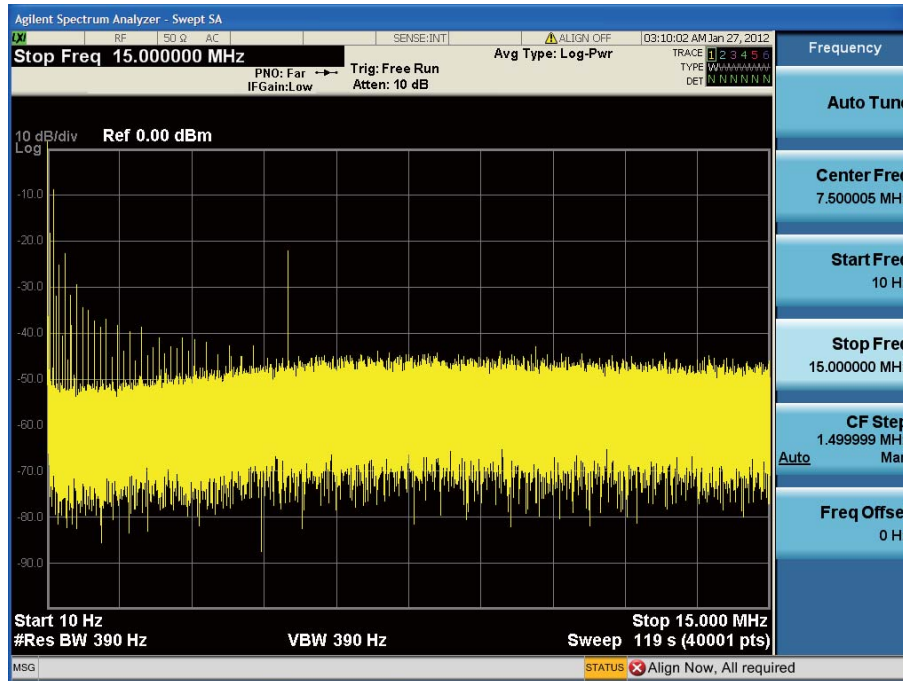


Figure 3.19: Electrical noise with electrical amplifier and optical set-up. To find the effect of additional electrical amplifier during the measurement of infinitesimal signal such as higher mode resonant response of mechanical resonator, electrical amplifier should be included. From the measurement of spectral noise with amplifier, we can observe the added noise and amplification of noise by external amplifier.

iment to measure the spectral response of mechanical resonator with very small amplitude, which can be observed during the measurement of thermal self-oscillation, higher-mode excitation, and sideband-assisted response of thermal-mode, external amplifier is essential tool. Thus, to discriminate added electrical noise and identify the small resonant responses of mechanical resonator, we should first investigate the spectral noise with all electrical and optical components.

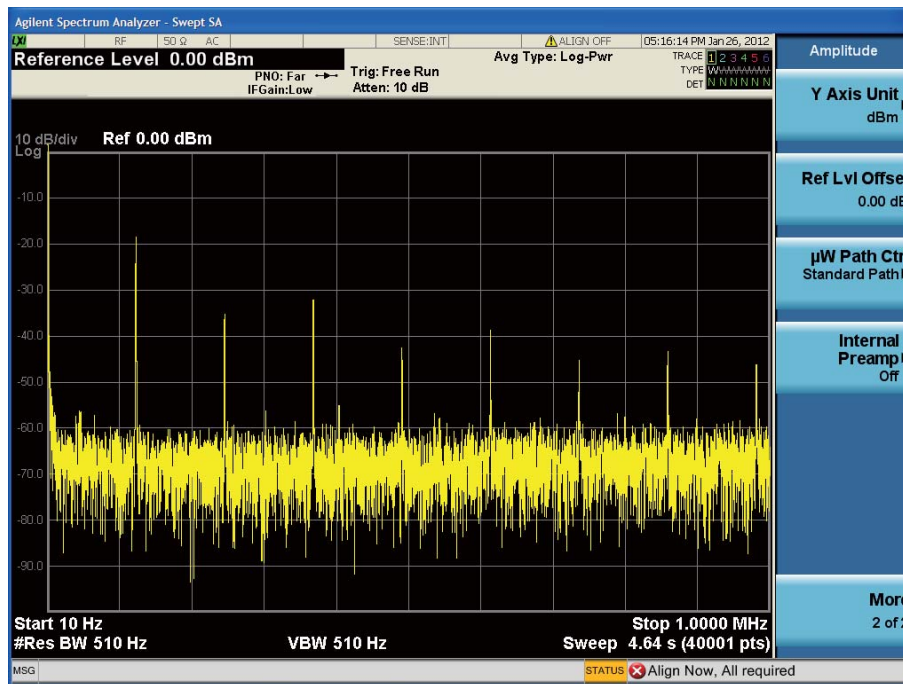


Figure 3.20: Detailed noise with full electrical and optical measurement set-up. Detailed spectral noise is measured in the range from 10 Hz to 1 MHz. Regular peaks with same interval are attributed to the noise from the function generator or rf-signal generator.

3.3 Field gradient actuation of doubly-clamped mechanical oscillator with on-chip electrode

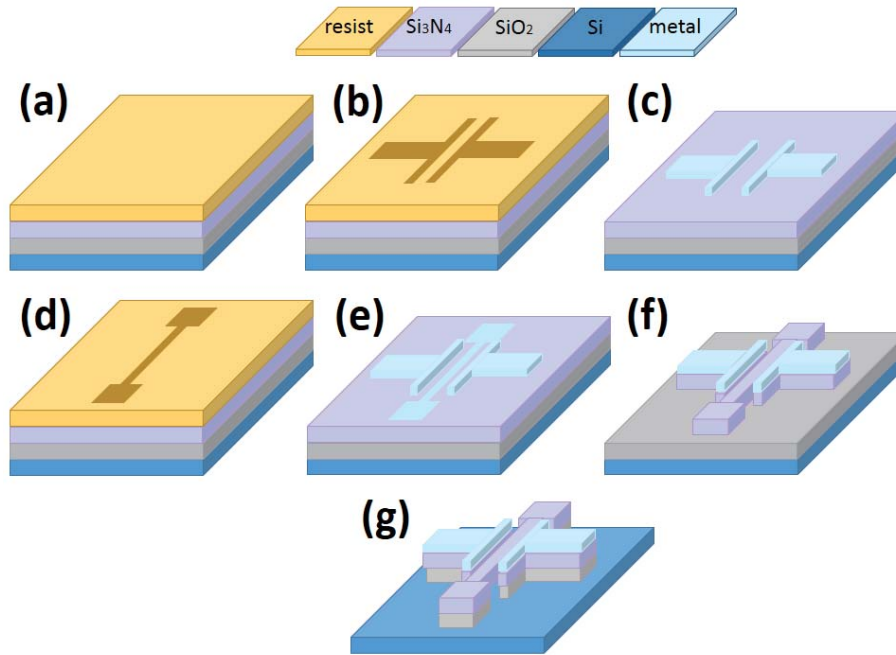


Figure 3.21: Fabrication process for on-chip electrode and mechanical resonator. (a) Coating of PR (b) Patterning of electrode by E-beam lithography (c) Metallization following developing process (d) PR coating and patterning of mechanical resonator (e) metallization of mask pattern for RIE etching process (f) RIE etching process to remove Si_3N_4 layer except resonator and electrodes (g) Removal of sacrificial SiO_2 layer by BOE

Polarizable materials which are placed in an inhomogeneous or asymmetric electrical field can feel force by dielectric interaction between polarized material and surrounding electrical field. This scheme can be extended to the micromechanical and nanomechanical structures. By applying V_{DC} to polarize mechanical resonator from dielectric material, we make dielectric interaction between electrical field and polarized mechanical resonator. By

mixing small rf-signal to V_{DC} we can introduce the dielectric force which can actuate the mechanical resonator to direction of asymmetric field. This scheme can be used in high-frequency operation of mechanical resonator. Furthermore, this scheme do not need any additional components on the mechanical oscillator, it can enable the operation of mechanical resonator with high- Q .

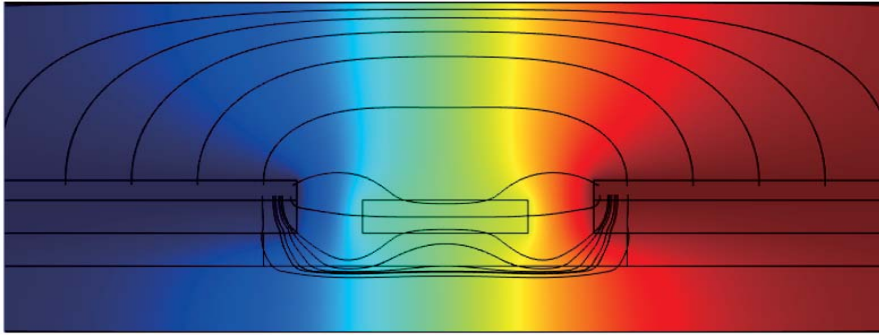


Figure 3.22: Numerical simulation of electrical field by on-chip electrode by Finite Element Analysis (COMSOL 4.3b) By applying V_{DC} between two electrode, we can generate the electrical field around the mechanical resonator. Due to the level difference between mechanical resonator and metal electrode, mechanical resonator is positioned slightly away from the equilibrium position inside the electrical field. Substrate and dielectric sacrificial layer (SiO_2) can also help to make asymmetric electrical field

To make the asymmetric electrical field around the mechanical resonator, we adopted the more simpler geometry which do not affect the dimensions of mechanical resonator. By positioning the electrode on the Si_3N_4 layer, which is also used to realize to oscillating component, we can generate asymmetric electrical field in the vicinity of mechanical resonator. As there is a level difference between mechanical resonator and electrode, which is exactly the thickness of Si_3N_4 , mechanical resonator is positioned slightly away from

the equilibrium position in the electrical field. This asymmetric field induces attractive force on mechanical resonator toward the electrode. We can induce resonant motion of mechanical resonator by applying rf-signal to the V_{DC} which is applied to polarize the mechanical resonator.

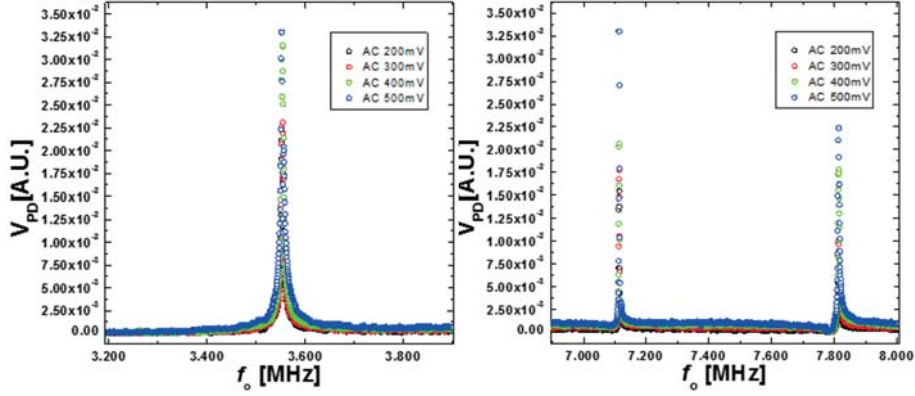


Figure 3.23: Resonant motion of doubly-clamped mechanical resonator actuated by on-chip electrode. By using the on-chip electrode deposited on the Si_3N_4 , we can apply asymmetric electrical field and rf-signal to mechanical resonator. Fundamental mode has resonant frequency of approximately 3.54 MHz (left). 2nd and 3rd mode(right) can be observed at 7.11 MHz and 7.81 MHz.

To actuate the mechanical resonator more efficiently, we should reduce the gap between mechanical resonator and electrode. Because of the limitation in E-beam lithography technique, we approached the electrode to the mechanical resonator less than 500 nm gap. Although we tested the effect of thickness of metal electrode for generating electrical field, we could not find significant difference due to thickness.

3.4 Field gradient actuation of doubly-clamped mechanical oscillator with off-chip electrode

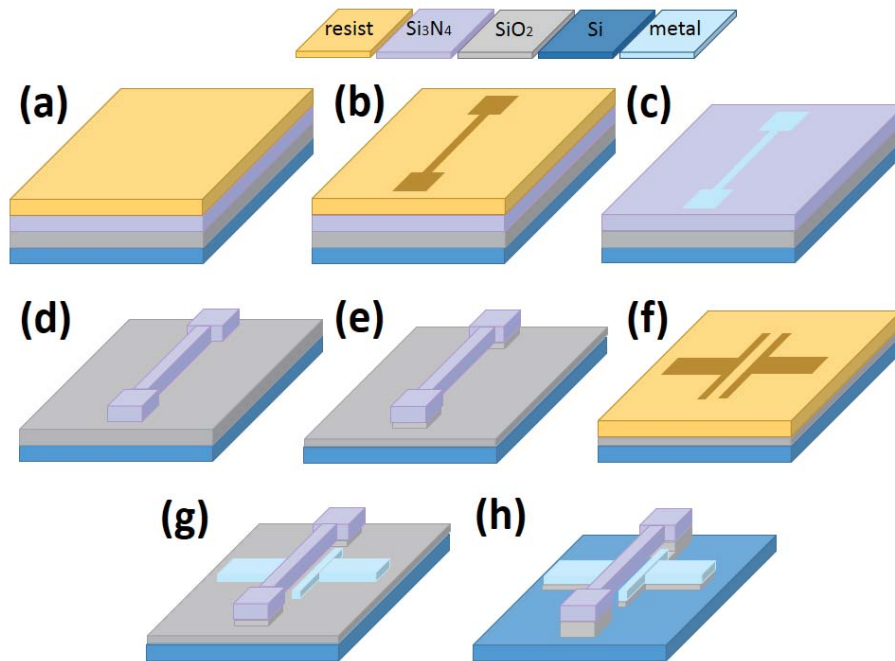


Figure 3.24: Fabrication process for off-chip electrode and mechanical resonator. (a) Coating of PR (b) Patterning of mechanical resonator with E-beam lithography (c) Metallization of mask pattern for RIE etching process (d) RIE etching process to remove Si_3N_4 layer except resonator (e) Partial removal of sacrificial SiO_2 layer for level difference between mechanical resonator and electrode by BOE (f) Coating of PR and patterning of electrode by E-beam lithography (g) Metallization of metal electrode (h) Removal of remaining sacrificial SiO_2 layer by BOE

On-chip electrode scheme which is described in previous section can be easily realized with less fabrication step. But due to the difficulties to make larger level difference which only depends on the thickness of Si_3N_4 layer, there are some limitations in applying high-power pumping or efficient actuation. To overcome this challenges, out of plane electrode should be real-

ized with the level difference which can maximize the electrical field gradient force.

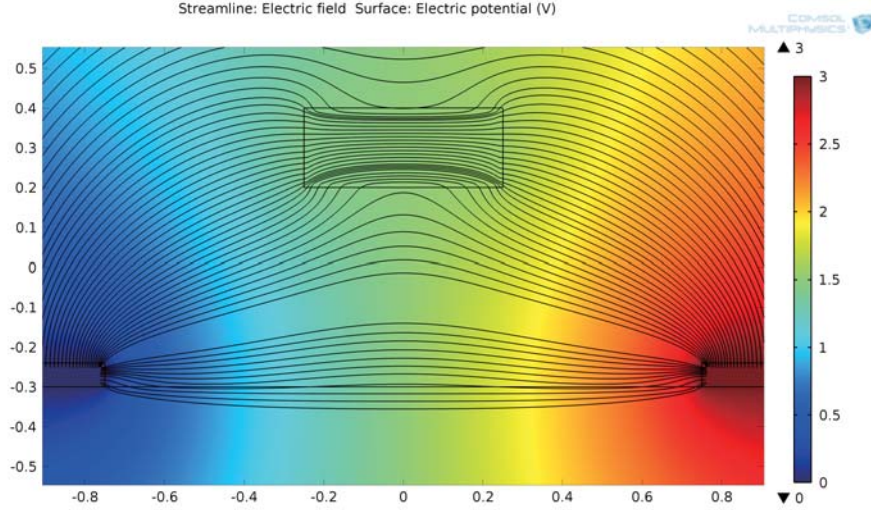


Figure 3.25: Numerical simulation of electrical field by off-chip electrode. By applying V_{DC} between two electrodes, we can generate the electrical field around the mechanical resonator. Due to the enlarged level difference between the mechanical resonator and the metal electrode, the mechanical resonator is positioned relatively far away from the equilibrium position inside the electrical field compared with the on-chip electrode scheme in the previous section. The effect of the substrate and dielectric sacrificial layer (SiO_2) can be neglected compared to the effect of the level difference between the electrode and the mechanical resonator.

By positioning the electrode on the SiO_2 layer after partial etching by BOE, we can realize a level difference between the mechanical resonator and the electrode, which is bigger than the thickness of the Si_3N_4 layer. By positioning the electrode underneath the mechanical resonator, we can generate a stronger asymmetric electrical field in the vicinity of the mechanical resonator compared to the on-chip electrode scheme. With a stronger asymmetric electrical field around the mechanical resonator, we can actuate the mechanical resonator with a smaller amplitude of rf-signal.

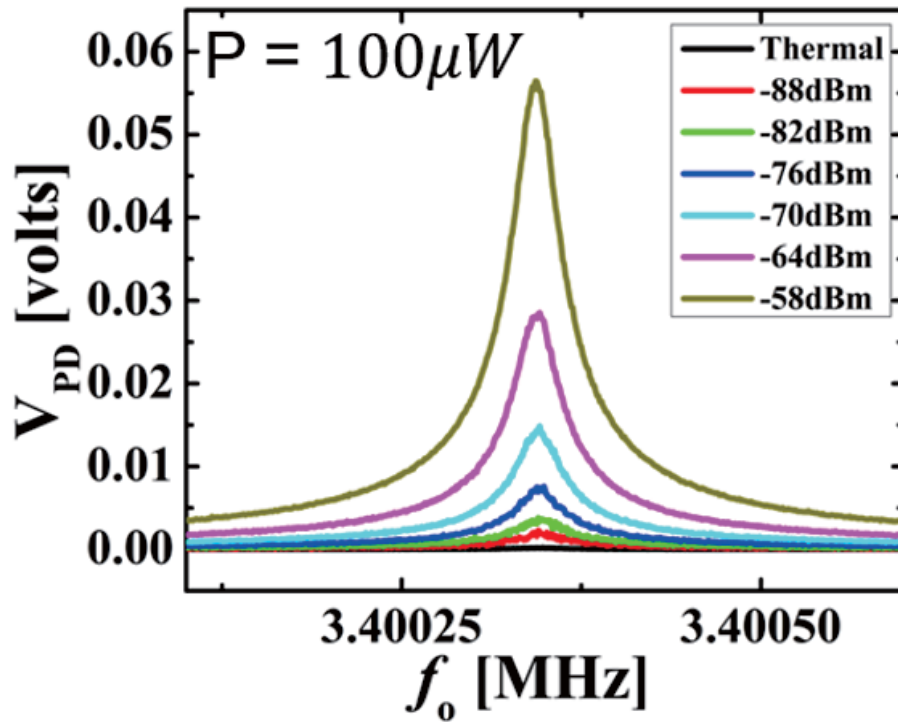


Figure 3.26: Resonant response of fundamental mode of mechanical resonator to applied pumping rf-signal by off-chip electrode. Due to the level difference between mechanical resonator and metal electrode, mechanical resonator can be actuated more efficiently and sensitively. Compared to the response of mechanical resonator by on-chip electrode, off-chip electrode can drive mechanical resonator by electrical field gradient force with smaller power of applied rf-signal

3.5 Field gradient actuation of membrane mechanical oscillator with on-chip electrode

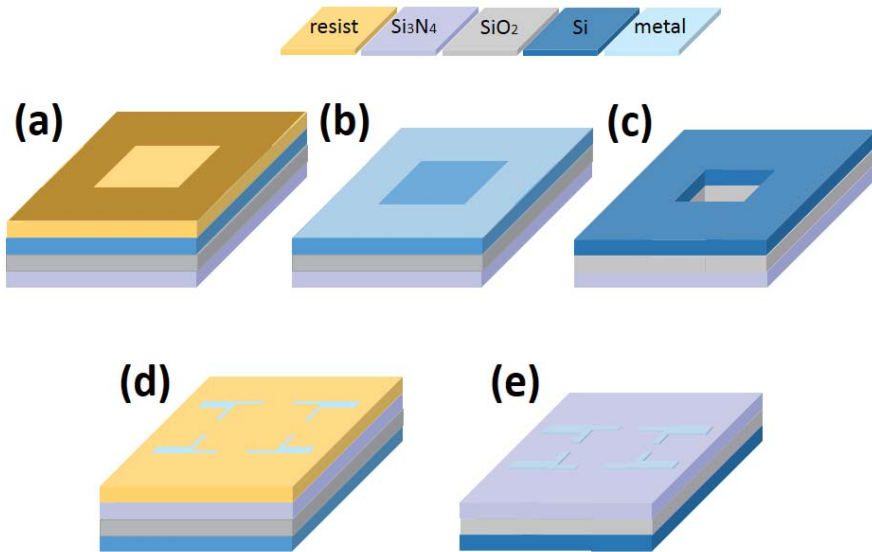


Figure 3.27: Fabrication process of membrane resonator with electrodes for electrical field gradient actuation (a) Coating of PR and patterning of etch-window on the back side (b) RIE etching process for removal of Si₃N₄ and SiO₂ layer on the backside (c) Removal of Si substrate and SiO₂ sacrificial layer (d) Coating of PR and patterning of electrode (e) Metallization of metal electrode

Electrical field gradient actuation scheme can be applied to the membrane resonator which can not accommodate electrode structure on the mechanical resonator. To induce asymmetric electrical field on the membrane resonator, we placed metal electrode next to the membrane resonator. With the same scheme of doubly-clamped mechanical resonator with on-chip electrode, electrode generate the asymmetric electrical field. Polarized membrane resonator

feels attractive force towards the vertical direction to the surface of resonator structure. Due to the larger mass and clamping area, larger attractive force is needed to actuate the membrane mechanical resonator, Thus, amplitude of V_{DC} applied to membrane resonator should be higher than doubly-clamped resonator and rf-signal with higher amplitude is also needed for actuation.

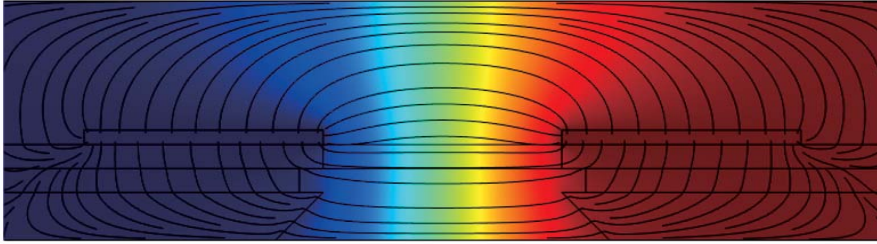


Figure 3.28: Numerical simulation of electrical field by on-chip electrode on membrane mechanical resonator. By applying V_{DC} between separated for electrodes, we can generate the electrical field around the membrane resonator. Due to the level difference between mechanical resonator and metal electrode, membrane resonator is also positioned slightly away from the equilibrium position inside the electrical field and feels attractive force. Due to the larger mass and clamping area, displacement of membrane mechanical resonator is smaller than the displacement by doubly-clamped mechanical resonator

By using the electrical field gradient actuation technique, we can control the the resonant motion of membrane resonator without additional component on the resonating structure. Additional structure on the membrane resonator can degrade mechanical and optical properties of mechanical resonator. And enlarged surface area of mechanical resonator by removing those components, we can use the full surface of resonator and access the resonator from the back-side.

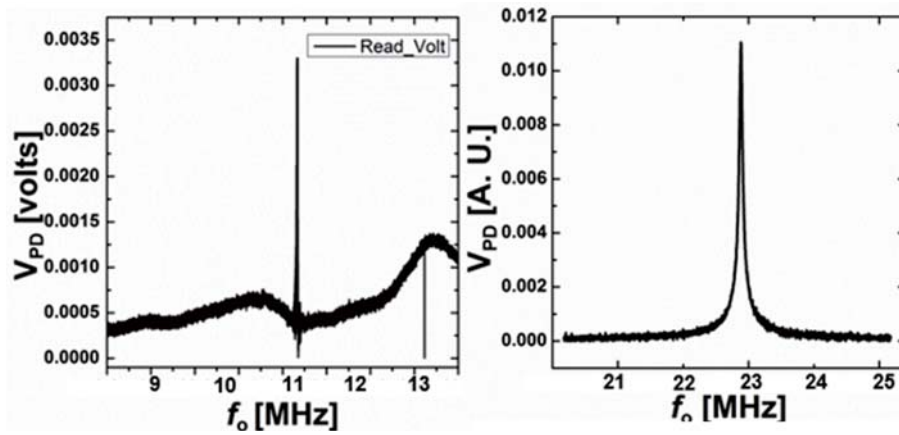


Figure 3.29: Resonant response of membrane mechanical resonator. On-chip electrode in the vicinity of suspended membrane can apply V_{DC} to polarize and actuate the membrane resonator. Due to the geometry of mechanical resonator and stress, fundamental mode(left) and 2nd mode have higher resonant frequency compared with the doubly-clamped mechanical resonator with same length or longitudinal dimension. Square-type membrane resonator of 40 micron-long side shows fundamental resonant motion at 11 MHz and 2nd mode at 22.8 MHz

Chapter 4

Nonlinear parametric amplification of mechanical resonator with high quality factor by electrical field gradient pumping¹

4.1 Introduction

As size of device is reduced to sub-nanometer scale by development of nanofabrication technique, consequently, mechanical devices like MEMS and NEMS devices have been also fashioned into ever-smaller dimensions. Accordingly, transductional motion generated by mechanical oscillation of device under test is reduced down even to the level atomic scale displace-

¹Works presented in this chapter has been published in: "Electrical field gradient pumping of parametric oscillation in a high-frequency nanoelectromechanical resonator", *Japan Journal of Applied Physics*, 51, 074003 (2012)

ment. Thus, displacement signals from mechanical resonator also become ever-finer. For precise measurement for such small signals, it is still a challenge with the state-of-the-art measurement techniques as optical, electrical and so on.

Furthermore, both intrinsically and extrinsically, mechanical resonator at reduced dimension are more susceptible to dissipation of energy in device by their small dimension and increased surface to volume ratio. To realize more precise control, measurement, low energy consumption, and higher frequency operation, implementation of high- Q in micro- and nano-mechanical device should be achieved.

Therefore, development of signal amplification and high-frequency actuation with minimized dissipation become more important in NEMS. For amplification of displacement amplitude in signal by mechanical resonator, nonlinear parametric amplification phenomena was adopted firstly by Rugar. [30] Following Rugar's seminal report on amplification of mechanical displacement by parametric amplification, number of different attempts to amplify small responses of mechanical resonator by nonlinear parametric amplification have been investigated and realized. [19] [27] [32] [34] [92] [93] [94]

To realize the oscillatory structure with mechanical high- Q , investigation of efficient actuation and measurement technique NEMS started with the development of nanomachining in many different shapes of geometry such as beams, cantilevers, and membranes. Numerous actuation techniques have been developed to effectively excite the mechanical resonator such as capacitive, [20] piezoelectric, [21] magnetomotive, [19] electro-thermal, [26] and so on. Although some success could be achieved by those actuation technique, these techniques have also shown some constraints in material selectivity, difficulties in fabrication processes and compatibility with measurement tech-

niques. Furthermore, additional structures which should be implemented in mechanical resonator for actuation can act as important source of dissipation. Although photothermal, [95] and inertia-based piezoelectric actuation scheme [96] have been developed to overcome such constraints, there remain some disadvantages such as difficulty in high frequency operation and integration with resonator of mechanical high- Q .

To resolve those obstacles in realizing mechanical device which can accommodate high-frequency operation with mechanical high- Q and amplification of signal of displacement, we applied nonlinear parametric amplification phenomenon to mechanical resonator. Electrical field gradient actuation scheme made it possible to excite resonant motion with high quality factor and high frequency operation. Using a set of separated on-chip electrodes, we polarize and actuate a dielectric resonator under an electrical field gradient with simple voltage tuning of the mechanical resonance. By applying a signal twice the resonant frequency, $2f$ to the dielectric resonator simultaneously, mechanical resonator shows parametric oscillation and damping depending on relative phase. Mechanical resonator fabricated from high-stress stoichiometric silicon nitride has mechanical Q factor above 20,000, which enabled the parametric oscillation of mechanical resonator with modulation of mechanical resonator's spring constant by applied periodic voltage signal.

4.2 Mechanical Resonator with double electrode geometry

To accommodate mechanical resonator with mechanical high- Q factor, we designed and fabricated doubly clamped mechanical resonator with two sets of electrodes to accommodate different input RF signal.

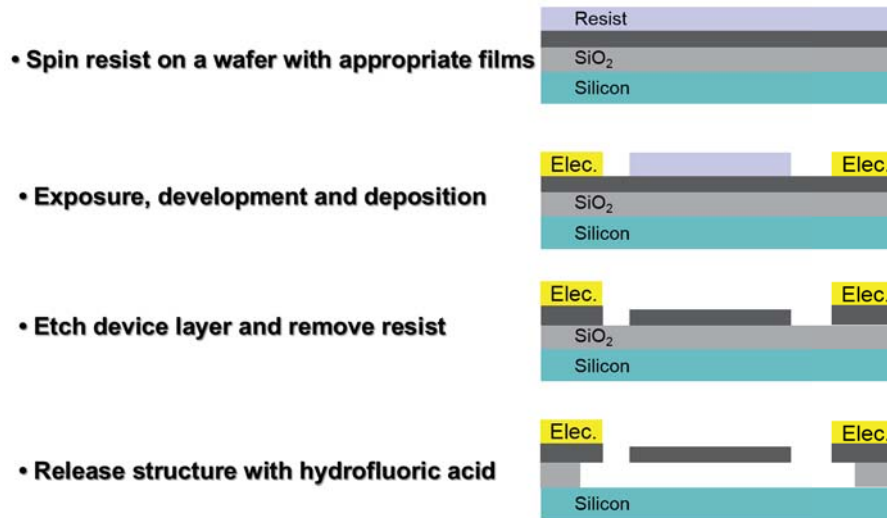


Figure 4.1: Cross sectional view of step by step fabrication process. From top to bottom of figure, each step is processed to suspend mechanical resonator with 4 different side-electrodes

Mechanical resonators are fabricated from high-stress or stoichiometric silicon nitride (Si_3N_4) thin film of 200 nm thickness. Silicon Dioxide (SiO_2) layer beneath the Si_3N_4 has a thickness of 500 nm grown on Si substrate ($\sim 500 \mu m$). SiO_2 layer serves as a sacrificial layer to suspend mechanical resonator structure. Two sets of electrodes (Fig. 4.1 and 4.2) for electrical field gradient actuation at resonant frequency (f_o) and pumping frequency ($2f_o$) are patterned utilizing conventional e-beam lithography techniques using NPGS (Nanometer Pattern Generation System) and SEM (Tescan Vega). Lateral distance between electrodes in same set for resonant driving at (f_o) is designed to be 3 μm to make 500 nm gap between mechanical oscillator (width = 2 μm) and each electrode. After developing the PMMA coated on the sample following e-beam lithography process, The Ti/Pd (10 nm /70 nm) double layers are deposited to deliver the electrical field gradient force around the resonator. After deposition of metal electrodes, second e-beam lithography process to define the of mechanical resonator is followed. After

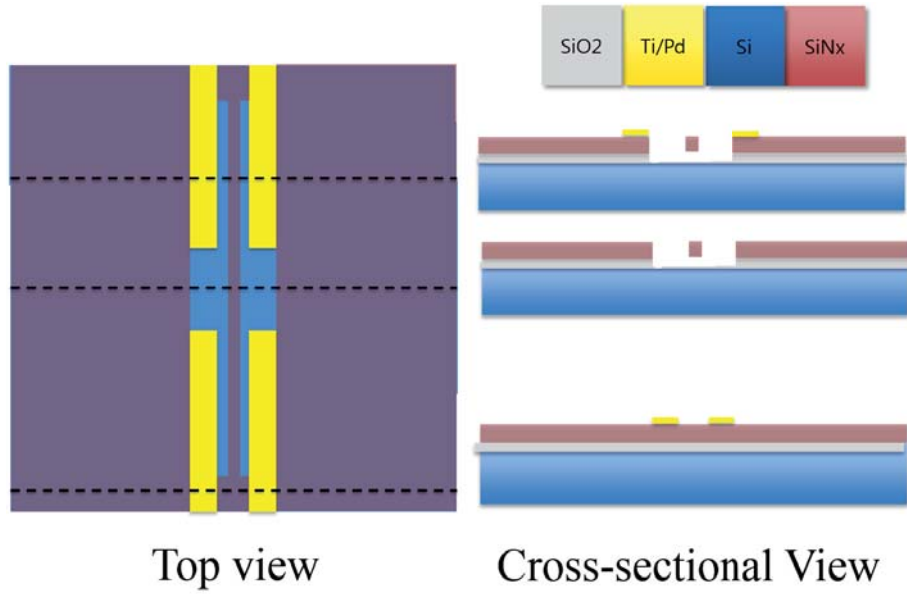


Figure 4.2: Cross sectional view at different position on device. 4 electrodes are fabricated to apply two different rf signal to mechanical device. Each electrodes are connected to electrical pad(not shown here) and each electrical pads is wire-bonded to connector which can be accessed by external signal or function generator via rf cable

deposition of Cr of 40 nm thickness for masking resonator structure while Reactive Ion Etching process (RIE), mechanical resonator pattern is transferred by typical RIE process for etching out Si_3N_4 except electrode and resonator structure. Finally, we suspend mechanical resonator from Si_3N_4 by removing the sacrificial SiO_2 layer with buffered oxide etchant (BOE) while controlling the etching depth by time. Dimension of the resonator is 40 μm in length, 2 μm in width and 200 nm in thickness as shown in the scanning electron micrograph (Fig. 4.3).

For dielectric force generation, the structure should be placed in the different plane to make asymmetric field gradient around the resonator. In our device, electrode is patterned and deposited on the Si_3N_4 and the gap be-

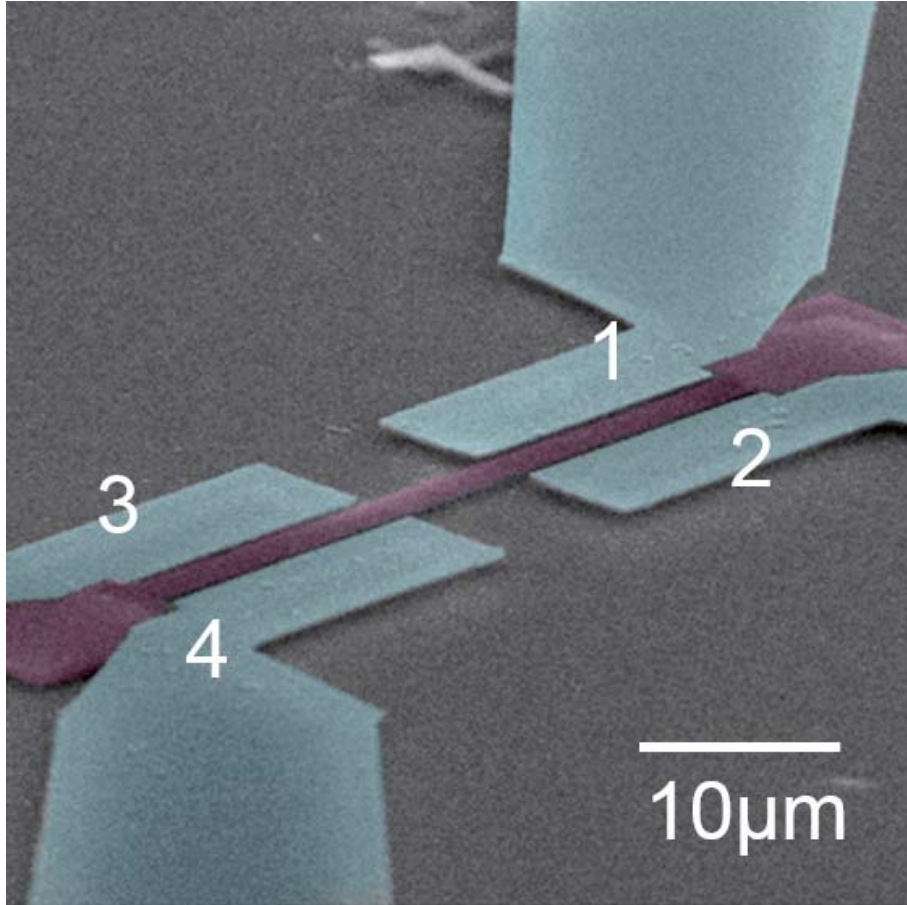


Figure 4.3: Scanning electron micrograph with faked color for different components after finishing all fabrication process. 4 electrodes(blue) are fabricated to apply 2 different rf signal. electrode 1 and electrode 2 are composing set to apply resonant driving signal (f_o) and electrode 3 and 4 for applying parametric pumping signal of ($2f_o$) frequency. Mechanical resonator (purple) is suspended after etching SiO_2 . Each electrodes are connected to connector which can be accessed by external signal or function generator via rf cable

tween bottom of the resonator and bottom of the electrode is the same as the thickness of the mechanical resonator (200 nm).

4.3 Actuation and measurement scheme of oscillation in mechanical resonator

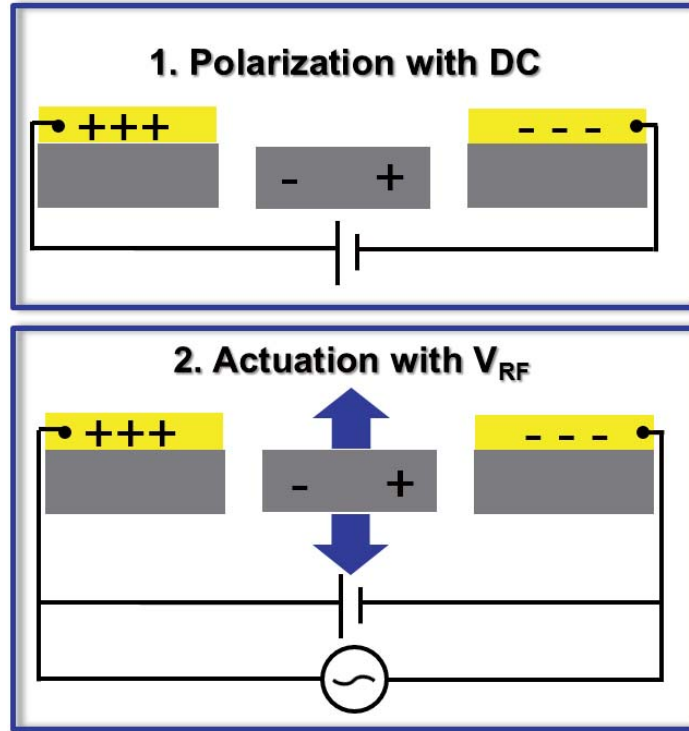


Figure 4.4: Schematic diagram of mechanical resonator excitation by electrical field gradient force. Electrodes are fabricated and deposited on the Si_3N_4 layer of same level with mechanical resonator. DC voltage (from -30 V to 30 V in real experiment) is applied to side electrode to polarize the dielectric mechanical resonator. Small (compared to the amplitude of applied DC voltage) rf signal around the resonant frequency of mechanical resonator is combined with DC voltage and applied to the electrode. Small rf signal (from \sim mV to \sim 1 V) perturb the electrical field around the mechanical resonator and mechanical resonator feels force in to the vertical axis.

To actuate the mechanical resonator from Si_3N_4 , Dielectric interaction between electrical field which is generated by one set of electrodes and the resonator polarized by applied DC voltage between electrode. By applying DC bias in the electrodes, the resonator was electrically polarized. By the dipole interaction between electrical field and dipole moment in the me-

chanical resonator, the resonator feels attractive force toward the direction of strong electric field and this force bends the resonator to the new initial position.

In addition to the applied DC bias, the relatively small (compared to amplitude of DC voltage) RF signal is applied to modulate the electrical field for resonant driving of the structure. By sweeping the frequency of rf signal around the resonant frequency, we can observed the resonant response and amplitude of resonant displacement of mechanical resonator. The resonator oscillated in transverse mode with as small as 1 mV_{rms} modulating AC signal. The schematic diagram for the transverse mode driving is depicted in Fig. 4.5.

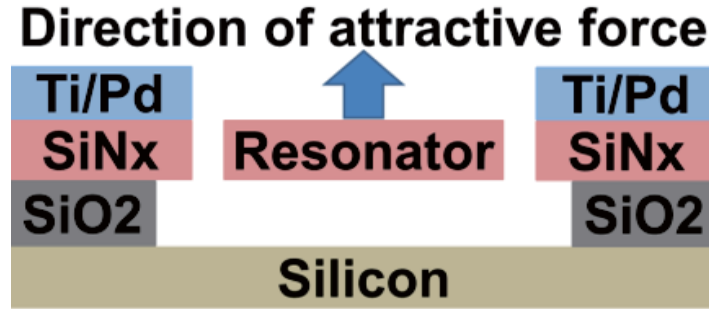


Figure 4.5: Schematic diagram of device operation and realized structures. Ti/Pd metal electrode apply V_{DC} and AC electrical field around the mechanical resonator

The response of the mechanical resonator by resonant and parametric pumping signal is measured by optical reflectance measurement scheme. The intensity stabilized He-Ne laser (Research Electro-Optics inc., Model 39727, wavelength = 632.8 nm) is focused on the mechanical resonator by long-working distance objective lens (by Mitutoyo Co.). Intensity-stabilized laser can reduce the effect of intensity noise from the laser and prevent the intensity fluctuation by varying laser power. Reflected laser beam from the surface

is delivered to the photo-detector (Menlo Systems, FPD-510FV) to record the information of mechanical resonance. Herein, we utilize typical lock-in technique in measuring the response of mechanical resonance according to applied RF signal from function generator. As the Si_3N_4 doubly-clamped mechanical resonator does not have metal electrodes or other materials on the oscillatory structure and intrinsic mechanical tensile stress, the resonator showed very high mechanical- Q which was measured to be over 22,000 at room temperature under modest vacuum (1.7 mTorr).

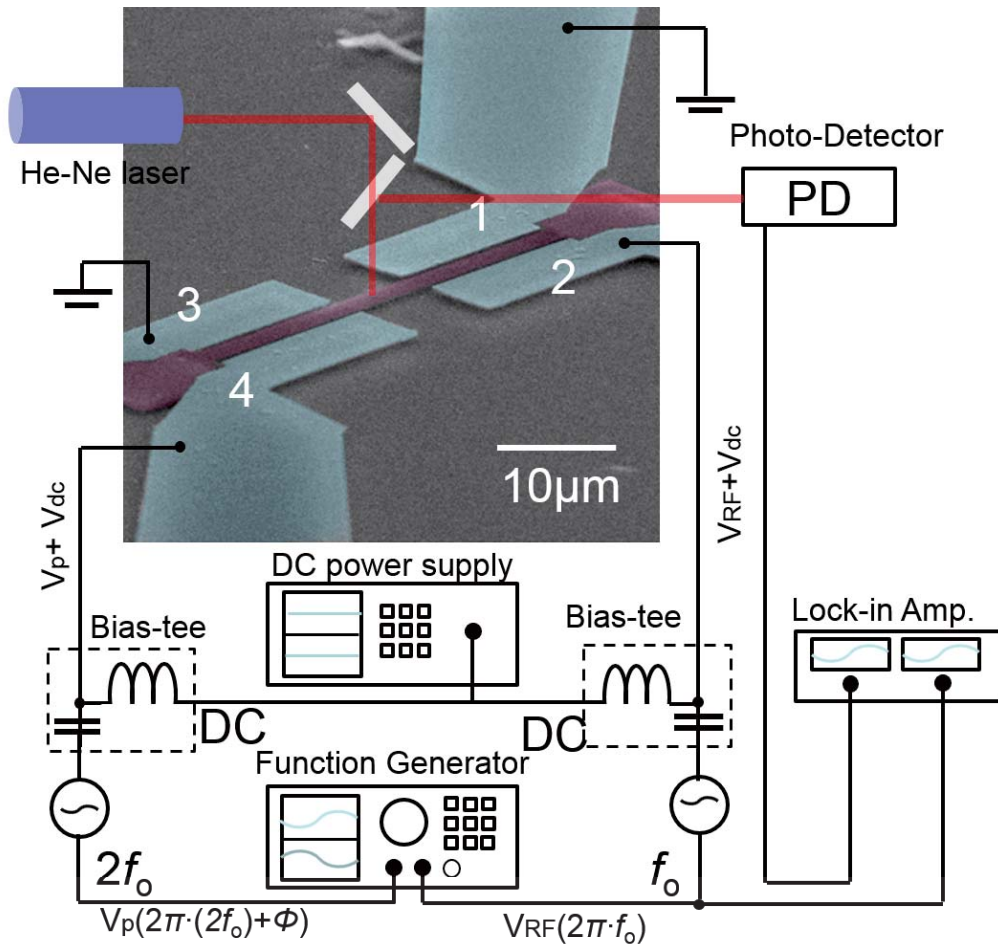


Figure 4.6: Actuation and measurement strategy to excite and investigate the nonlinear parametric amplification in mechanical resonator. Intensity-stabilized laser beam is focused on the mechanical resonator and reflect back to the photo-detector. Output signal from photo-detector goes into the input port of lock-in amplifier and lock-in amplifier compare input signal from photo-detector with reference frequency which comes from RF function generator. By using the function generator which has a function to control the relative phase between two output rf signal, rf signal (f_0) to excite the resonant motion of mechanical resonator is applied to mechanical resonator (electrode 1 and electrode 2) and parametric pumping signal with twice the resonant frequency ($2f_0$) and phase shift (ϕ) is applied to the other set of electrode (electrode 3 and electrode 4). Each rf signal is combined with DC voltage which comes from the DC power supply to polarize the mechanical resonator

4.4 Theoretical background for nonlinear parametric oscillation of mechanical resonator

The equation for damped harmonic oscillator with parametric excitation can be described as following equation. [80]

$$m \frac{d^2 x}{dt^2} + \frac{m\omega_0}{Q} \frac{dx}{dt} + [k_o + \delta k_o \sin \omega_p t] x = F_o \cos(\omega_d t + \theta) \quad (4.1)$$

where $x(t)$ is the displacement of the oscillator at time t , m is the mass, ω_o is the resonant frequency of mechanical resonator at given bias voltage, k_o is the spring constant which is related to the mechanical resonant frequency and mass of mechanical resonator by $k_o = m\omega_o^2$, ω_p is the frequency of the parametric pumping signal, ω_d is the frequency of resonant driving signal for mechanical resonator, Q is the mechanical quality factor, and θ is the relative phase difference between ω_d and ω_p .

Using the normal-mode approach described by Louisell [29] for electrical parametric amplifier and Rugar [30] for adaptation to mechanical system, we can introduce following transformation of equation.

$$a = \frac{dx}{dt} + j\omega_1^* x, \quad (4.2)$$

$$a^* = \frac{dx}{dt} - j\omega_1 x, \quad (4.3)$$

where $j = \sqrt{-1}$ and

$$\omega_1 = \omega_o [(1 - 1/4Q^2)^{1/2} + j/2Q] \quad (4.4)$$

The inverse transformations are

$$x = \frac{a - a^*}{j(\omega_1^* + \omega)}, \quad (4.5)$$

$$\frac{dx}{dt} = \frac{\omega_1 a + \omega_1^* a^*}{\omega_1^* + \omega_1} \quad (4.6)$$

By substituting 4.5 and 4.6 into 4.1 and then with a series of algebraic manipulations, we can get the simplified equation of motion as follows.

$$\frac{da}{dt} = j\omega_1 a + j \frac{\delta k_o \sin \omega_p t}{m} \frac{a - a^*}{\omega_1^* + \omega_1} + \frac{F_o \cos(\omega_d t + \theta)}{m} \quad (4.7)$$

Now, we find the steady-state solutions of 4.7 which have the form of

$$[j(\omega_1 - \omega_o)A - \frac{\delta k_o}{2m(\omega_1^* + \omega_1)}A^* + \frac{F_o}{2m}e^{j\theta}]e^{j\omega_o t} \quad (4.8)$$

To the first order in $1/Q$, $\omega_1^* + \omega_1 \approx 2\omega_o$ and $\omega_1 - \omega_o \approx j\omega_o/2Q$, then we can find that

$$A = F_o \cdot \frac{Q\omega_o}{k_o} \left[\frac{\cos\theta}{1 + Q\delta k_o/2k_o} + j \frac{\sin\theta}{1 - Q\delta k_o/2k_o} \right] \quad (4.9)$$

If we re-write the motion of mechanical resonator as $x(t) = X_1 \cos \omega_o t + X_2 \sin \omega_o t$, then $x_1 = \text{Im}A/\omega_o$ and $X_2 = \text{Re}A/\omega_o$. The gain of the amplifier is

$$G(\theta) = \frac{|X|_{\text{pump on}}}{|X|_{\text{pump off}}} = \frac{|A|_{\text{pump on}}}{|A|_{\text{pump off}}} \quad (4.10)$$

where $|X| = (X_1^2 + X_2^2)^{1/2}$. Using 4.9, we can get the theoretical gain of parametric amplification.

$$G(\theta) = \left[\frac{\cos^2\theta}{(1 + Q \cdot \delta k_o/2k_o)^2} + \frac{\sin^2\theta}{(1 - Q \cdot \delta k_o/2k_o)^2} \right]^{1/2} \quad (4.11)$$

From 4.11, we can get the possible gain of parametric amplification with phase and $Q \cdot dk_o/k_o$ as variable.

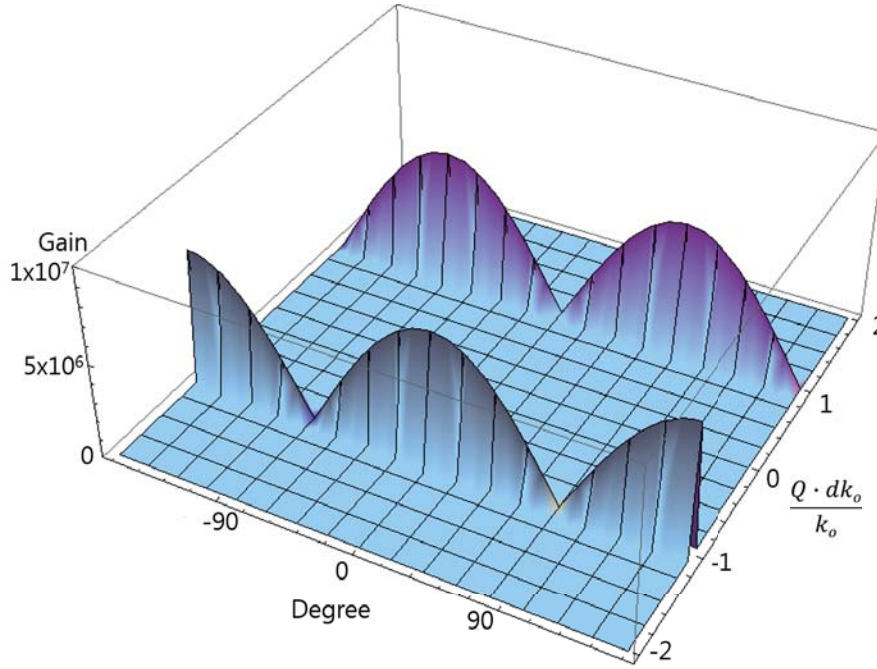


Figure 4.7: Gain of nonlinear parametric amplification in parameter space of phase θ and $Q \cdot dk_o/k_o$. For $Q \cdot dk_o/k_o$ as a variable for parametric amplification, maximum gain can occur only for $Q \cdot dk_o/k_o$ is -1 or 1. But in case of relative phase at 90 degree or -90 degree, gain of parametric amplification decreases to 0.5 and parametric damping occurs. To attain maximum gain with parametric pumping, relative phase between resonant driving f and parametric pumping $2f$ should be 0 and or $pm180$ degree. Even in this case, if we can tune the parameter $Q \cdot dk_o/k_o$ have 1, we can observe the parametric damping.

With Eq. 4.11 and θ and $Q \cdot dk_o/k_o$ as an independent parameter, we can estimate the possible gain by nonlinear parametric oscillation as shown in Figure 4.7. For a parametric gain at -90 degree and 90 degree, we can get a sharp gain as $Q \cdot dk_o/k_o$ approaches 1. In this case, the former term with $\cos\theta$

becomes 0, but the latter term with $\sin\theta$ increases to ∞ as $1 - Q \cdot dk_o/k_o$ approaches to 0. On the contrary, when phase θ is fixed at 0, the former term with $\cos\theta$ approaches to ∞ while the latter term with $\sin\theta$ becomes 0. In case of relative phase at 90, 0, and -90 degree, we can get parametric damping by tuning the other parameter $Q \cdot dk_o/k_o$. For relative phase of 0 degree, we can get maximum gain approaching ∞ with as $Q \cdot dk_o/k_o$ approached to -1. For $Q \cdot dk_o/k_o$ approaching to 1, we can get the gain of 0.5 by parametric pumping, which is parametric damping. For the relative phase of -90 degree and 90 degree, we can get maximum gain where $Q \cdot dk_o/k_o$ is -1. In case of 1 for $Q \cdot dk_o/k_o$, we can observe the decrease of gain and 0.5 is the minimum gain we can attain by parametric pumping.

To observe detailed phase dependent gain of parametric amplification with $Q \cdot dk_o/k_o$ from 0.9 to 0.99 with 0.01 step, we can see the parametric amplification and damping with different phase. While θ approaches to 0 or 180 degree, gain become lower than 1 and saturated to approximately 0.5, which is the parametric damping by parametric pumping in Fig 4.8. As θ increases from 0 to 90 degree, gain also increases from 0.5 to maximum value and decrease and $Q \cdot dk_o/k_o$ as a parameter for gain of parametric amplification. For $Q \cdot dk_o/k_o$, we can observe the dependence of gain on modulation of spring constant. With the $Q \cdot dk_o/k_o$ from 0.9 (blue with lowest amplitude) to 0.99 (purple with highest amplitude), as the amplitude of frequency modulation increase.

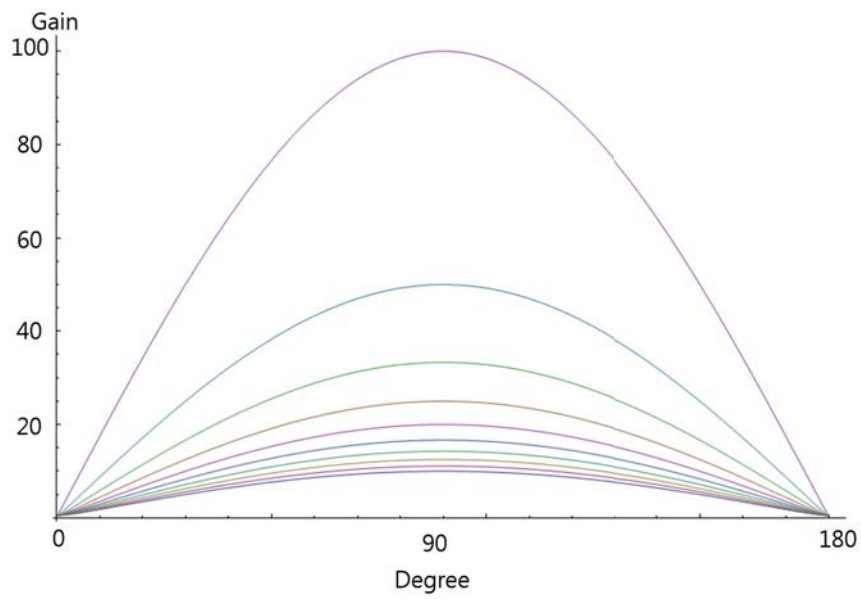


Figure 4.8: Gain of parametric amplification on phase different phase with $Q \cdot dk_o/k_o$ from 0.9 to 0.99 with 0.01 step. By increasing the $Q \cdot dk_o/k_o$, or by increasing the modulation of spring constant dk_o , maximum gain at phase 90 degree increases. For $Q \cdot dk_o/k_o$ near 0 or 180 degree, we can observe the parametric damping which reduces the gain of parametric amplification to approximately 0.5.

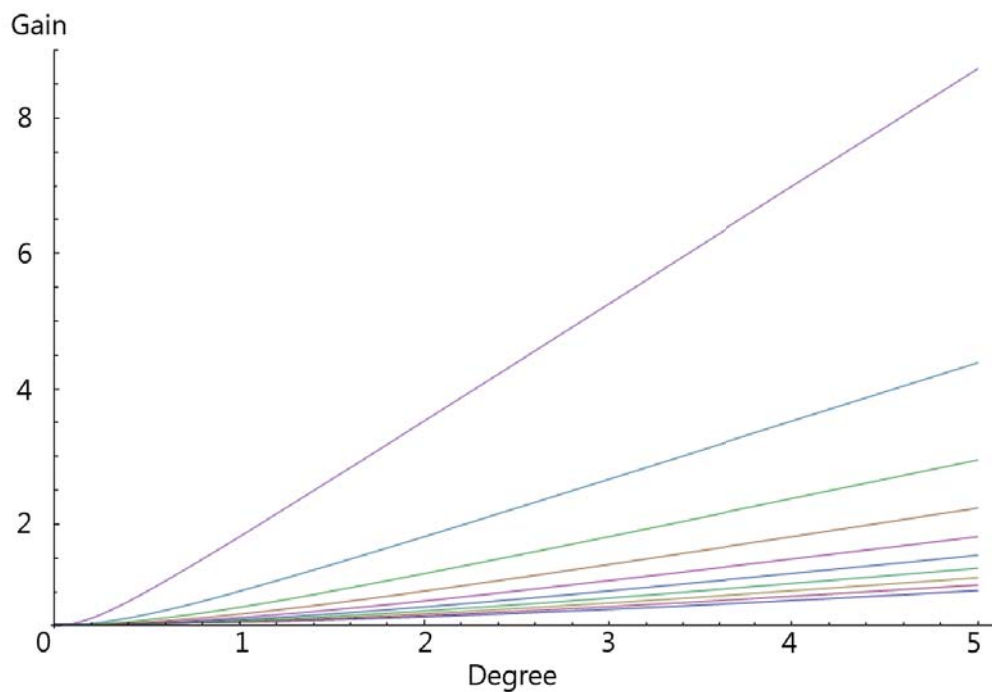


Figure 4.9: Deamplification by nonlinear parametric oscillation. For $Q \cdot dk_o/k_o$, we can get maximum gain when modulation of spring constant by tuning the dk_o to make $Q \cdot dk_o/k_o$ approach to 1. In this case, we can also observe parametric demaplification when phase difference θ is near 0 or 180 degree. With $Q \cdot dk_o/k_o$ from 0.9 (blue with lowest gain) to 0.99 (purple with highest gain) with 0.01 step, We can observe the parametric deamplification at phase difference θ near 0.

4.5 Pumping power dependence of parametric amplification

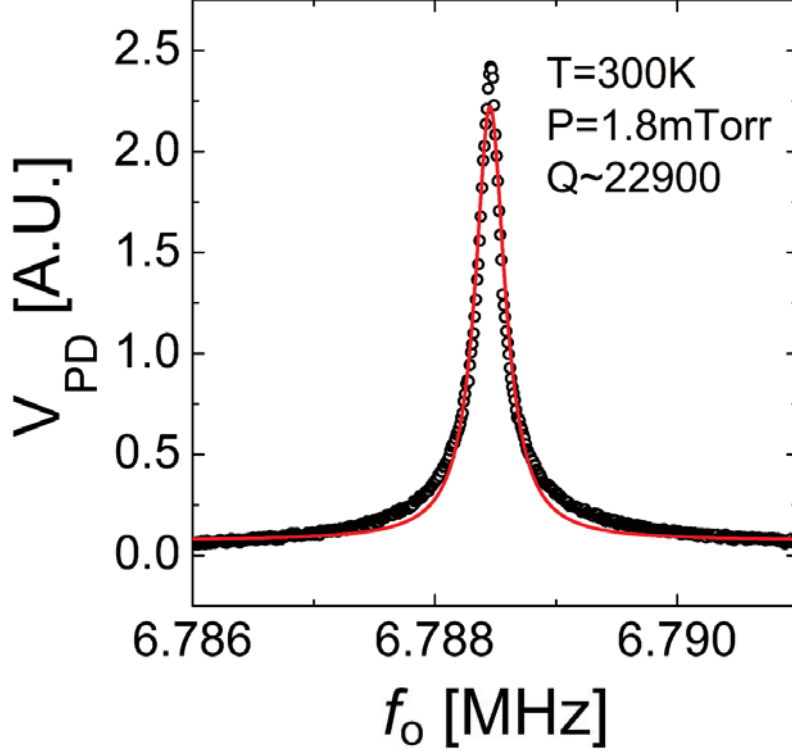


Figure 4.10: Resonant response of mechanical resonator at DC 20 V bias across the two electrodes with small RF signal of $1 mV_{p-p}$ amplitude. At 300 K temperature and 1.8 mTorr pressure, we could observe the resonant response of mechanical resonator at approximately 6.7882 MHz with mechanical quality factor of 22,900. Due to high mechanical tensile stress in Si_3N_4 , mechanical resonator shows high frequency operation compared with mechanical resonators from low-stress or stressless materials.

The response of the mechanical resonator is measured using an optical reflectance measurement scheme and a standard lock-in techniques. An intensity-stabilized He-Ne laser (wavelength = 632.8 nm) is focused on the resonator beam center and the reflected beam is delivered to a PD. Because of residual stress and the absence of a metal electrode on the resonating structure, the resonator shows a very high- Q of over 22,000 at room temper-

ature under a modest vacuum (1.7 mTorr). The resonant frequency with an applied $V_{dc} = 20$ V is approximately 6.79 MHz as plotted in Fig. 4.10

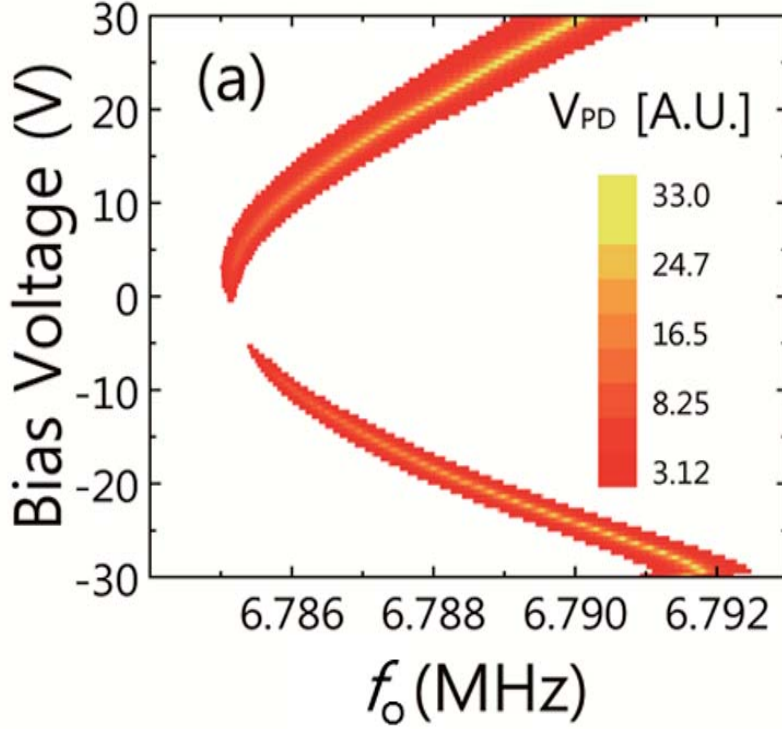


Figure 4.11: Quadratic tuning of resonant frequency of mechanical resonator by applied DC voltage. By dielectric interaction between dipole moment in mechanical resonator and electrode, resonant frequency of mechanical resonator can be tuned according to the V_{DC}^2 and direction of tuning is determined by the distance between electrode and dipole-moment on mechanical resonator

To investigate resonant frequency detuning and modulation of the spring constant of the resonator, we vary the V_{dc} from +30 V to -30 V as shown in Fig. 4.11. The minimum resonant frequency is found for $V_{DC} = 0$ V and initially increases quadratically with V_{DC} because of an increase of internal stress in the resonator. Note that there is a slight asymmetry to the resonant frequency detuning which we attribute to the electrical charging effects on the dielectric resonator by V_{dc} and imperfections of the fabrication process

(i.e., two-step alignment process between the electrodes and the beam resonator). The resonant frequency change shows the modulation of the spring constant by V_{dc} . At higher V_{dc} values, the resonant frequency shift becomes more linear with applied V_{DC} . To investigate the modulation of the spring constant, k , with the electric field in the linear regime, we measure the resonant frequency near $V_{DC} = 20$ V with an applied RF signal of 1 mV_{p-p} . Under these conditions, the measured frequency shift is 340 Hz/V .

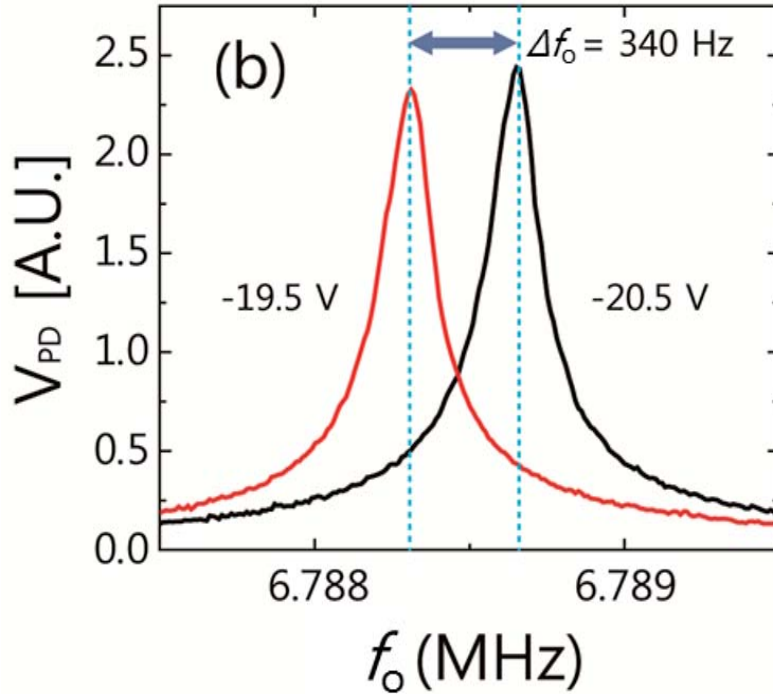


Figure 4.12: Tuning of resonant frequency of mechanical resonator by change of 1 V DC voltages. By increase of 1 V DC around 20 V from 19.5 V to 20.5 V, resonant frequency of mechanical resonator is tuned by approximately 340 Hz. This tuning can show the possibility of tuning spring constant by applying RF signal of sufficiently large AC voltage, which is sufficient to modulate the spring constant for parametric amplification and deamplification.

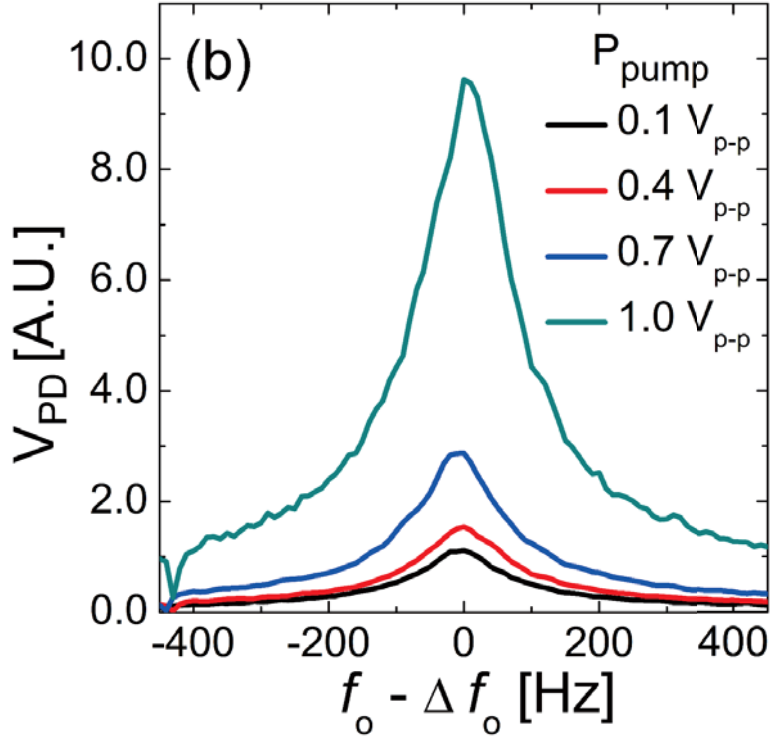


Figure 4.13: Amplification of resonant motion by parametric amplification with different pumping power of $2f$ at the same phase. To observe the pumping power dependency of the parametric amplification, parametric excitation signal of frequency $2f$, where f is the resonant frequency of mechanical resonator is applied to the mechanical resonator with different pumping power from $0.1 V_{p-p}$ to $1.0 V_{p-p}$ with $0.3V$ step. As pumping power increase, amplitude of resonant peak also increases and gain by parametric amplification ($V_{PD,pump\ on}/V_{PD,pump\ off}$) is increased up to approximately 9.7 which is the proof of parametric amplification. To verify the pumping power dependence of amplification, relative phase between $2f$ and f is fixed to have the maximum amplitude while measurements are done on different relative phase.

4.6 Phase dependence of parametric amplification

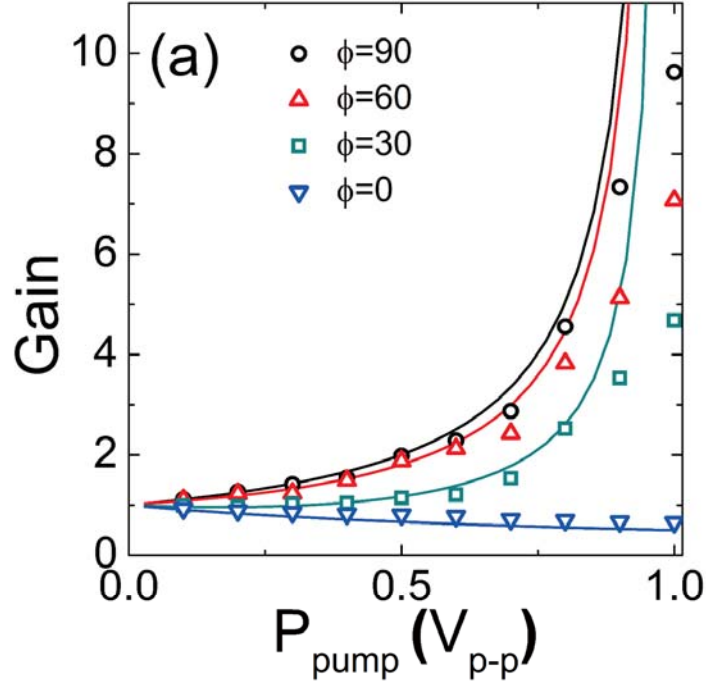


Figure 4.14: Pumping power vs amplification gain with different relative phase θ . To observe the gain dependence of parametric amplification at the different phase θ , amplitude of resonant peaks at different power is measured and height of resonant peaks are compared. At the relative phase of 0 degree, parametric deamplification is observed and gain is decreased to approximately 0.5. In case of other relative phases at 30, 60, 90 degree, gain of parametric amplification increases and we can maximum gain of approximately 9.7 at the relative phase of 90 degree and pumping power of $1.0 V_{p-p}$. Although now shown in this figure, gain is saturated at the $1.0 V_{p-p}$ with relative phase of of 90 degree and its gain is decreased slowly while pumping power is increased. To compare the theoretically expected gain with experimental result, theoretical gain (solid line) is also presented. For pumping power of $0.8 V_{p-p}$, experimental results show good agreement with theoretically calculated gain. But for pumping power bigger than $0.8 V_{p-p}$, experimental gain does not follow the theoretical result and saturated at the pumping power of $1.0 V_{p-p}$

The parametric attenuation is also measured under a phase matching condition between f_o and $2f_o$. The overall behavior of parametric gain enhancement shows good agreement with the theoretical results up to the $0.8 V_{p-p}$ pumping voltage. Above that point, the experimental gains do not follow the theoretically expected values because of nonlinear damping. [97] As shown in 4.14 shows the resonant peak under different V_p . The quality factor increases from 22,900 to 39,000 with increasing V_p from $0.1 V_{p-p}$ to $0.7 V_{p-p}$. However, as explained above, the quality factor decreases to 27,000 with a $1.0 V_{p-p}$ pumping voltage because of increasing nonlinear damping. The phase dependence of the parametric gain is maximized at the relative phase of 90 degrees as shown in Fig. 4.15. The theoretical results (solid line) shows good agreement with experimental results except for the $V_p = 1 V_{p-p}$ in which the parametric damping effect is dominant.

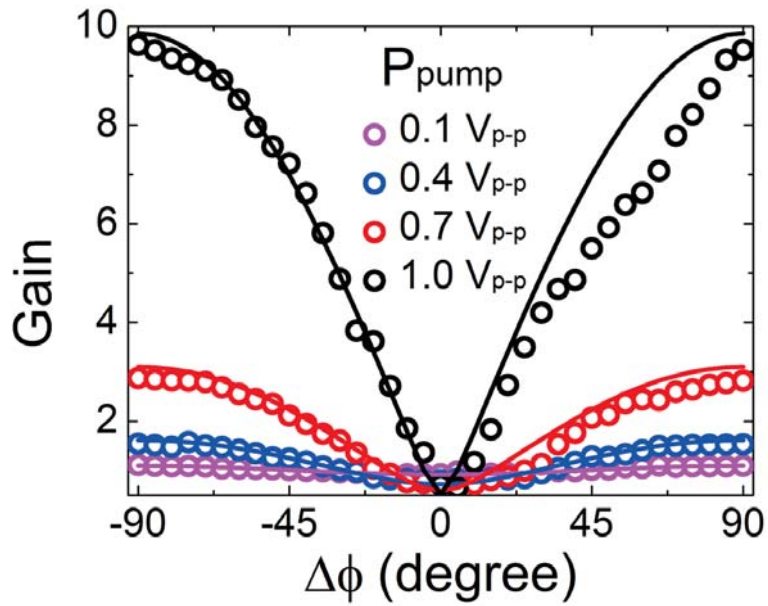


Figure 4.15: Relative phase vs amplification gain with different pumping power of $2f$ frequency. To see the full dependency of gain by parametric amplification on different relative phase, gain of parametric amplification is investigated with different relative phase at fixed pumping power from $0.1 V_{p-p}$ to $1.0 V_{p-p}$ with $0.3 V_{p-p}$ step. For pumping power of 0.1 , 0.4 , and $0.7 V_{p-p}$, phase dependency of gain by parametric amplification shows good agreement with theoretically calculated gain (solid line with same color). For parametric pumping of $1.0 V_{p-p}$, experimental result does not follow the gain increase in theoretical calculation and theoretical gain of $0.9 V_{p-p}$ (black solid line) is better fitted to the experimental result.

Chapter 5

Observation of thermal self-oscillation with optical technique

5.1 Introduction to self-oscillation¹

For resonators which can have oscillatory motions, resonators with small damping or even without damping can show oscillations whose amplitude and oscillation frequency is determined by the mechanical and geometrical factors of resonator itself. Due to small damping from environment around the resonator, there can exist oscillatory motion without variable, or periodic external excitation. Therefore, self-oscillation is different from the driven oscillation as amplitude and period of oscillation is determined by external periodic driving in driven oscillation. But it is different from the free-oscillation which do not need any external excitation with damping from environment and finally oscillatory motion of resonator decays because os-

¹This introduction to self-oscillation phenomena is based on the paper "Self-oscillation" by Alejandro Jenkins, published in *Physics Reports*

cillatory motion of resonator in self-oscillation do not depends on the initial condition.

To maintain the oscillation of resonator in undamped condition, or to make the resonator oscillate continuously, energy which comes out of the system should be compensated by the energy entering the system. Such energy compensation process occurs during the period of oscillations; however, net energy change, which is equal to the difference between energy entering the system and energy exiting the system, can fluctuate and the amplitude of the oscillations during the entire period and measurement time appears to be stable.

For self-oscillation where stable oscillation is triggered and sustained, energy exchange between the system of self-oscillatory motion and source of energy whatever type of source should be considered. If some amount of energy which is bigger than the energy loss from the system is transferred to the system, the exceeding energy is transformed to the amplitude of self-oscillation. In case of self-oscillation where amplitude of oscillation is below the stable point, the energy transfer of energy exceed the losses of energy from the system. Thus, amplitude of the oscillation increases and reaches the point of stable oscillation. On the contrary, if the energy losses from the system where amplitude exceed the amplitude of stable oscillation is greater than the energy transfer from the source of oscillation energy, oscillation amplitude decreases and amplitude reached to that of the stable oscillation. Therefore amplitude deviation from the stable self-oscillation to either direction from the stable point are subject to decay and self-oscillation become stable.

Furthermore, in some cases where amplitude deviation of self-oscillation from the stable state and a change to compensate the energy loss from the

system excite further deviations from the amplitude of stable self-oscillation, self-oscillation become unstable and system can even diverges to more unstable point. This abrupt change occur if with a decrease of amplitude, energy loss begin to exceed the energy being transferred to the system, or energy transferred to the system exceed the loss of energy from the system while the amplitude of oscillation increases; unavoidable disturbances and shocks from outside can make the self-oscillation system unstable and system itself cannot sustain its stable oscillation for any length of time.

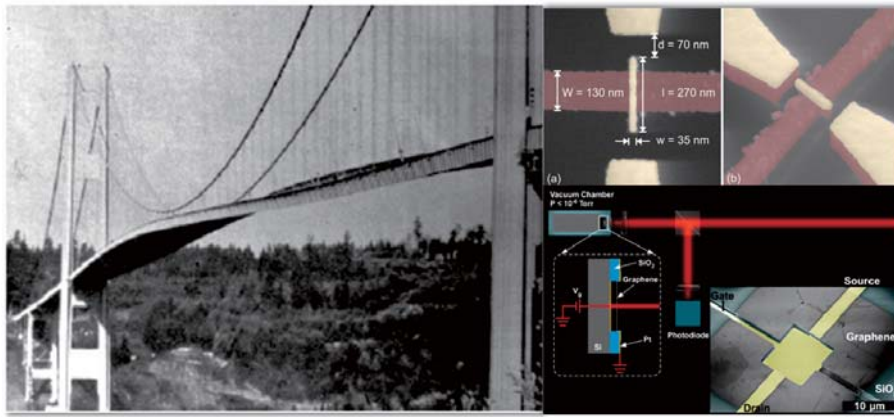


Figure 5.1: Introduction to self-oscillation

We can think of the self-oscillation of oscillator with different properties regarding the dissipation. When the energy dissipation is relatively small, or quality factor of the system is relatively high, then only small quantity of energy compared to the total energy of the system should comes to the oscillating system to sustain its self-oscillation without divergence of the stable system. The oscillation frequency and mode shape is similar to the natural frequency of the system. On the other hand, the oscillating system with higher dissipation energy, or quality factor of the system is low, energy entering the system should be large enough to sustain the oscillational motion of system. Thus the shape of self-oscillation can be different from the case

of low dissipative system. If the energy comes to the oscillating system is large enough and dissipated during a self-oscillation, it can show oscillatory motion or self-oscillation. But because of large dissipation, self-oscillations can be very different in shape from the sinusoidal oscillation and it is rather close to the relaxation oscillation, or damped oscillation.

In case of linear approximation of the equation of oscillating system, oscillation amplitude grows rapidly, or exponentially with time. In many cases, to establish the balance of energy in the system to sustain the stable state, we should account the presence of nonlinearities in the system. Thus, system can be attain the stable self-oscillation in real environment except for the case like the collapse of Tacoma Narrow Bridge which occurred in 1940.

5.2 Optical measurement of mechanical modes in thermal equilibrium

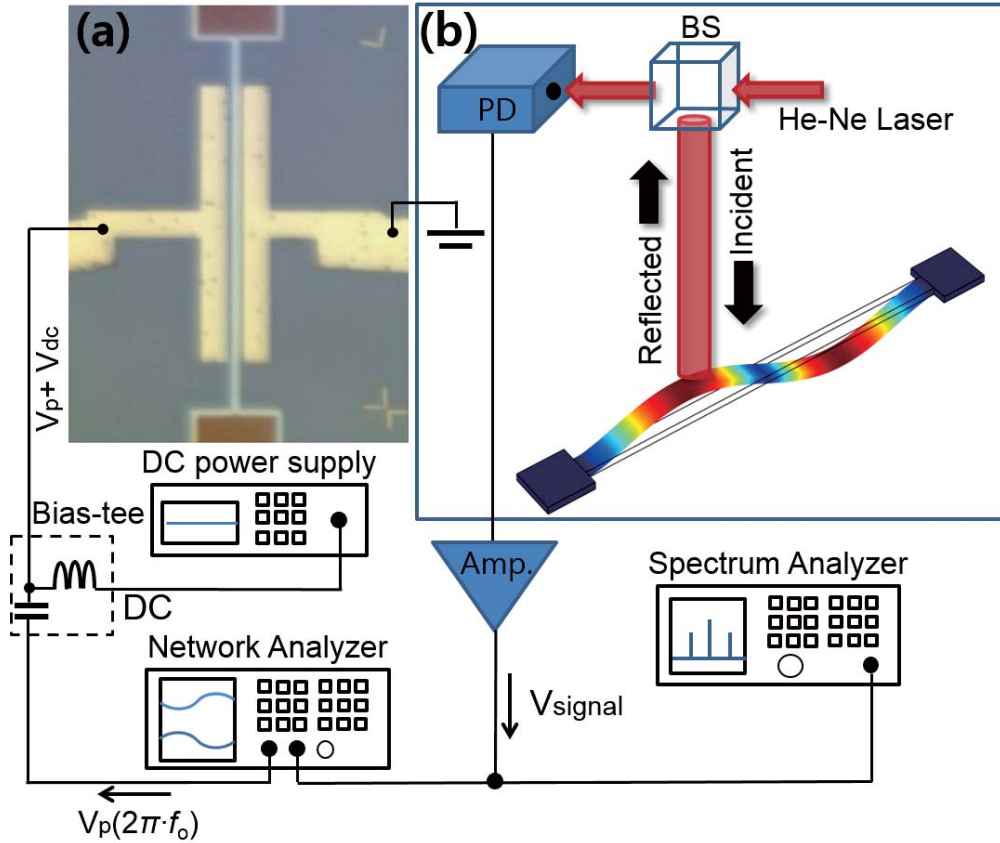


Figure 5.2: Set-up for optical measurement of thermal self-oscillation. Intensity modulated laser light which is reflected on the surface of mechanical resonator is focused onto the photo-detector(PD). To polarize the dielectric mechanical resonator, DC voltage of ± 5 V is applied between two electrodes. Small rf-signal is mixed with the DC voltage using the bias-tee. After confirming the resonant frequency of mechanical resonator by S21 measurement using network analyzer, resonant response of mechanical resonator without external excitation signal is measured using spectrum analyzer

Mechanical resonator is fabricated from high-stress silicon nitride (Si_3N_4) thin film with 200 nm thickness on a 500 nm thick silicon dioxide (SiO_2) sacrificial layer on a Si substrate. To define the movable mechanical component,

conventional e-beam lithography step and e-gun evaporation step to deposit metal are processed to define beam resonator shape and Cr mask to protect the resonator structure while following reactive ion etching (RIE) process. After RIE process to remove Si_3N_4 , Cr mask is removed with a conventional Cr etchant. To achieve desired height step between resonator and electrodes, second e-beam lithography process was done after removing SiO_2 of 300 nm thickness. Electrodes were aligned and patterned with 500 nm lateral gap from the mechanical resonator on both sides and evaporation process of dual layer Ti/Pd (10nm/50nm) was done after defining the pattern of electrode. Finally, second etching of SiO_2 sacrificial layer followed by critical point drying results the freestanding doubly-clamped beam resonator structure (80 m length, 2 m width, and 200 nm thickness) as shown in Fig. 5.2 (a)).

The response of mechanical resonator in thermal self-oscillation was detected using an optical reflectance measurement scheme combined with external RF amplifier. To confirm the resonant response by external actuation signal and the resonant frequency for multiple flexural modes, network analyzer in transmittance measurement mode (S21) was used to excite and record the resonant responses. To measure the response spectrum of mechanical in thermal self-oscillation without any external pumping, spectrum analyzer combined with external amplifier was used. Micromechanical resonator is placed in vacuum chamber under a modest vacuum (0.1 mTorr) at room temperature to prevent external damping and stimulation by air. To transfer motional state to PD, an intensity-stabilized He-Ne laser with 632.8 nm wavelength is focused on the surface of the resonator.

To verify the resonant response of mechanical resonator and resonant frequency, we first observed the driven motion to discriminate the mechanical response of the resonator from external noise like laser frequency noise. A

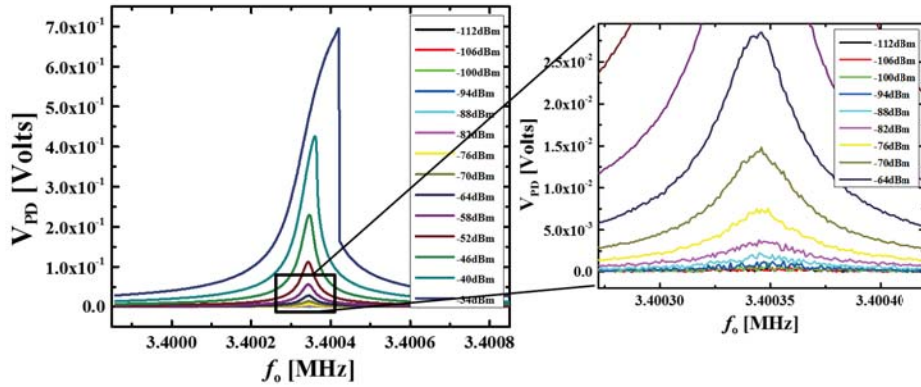


Figure 5.3: Resonant response investigation by driven oscillation. By using the network analyzer, resonant response and frequency of driven mechanical oscillation is measured. With applied rf signal ranging from -112 dBm to -34 dBm, we can observe the linear response and nonlinear response of the mechanical resonator. As the power of applied rf signal decreases, nonlinear response of mechanical resonator changes to linear response and their amplitude decreases. At the lowest power of rf signal, amplitude of resonant peak is approximately 1/100 compared to the maximum amplitude of resonant peak in the linear regime.

Vdc (10 V) between electrodes is applied and a small driving RF signal from Network Analyzer is added to excite the resonant motion. By dielectric force between electrode and mechanical resonator, micromechanical resonator oscillates along its vertical axis. To avoid nonlinear response of the resonator, driving power of applied rf-signal is limited and we applied rf power ranging from -58 dBm(0.3 mV) down to -88 dBm(4.7 V) by 6 dB steps. In the linear regime of resonant response of mechanical resonator, amplitude of the PD signal was doubled while driving power was also doubled and mechanical quality factors(Q) were measured to be 56,000 with 5 % variation at each driving rf power as shown in Fig. 5.3. By decreasing the amplitude of applied rf signal, we can approach the motional state of the mechanical resonator at thermal equilibrium.

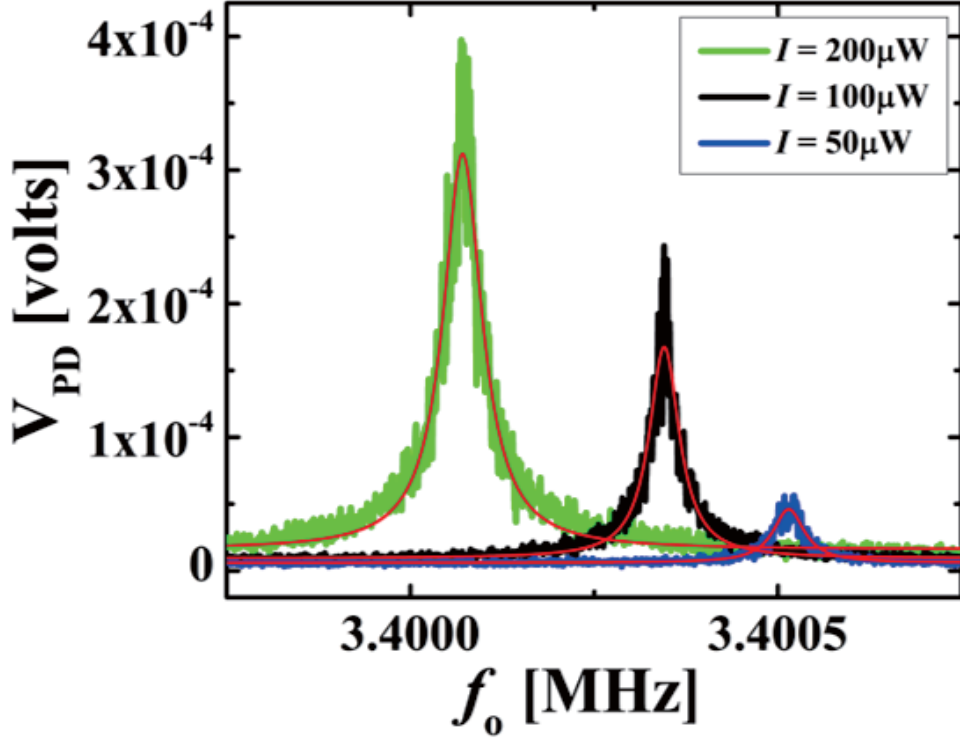


Figure 5.4: Resonant frequency vs probing laser power

By increasing the intensity of probing He-Ne laser, we observe the increase of signal amplitude at resonance, while Q and resonant frequency of thermal motion decreases due to thermal dissipation by increased laser power. Spectrum analyzer with external voltage amplifier (55 dB) is used to detect fundamental and higher-mode thermal self-oscillations and its power spectral density is recorded as shown in Fig. 5.4. To verify whether any unintended electrical polarization of the mechanical resonator itself is a possible energy source for the self-oscillation, we also measured a normalized resonant response with varying DC bias. Along with a constant Q values without significant variation, we found the stable amplitude of thermal oscillation under various DC bias and we could not find any proof for DC bias dependent oscillation. [98] [99]

For the fundamental mode of doubly-clamped mechanical resonator with internal mechanical stress, resonant frequency is expressed as follows

$$f_0 = 1.03 \left(\frac{t}{l^2} \right) \sqrt{\frac{E}{\rho}} \sqrt{1 + \frac{\sigma_{int} l^2}{3.4 E t^2}} \quad (5.1)$$

where l is length of resonator, E is Young's modulus, ρ_{int} is internal stress, t is thickness, and ρ is density of Si_3N_4 . With known physical parameters for high-stress Si_3N_4 ($E=320$ GPa, $\sigma_{int} = 800$ MPa, $\rho = 3.2$ g/cm³) and dimensions of mechanical resonator ($l = 80$ μm , $t = 200$ nm), estimated frequency of the 1st oscillation mode of our mechanical resonator is approximately 3.506 MHz. From our measurement of mechanical resonators of some resonators with same dimensions, resonant frequency was around 3.5 MHz with variation of approximately 100 kHz for numerous resonators. By using FEA (Finite Element Analysis) tool (COMSOL 4.3b and previous versions), resonant frequency of mechanical resonator with physical parameters mentioned above was 3.54 MHz. Both FEA and experimental measurement showed good agreement with theoretical calculation.

To investigate the resonant motion of mechanical resonator which is composed of multiple oscillatory mode, we measured the resonant frequency of the mechanical resonator from fundamental to higher modes. To clarify their oscillatory motion from the electrical and optical noise, we also used the S21 measurement by network analyzer for investigation of driven oscillation at each mode. At each mode measured using network analyzer, each mechanical mode were tested by spectrum analyzer combined with external amplifier. To remove external excitation except thermal excitation, vacuum chamber and electrical lines were grounded. Only DC bias voltage was applied to the sample to stabilize the resonant frequency. Among many mechanical resonators

tested, we show most representative results of same mechanical resonator with probing laser of $200 \mu\text{W}$ power.

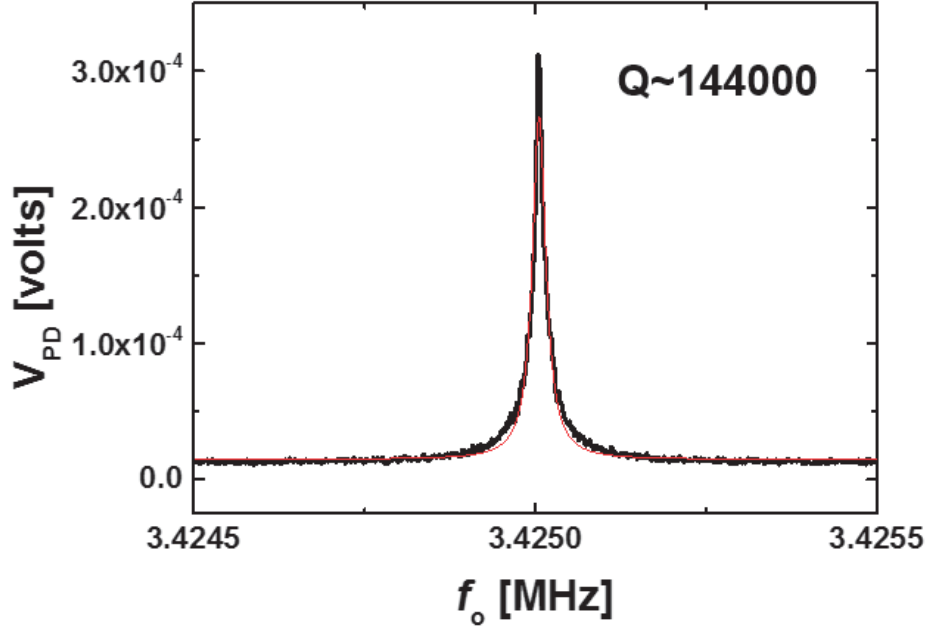


Figure 5.5: Resonant frequency of 1st mode thermal self-oscillation. Resonant frequency and their spectral response is measured using spectrum analyzer with optical set-up. Resonant frequency is measured to be approximately 3.425 MHz. Q is about 144,000 and dissipation rate γ is 23.8 Hz. Laser spot is focused on the center of mechanical resonator to acquire maximum amplitude of resonant spectrum

For fundamental mode of thermal self-oscillation, we can observe the fundamental resonant mode of mechanical resonator of $80 \mu\text{m}$ length. Resonant frequency is approximately 3.4250 MHz and mechanical quality factor Q is approximately 144,000 by Lorentzian fitting of resonant peak (Fig. 5.5). For fundamental mode of mechanical resonator, amplitude of resonant peak was sufficiently high and we could observe the peak even without external amplifier.

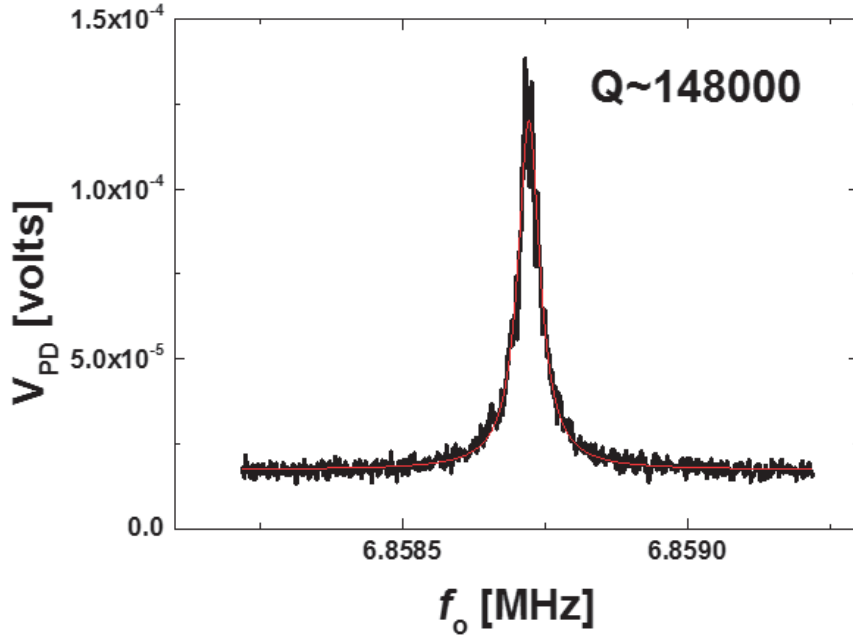


Figure 5.6: Resonant frequency of 2nd mode frequency thermal self-oscillation. Resonant spectrum and their frequency is measured using spectrum analyzer and optical set-up. To get maximum amplitude of spectral response, laser beam is focused on the position of one quarter along the longitudinal axis of mechanical resonator from one clamping point. Their resonant frequency is approximately 6.8587 MHz. Q and dissipation rate γ is 148,000 and 46.3 Hz, respectively.

To observe the second mode of thermal self-oscillation, we move the position of focal point of laser on the mechanical resonator to $20 \mu\text{m}$ distant from one clamp. In case of measurement done at the center of mechanical resonator, we could only observe small amplitude of resonance due to small displacement of mechanical resonator at nodal point. At the position for measurement of 2nd mode, we could observe maximum amplitude of 2nd resonant mode. Resonant frequency is approximately 6.8587 MHz and mechanical quality factor Q is approximately 148,000 by Lorentzian fitting (Fig.

5.6). Amplitude of 2nd mode compared to fundamental mode is smaller than one half of that of fundamental mode.

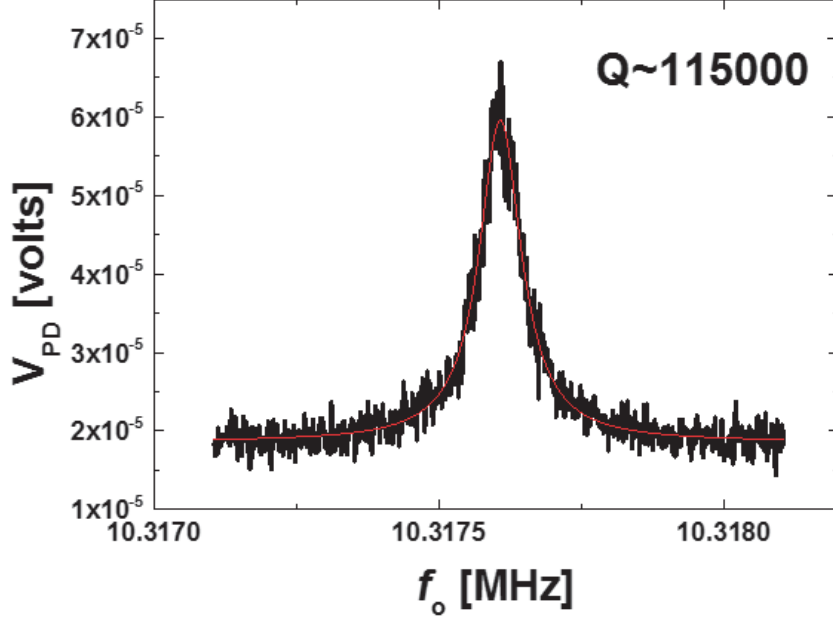


Figure 5.7: Resonant frequency of 3rd mode thermal self-oscillation. Resonant spectrum and their frequency is measured using spectrum analyzer and optical set-up. To get maximum amplitude of spectral response, laser beam is focused at the center of mechanical resonator along the longitudinal axis from one clamping point. Their resonant frequency is approximately 10.3176 MHz. Mechanical quality factor Q and dissipation rate γ is 115,000 and 89.7 Hz, respectively.

For observation of 3rd mode of thermal self-oscillation, we move the position of focal point of laser on the mechanical resonator to the center of the mechanical resonator. At the position for measurement of 3rd mode, Resonant frequency is approximately 10.3176 MHz and mechanical quality factor Q is approximately 115,000 by Lorentzian fitting (Fig. 5.7).

We moved the position of focal point of laser on the mechanical resonator to 10 μm distant from one clamp to get maximum amplitude of resonant

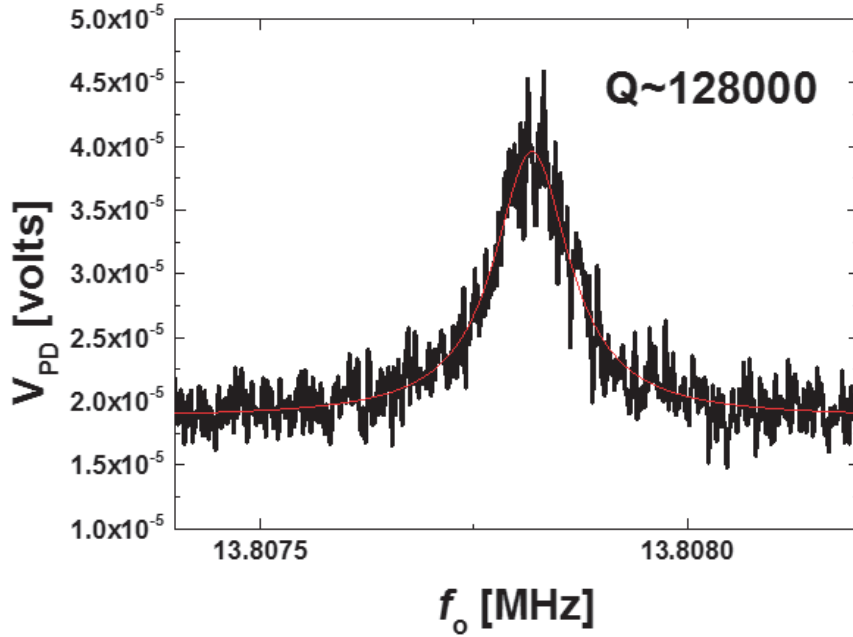


Figure 5.8: Resonant frequency of 4th mode thermal self-oscillation. Resonant spectrum and their frequency is measured using spectrum analyzer and optical set-up. Laser beam is focused on the resonator 10 micron distant from the one clamping point along the longitudinal axis. Their resonant frequency is approximately 13.8078 MHz. Mechanical quality factor Q and dissipation rate γ is 128,000 and 107.8 Hz, respectively.

peak at the anti-node. We could measure the resonant peak of 4th mode approximately 13.8078 MHz and mechanical quality factor Q is approximately 128,000 by Lorentzian fitting (Fig. 5.8). Because of the small amplitude of 4th mode of thermal self-oscillation, we combined external voltage amplifier (Miteq Co.) with spectrum analyzer and multiple of dc block and low-pass filter were used to suppress the external noise power.

To observe the resonant peak of 5th mode, we moved the position of focal point of laser on the mechanical resonator to the center of mechanical resonator along the longitudinal axis which is the nodal point of 5th oscillation. We measured the resonant peak of 5th mode approximately 17.3447 MHz

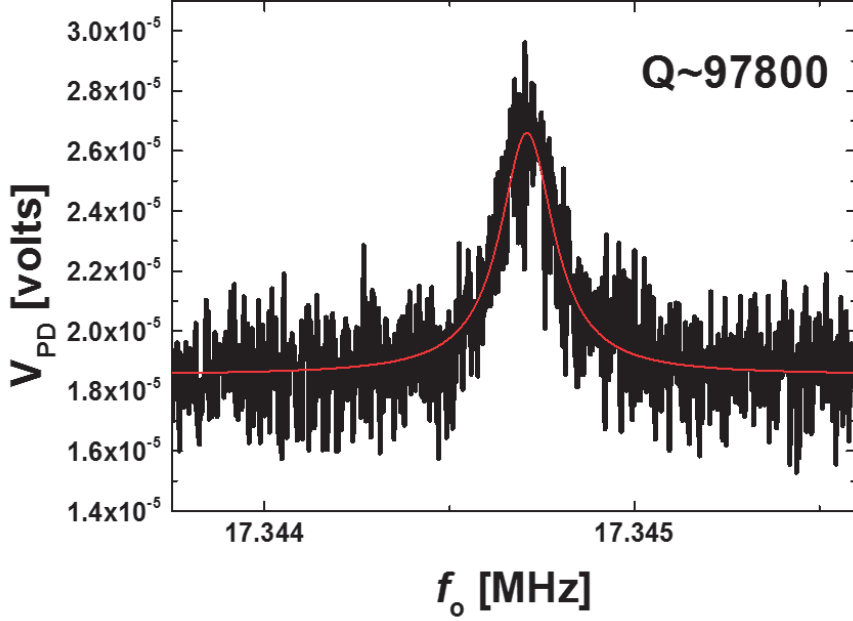


Figure 5.9: Resonant frequency of 5th mode thermal self-oscillation. Resonant spectrum and their frequency is measured using spectrum analyzer and optical set-up. Laser beam is focused at the center of along the longitudinal axis. Their resonant frequency is approximately 17.3447 MHz. Mechanical quality factor Q and dissipation rate γ is 97,800 and 177.3 Hz, respectively.

and mechanical quality factor Q is approximately 97,800 by Lorentzian fitting (Fig. 5.9). To measure the 5th mode, we also used the external voltage amplifier, dc block, and low-pass filter.

To measure the possible effect of probing laser, we measured the resonant response of 1st mode of mechanical resonator with different power of probing He-Ne laser ($\lambda = 632.8$ nm). In case of mechanical resonator with small cross-sectional area, heat induced by incident light cannot dissipate to clamping area sufficiently. This thermal effect by incident laser beam can affect the resonant motion of mechanical resonator in the form of decrease of mechanical quality factor Q , or increased dissipation rate γ , and decrease of resonant frequency by relaxation of internal stress by thermal expansion

from temperature change. At different power of incident laser on mechanical resonator using O.D (Optical Density) filter, we could observe the increase of both resonant frequency of fundamental mode and mechanical quality factor (Q) Fig. 5.10. At the strongest optical power of incident laser (Upper left, $100 \mu\text{W}$), resonant frequency was measured to be approximately 3.50992 MHz with quality factor of $144,000$. By reducing the laser power with OD (Optical Density) filter to $40 \mu\text{W}$ (upper right), resonant frequency rose to 3.50995 MHz and quality factor also increased to $160,000$. With probing laser of $18 \mu\text{W}$ power(lower left), resonant frequency was measured to be 3.50996 MHz and quality factor was $218,000$. At the power of probing laser at $10 \mu\text{W}$ (lower right), measured resonant frequency is approximately 3.50996 MHz , almost same as the case of probing laser power of $18 \mu\text{W}$, but quality factor decreased to $190,000$. To investigate the stable thermal self-oscillation, we waited for some time until the resonant frequency was stabilized at thermal equilibrium. From the experiment with different probing laser power, we could verify that thermal dissipation and relaxation affected the self-oscillation of mechanical oscillator and those effects did not affect further on the resonant spectrum of mechanical resonator under certain power of probing laser.

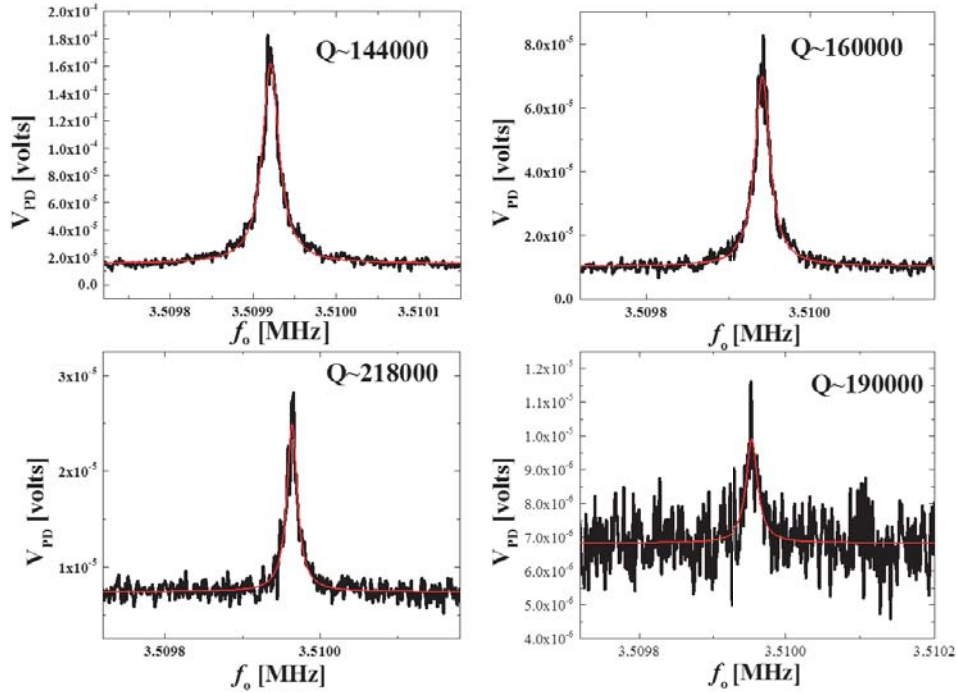


Figure 5.10: Q -factor and mechanical resonant frequency dependence on the power of probing laser on mechanical resonator. Resonant frequency and mechanical quality factor is affected by the power of probing laser due to thermal dissipation and stress relief by heat from incident light of laser. By decreasing the power of incident laser on mechanical resonator using optical filter, we can observe the increase of both resonant frequency of fundamental mode and mechanical quality factor (Q). With the highest optical power of probing laser (Upper left, $100 \mu\text{W}$), resonant frequency is measured to be 3.50992 MHz with quality factor of 144,000. By reducing the laser power with OD (Optical Density) filter to $40 \mu\text{W}$, resonant frequency rise to 3.50995 MHz and quality factor increases to 160,000. With the power of probing laser of $18 \mu\text{W}$, resonant frequency is measured to be 3.50996 MHz and quality factor become 218,000. With the probing laser of $10 \mu\text{W}$, measured resonant frequency is approximately 3.50996 MHz, same as the case of probing laser power of $18 \mu\text{W}$, but quality factor decreases to 190,000.

5.3 Construction of power-spectral image of thermal self-oscillation

Recently, capacitive measurement and optical measurement technique could resolve the resonant frequencies of flexural motion at low temperature and its phonon ground state. But mode shape and other information related higher modes could not be collected due to their limitation in measurement technique which requires the summing segmented capacitance or optical reflectance over the surface length of the mechanical resonator. Thus there were many attempts to reveal the mode shape of mechanical resonator in driven motion and thermal oscillation.

Measurement techniques based on high-finesse optical cavity [100] [4] or optical reflectance also have been successful in observing thermal motion of micro-mirror at the one end of a Fabry-Perot cavity. Although optical measurement based on high-finesse optical cavity presents very sensitive detection of thermal motion, it needs high-reflective coating on the resonator or the resonator itself should consist of materials with large optical reflectance to observe such a small motion. Thus, high-finesse cavity is not easily compatible with mechanical resonator for applications requiring both high-frequencies and high mechanical Q . Other optical techniques based on AFM technique, [101] synchronous imaging, [102] and beam deflection microscopy, [103] Recently, scanning probe microscope and optical reflectance measurement could map the driven motion of mechanical resonators based on carbon nanotubes [104] and graphene. [105] But, interaction between the scanning tip and the surface of oscillating structure suppresses its thermal motion, thus, mapping of thermal motion could not be attained.

With measurement of fundamental and higher mode of mechanical resonator in thermal self-oscillation, we reconstructed the mode shape of each vibrational mode by mapping the power spectral density on the surface of mechanical resonator in thermal self-oscillation. We measured the spectral density by thermal self-oscillation of mechanical resonator with spectrum analyzer, optical set-up, and external amplifier on the surface of mechanical resonator along the longitudinal axis with 500 nm step. To investigate the multiple vibrational modes which are superposed in the optical measurement at one point on the mechanical resonator, we measured the power spectral density around the resonant frequency at each point. After measurement of power spectral density of each mechanical modes on different position, measured power spectral densities were composed to their mode number along the longitudinal axis of mechanical resonator. Composed power spectrum reflected the mode shape of each mechanical mode.

During scanning noise power spectrum of thermal self-oscillation along the longitudinal axis of the resonator, resonant frequency of fundamental mode changes by 300 Hz (~ 5 times of FWHM) between clamp and the center of mechanical resonator. This change is attributed to relaxation of tensile stress by thermal expansion from heating effects due to the probing laser (100 μW). From the frequency dependency on internal tensile stress, we estimate that the temperature change $\Delta T = 4(\delta f/f)(\sigma/E)(1/\alpha)$ was about 0.4 K from the theoretical calculation, with thermal expansion coefficient $\alpha \sim 3.2 \times 10^{-6}$ for high-stress silicon nitride. [] Thus we can expect that temperature difference along the mechanical resonator does not change the resonant motion of mechanical resonator significantly. Frequency differences of resonant peaks of thermal oscillation at different positions are fitted to same frequency f_0 to compare the amplitude of thermal self-oscillation.

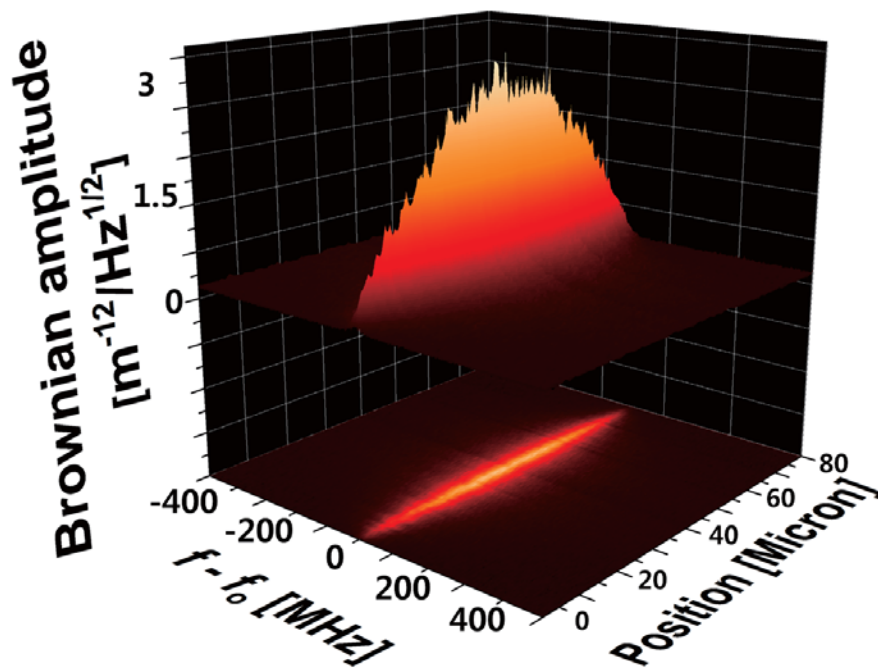


Figure 5.11: Mode image of 1st mode thermal self-oscillation. At clamp, amplitude of resonant amplitude is minimum and we can observe the maximum amplitude of resonant peak at the center of mechanical resonator. In this case, center of mechanical resonator is anti-node and nodal point only exist at the clamps

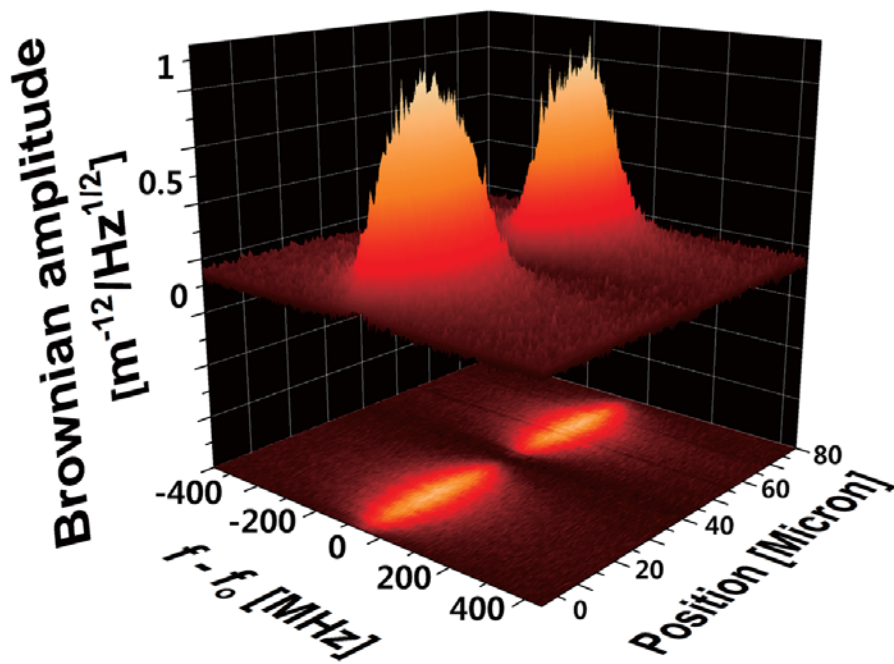


Figure 5.12: Mode image of 2nd mode thermal self-oscillation. We can observe the mode shape of 2nd vibrational mode with one nodal point at the center of mechanical resonator.

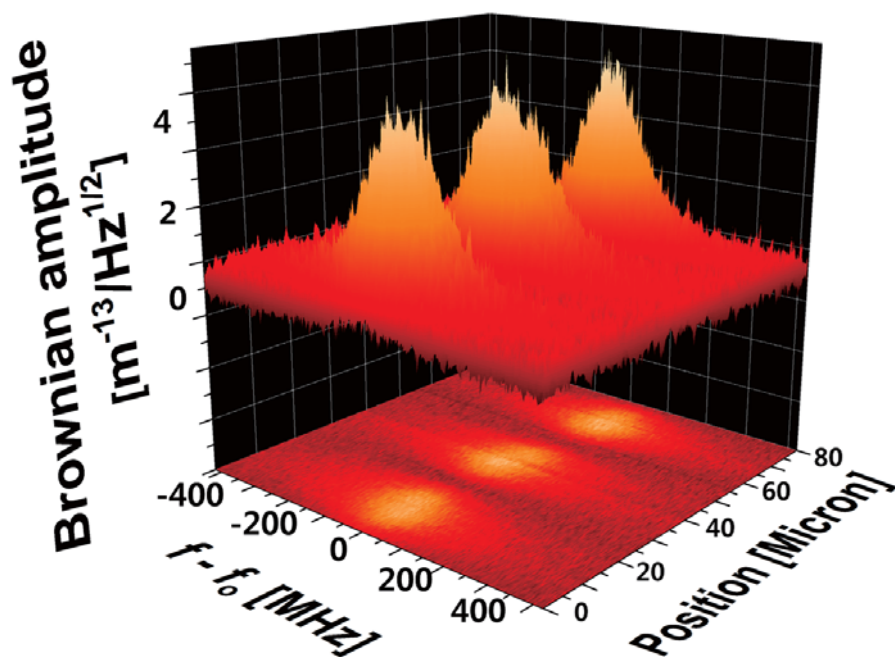


Figure 5.13: Mode image of 3rd mode thermal self-oscillation. We can observe the mode shape of 3rd vibrational mode with two nodal point along the mechanical resonator except clamping point and three anti-nodal points.

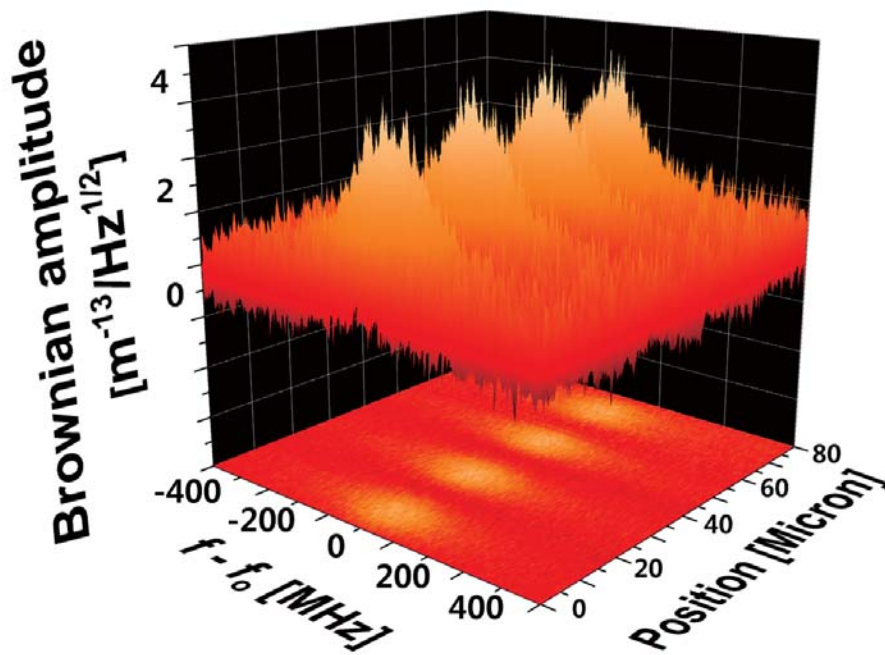


Figure 5.14: Mode image of 4th mode thermal self-oscillation. We can observe the mode shape of 4th vibrational mode with three nodal points along the mechanical resonator's longitudinal axis except the clamping point and 4 anti-nodal points.

5.4 Investigation of relative displacement of thermal modes in mechanical oscillator driven by Langevin force

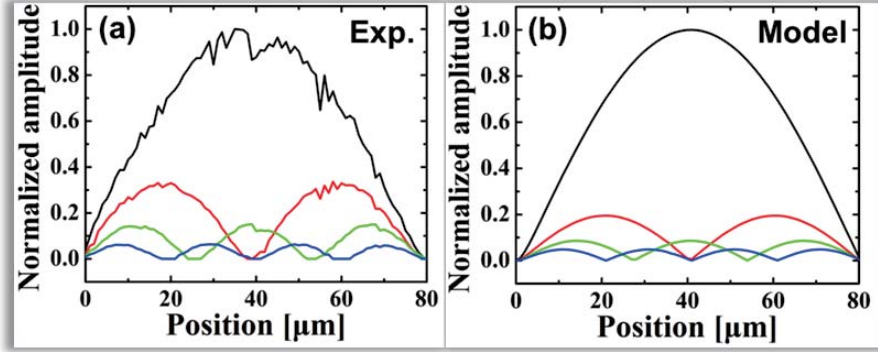


Figure 5.15: Comparison of relative displacement of thermal self-oscillation by experiment (a) vs theory (b). Relative displacement by experimental results are attained from the lorentzian fitting of each power spectral density. Their peak height corresponds to the relative displacement. Compared with the relative displacement of driven oscillation, peak amplitude of resonant spectrum are used to compare the relative displacement at different position in the same mechanical mode.

To verify the optical technique of displacement spectral density as a displacement measurement tool, we compared the mode shape and relative displacement of mechanical resonator of different vibrational mode of thermal self-oscillation at the same position on the mechanical resonator. [107] The displacement of mechanical resonator, z , at the position x can be given as follows.

$$\rho A \frac{\partial^2 z}{\partial t^2} + EI \frac{\partial^4 z}{\partial x^4} - T \frac{\partial^2 z}{\partial x^2} = 0 \quad (5.2)$$

where ρ is density of high-stress silicon nitride, A is cross sectional area, E is Young's modulus, I is moment of inertia of resonator along the ver-

tical axis, and T is tensile load at the clamp of mechanical resonator. For micromechanical resonator driven only by thermal energy or Langevin force, different from the driven oscillation, displacement of mechanical resonator at specific point on the mechanical resonator is the sum of displacement of superposed every resonant modes at the measured point and is given by

$$z_{max} = \sum_{n=1} \alpha_n z_n \exp(-i\omega_{driving}t) \quad (5.3)$$

where z_n is the n -th solution of resonant mode of the mechanical resonator from equation 5.2 and each solution has the form as follows.

$$z_n = \cos\left(\frac{A_n x}{L}\right) - \cosh\left(\frac{A_n x}{L}\right) - \frac{A_n}{B_n} \sin\left(\frac{B_n x}{L}\right) - \sinh\left(\frac{B_n x}{L}\right) \quad (5.4)$$

where $A_n = 57.8578, 78.955, 79.2692, 79.699$ and $B_n = 3.18361, 6.35177, 9.48989, 12.585$ for first 4 modes are numerically calculated by physical parameters of the mechanical resonator. By using the Zener's model, we can have the relative ratio of α_n between different mechanical modes,

$$\frac{\alpha_n}{\alpha_{n'}} \approx \frac{f_{n'}^2}{f_n^2} \cdot \frac{c_n}{c_{n'}} \quad (5.5)$$

where $c_n = 8.88925, 7.81494, 5.32446, 4.07732$ for four n -th mode ($n=1, 2, 3, 4$) are conversion factors to compare the relative displacement among different n -th mechanical mode at thermal equilibrium. With numerically calculated relative ratio and amplitude of each resonant mode, relative displacement amplitude among resonant modes can be compared. Theoretically calculated relative displacement of each resonant mode is scaled to fit the maximum amplitude of fundamental mode as 1 (Fig 5.15 (b)). Relative displacement by experimental results are from the lorentzian fitting

of each power spectral density and their peak height are scaled to compare relative displacement. Only in case of 2nd mode, experimentally attained displacement amplitude shows approximately 50 % higher value compared to theoretically expected amplitude and other modes show consistency between experimental data and theoretical calculation of relative amplitude. In thermal self-oscillation, different from oscillations driven by harmonic force, relative displacement amplitude of higher modes decreases rapidly according to increased resonant frequency, which is expected for mechanical resonators driven by thermal noise.

Chapter 6

Mode-splitting of thermal oscillatory mode in micromechanical resonator by mechanical sideband

Recently, photonic cavity with optical and microwave frequency coupled to micro-and nano-mechanical system become important tool to control and manipulate the motion of mechanical resonator and led to the realization of single phonon quanta. In these systems, photonic mode with high-quality-factor is coupled to other system. For optomechanical system which combine photons with phonons in mechanical devices or resonators, optical cavities with high-Q are coupled with the mechanical resonator's mode parametrically. This technique cannot avoid challenges like realizing nanostructure with both good optical properties and mechanical properties. To overcome these obstacles, there have been many approaches. In Caltech group, photonic-phononic crystal cavity where waveguide and photonic crystal cavity was realized in

a mechanical resonator which has breathing mode of GHz and coupling between photonic and phononic mode enabled the cooling of mechanical resonator by optical cooling. By NTT group in Japan, mechanical cavity which use one oscillation mode of the mechanical resonator was realized and interaction between mechanical mode and mechanical phonon-cavity was investigated. In contrast to a photonic cavity, phonon cavity can be operated in the resolved sideband regime by its narrow linewidth and it can host dynamical backaction onto the mechanical element.

In mechanical phonon-cavity presented by NTT group, piezoelectric pump generate strain-induced parametric coupling between the first and the second mode at a rate of that can exceed intrinsic damping rate. In that case, mechanically induced transparency in the second mode which plays the role of phonon cavity, the emergence of parametric normal-mode splitting and the ability to transfer mechanical energy to the second mode.

To control the parametric coupling between mechanical modes, we realized the doubly clamped mechanical resonator with high mechanical quality factor at room temperature and their fundamental and second mode. mechanical resonator is driven by electrical field gradient force and mechanical modes are coupled by mechanical sideband of fundamental and second flexural mode.

6.1 Micromechanical resonator as a signal mixer and mechanical sideband

In radio communications and RF engineering, sideband is a band of frequencies higher or lower than the carrier frequency, which contains power as a result of the modulation process. For frequency multiplier, frequency multiplier also mixes input frequencies (f_1, f_2, \dots) but their output only carries the sum of input frequencies. In case of frequency mixer, signal mixer mixes two, or multiple frequencies into input port and output sum and difference of input frequencies including harmonics which are not used or suppressed in multiplier.

As a nonlinear device or component for electrical signal control and processing, mechanical resonator can also act as a nonlinear device for mechanical signal processing to generate sum and difference frequency of input frequencies and their harmonics. Mechanical resonator driven at certain resonant mode can show mode interaction between different mechanical modes and their sidebands can be investigated.

For strongly driven mechanical resonator at one resonant mode of same device, mechanical resonator shows its spectral responses at the frequencies where sum (ex, $f_1 + f_2$) and difference (ex, $f_2 - f_1$) among their resonant frequencies(ex, $f_1, f_2, f_3 \dots$).

Instead of driving mechanical resonant mode to excite mechanical sideband which is screened or not observable by the electrical noise in normal operation, we can use the mechanical sideband to excite the mechanical mode of thermal oscillation. In case of thermal oscillation, we do not need actuate the mechanical resonator which is in oscillatory motion by thermal energy from environment. By applying rf signal at the frequency of red-detuned

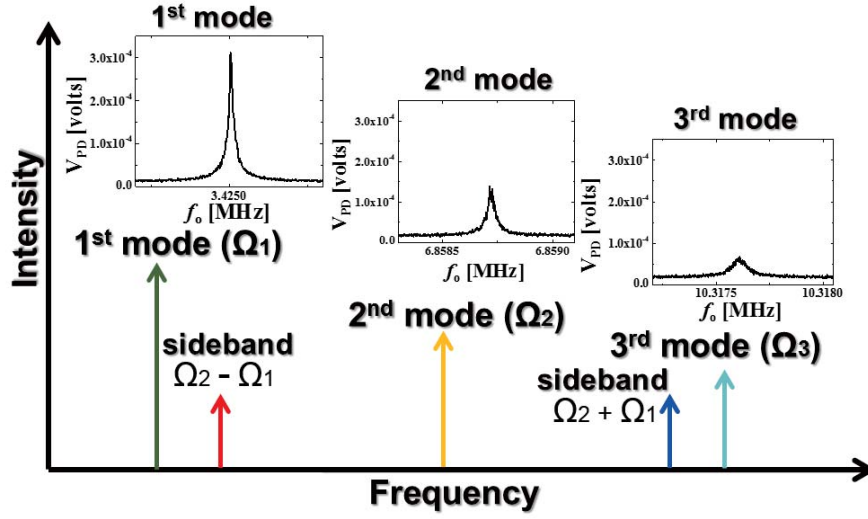


Figure 6.1: Mechanical sideband by thermal self-oscillation. For doubly-clamped mechanical resonator from high-stress Si_3N_4 , we can observe multiple resonant spectrums by thermal self-oscillation. Using these resonant spectrums, we can expect multiple sidebands by thermal modes. As mechanical resonators are not directly driven at resonant modes, we cannot observe sidebands by thermal modes. But we can expect virtual sidebands between mechanical modes. In this case, we set 2nd resonant spectral mode as a base band or carrier band. By interaction between 1st and 2nd mode, we can expect the red-detuned (f_r

sideband which is defined as difference frequency ($f_2 - f_1$) and blue-detuned(f_b) sideband which is defined as sum frequency ($f_2 + f_1$).

sideband ($f_2 - f_1$) and blue-detuned sideband ($f_1 + f_2$) their energy can be transferred to mechanical modes(blue-detuned sideband) and help to transfer energy in one band to the other band.(red-detuned sideband)

For mechanical resonator of our experiment to control its mechanical modes with mechaical sideband, first, motional states of thermal self-oscillation are investigated using optical measurement technique. Before sideband actuation, fundamental mechanical mode of resonator is measured at approximately 3.42 MHz. Their second mode (6.8587 MHz) and third mode (10.3176 MHz) were also observed by same technique and their resonant frequency is in good agreement with theoretical expectation that n-th

resonant frequency has the n -integer times the frequency of fundamental mode.

6.2 Control of mechanical system by side-band scheme

In laser cooling for atoms, ions, molecules, the lowest temperature that can be attained for a trapped atom optical decay rate κ is given by $T_D \simeq \hbar\kappa/4k_B$, the doppler temperature. If the harmonic trapping frequency Ω_m is smaller than κ , the minimum average occupation number $\langle n \rangle$ in the harmonic trapping potential is $\langle n \rangle \approx \kappa/4\Omega_m > 1$, that is, the ion's harmonic motion cannot be cooled down to the quantum ground state. In this case, the fundamental temperature limit can also be interpreted as the backaction of photon to ion or atoms. Due to the discrete and stochastic nature of photons, scattering occurs randomly in the time scale and thus, radiation-pressure force induces heating of ion and atom in the cooling process to ground-state cooling

But it was proved that the ground-state cooling can be possible in the resolved-sideband regime. [108] [109] [110] The physical mechanism of resolved-sideband cooling can be understood as follows in simple ways. Owing to their harmonic motion of atom or ion, a spatially oscillating excited particle emit phase-modulated radiation. Consequently, the emission spectrum consists of a series of sidebands at frequencies $\omega_0 - j\Omega_m$ where $j = \pm 1, \pm 2, \dots$ and ω_0 is the unperturbed transition frequency. Inversely, the absorption spectrum as probed by an observer in the laboratory frame will consist of a series of absorption lines, broadened owing to the upper state's decay rate. If we tune the incident laser radiation to one of the energetically lower-lying sidebands, $\omega_L = \omega_0 - \Omega_m$, then the particle absorbs photon of $\hbar\omega_L = \hbar(\omega_0 - \Omega_m)$ whereas it emits photon of energy $\hbar\omega_0$. Series of this process can entails a reduction of particle's translational energy by one quantum, enabling cooling to quantum ground state.

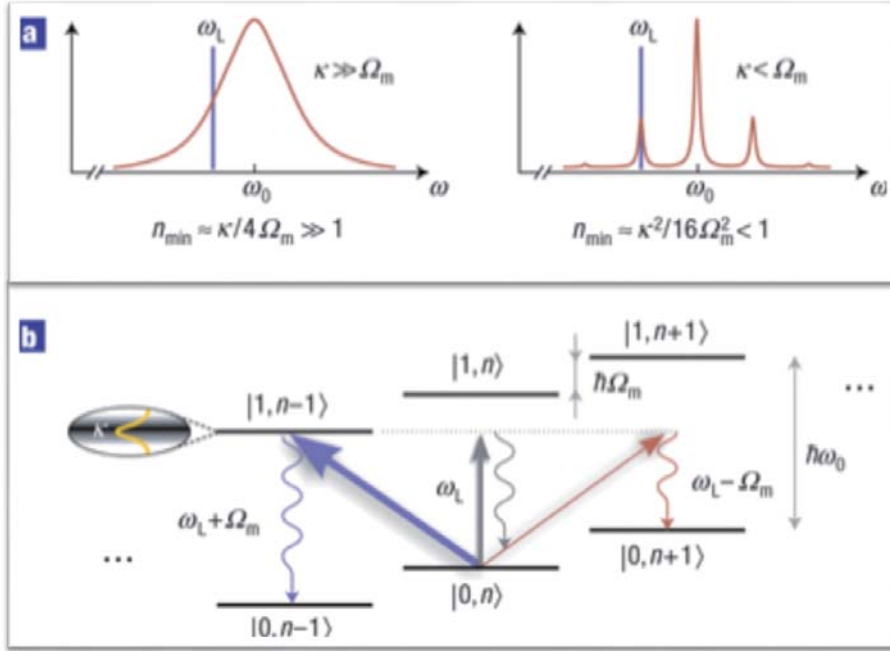


Figure 6.2: Control of mechanical resonator by optical sideband. In the resolved sideband regime, mechanical resonator's oscillation makes red-detuned and blue-detuned sideband next to the optical cavity resonant spectrum and their separation is the resonant frequency of mechanical oscillator (upper). When the optical photon at the frequency of red-detuned sideband meets the system of mechanical resonator and optical cavity ($|0, n\rangle$), energy of photon absorbs the energy of mechanical resonator by one phonon and its energy state is $|1, n - 1\rangle$, and photon energy is dissipated by spontaneous emission from the cavity. Thus energy of mechanical resonator (phonon) decreases. With blue-detuned sideband, system's state changes to $|1, n + 1\rangle$. By spontaneous or stimulated emission, photon exit the system and final state is $|0, n + 1\rangle$. Thus mechanical resonator absorbs energy from the photon and mechanical resonator is amplified. Figures are from *Nature Phys.* 4. 415(2008) by A. Schliesser.

Many of these concepts in atomic laser cooling can be applied to control the mechanical resonator and optomechanics, which study the dynamics of a mechanical resonator parametrically coupled to an electrically or optically resonant device. [112] [113] [114] [115] [8] Due to the dynamical back-action of the electrical or optical field on the mechanical oscillator in the form of a

Coulomb or radiation-pressure force, mechanical device of 10 MHz resonant frequency could be successfully cooled down to the mechanical ground state.

For control of mechanical resonator with phonon cavity and coupling of mechanical modes via mechanical sideband, mechanical cavity's decay rate κ should be smaller than the difference of resonant frequency and applied sideband frequency to avoid interference by resonant frequency of second or phonon cavity. In our mechanical resonator, there is a gap of 10 kHz in frequency domain between fundamental mechanical mode and red-detuned sideband frequency ($f_2 - f_1$), which is 200 times the FWHM of fundamental mode. Thus we can reduce the unwanted excitation of mechanical mode by mechanical sideband.

In photonic or optical cavity in optomechanical system, mechanical motion induces sidebands in optical spectrum and mechanical sideband should be separated from the optical resonant spectrum to avoid the absorption of energy from cavity.

6.3 Mode-splitting of 1st mode by red-detuned mechanical sideband

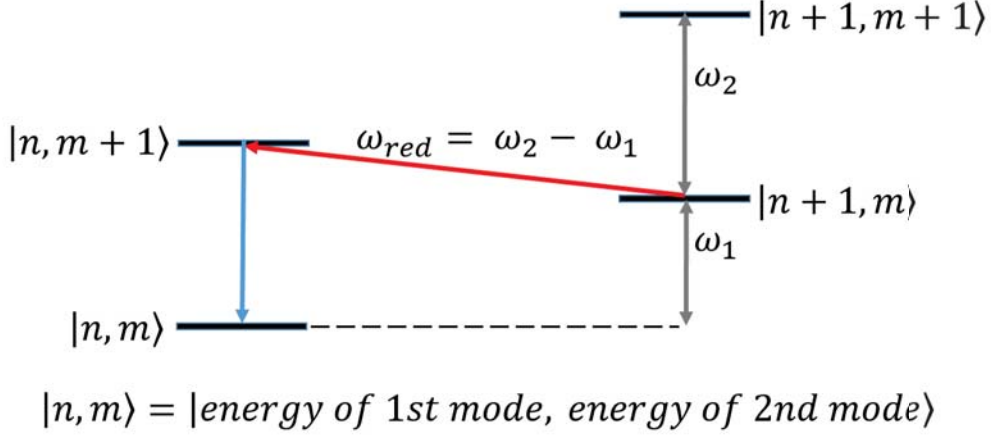


Figure 6.3: Control of mechanical resonator by red-detuned mechanical sideband. In the resolved sideband regime, mechanical resonator's oscillation (1st mode) makes red-detuned sideband next to the resonant spectrum of phonon cavity (2nd mode) resonant spectrum and their separation is the resonant frequency of mechanical oscillator. When the pumping rf-signal at the frequency of red-detuned sideband meets the system of mechanical resonator and phonon cavity, resonator at the state $|n+1, m\rangle$ absorbs energy from the red-detuned sideband and their state is shifted to $|n+1, m\rangle$ by transferring energy of 1st mode to 2nd mode via applied red-detuned sideband. As 1st mode of mechanical oscillation loses its energy and 2nd mode absorbs energy from red-detuned sideband pumping, 1st mode is cooled and 2nd mode is heated. If 2nd mode loses energy by some dissipation channel, then mechanical resonator loses its energy and cooled down from $|n+1, m\rangle$ state to $|n, m\rangle$ state. To transfer the mechanical energy of 1st mode to 2nd mode via red-detuned sideband, 1st mode is coupled to red-detuned sideband and we can observe mode-splitting in the response spectrum. 2nd mode is also coupled to red-detuned sideband and we can also observe the mode-splitting in the response spectrum of 2nd mode.

In case of mechanical resonator without external optical or electrical cavity, motional states of mechanical resonator can be used as a cavity. After control of motional state in mechanical resonator by sideband was demonstrated, [117] [118] there was a report to control the resonant motion of me-

chanical resonator by mechanical sideband as a phonon-cavity electromechanics, [39] and phonon lasing. [119] By applying red-detuned or blue-detuned sideband of a mechanical resonator with phonon-cavity (phonon cavity is designated to one mechanical resonant mode and sidebands are generated by interaction between phonon-cavity and other resonant band), normal modes or resonant modes, which do not interact in ordinary motional state can be coupled.

To investigate the response of mechanical resonator by applied the red-detuned sideband of 1st (f_1) and 2nd (f_2) oscillation mode of mechanical resonator, we should be able to control and observe the resonant motion of 1st and 2nd mode during the measurement of spectrum. As a preliminary process for experiment with red-detuned sideband, we observe the resonant spectrum of fundamental mode of mechanical resonator (f_1) without applying rf signal. During the measurement for 1 hour under moderate vacuum (~ 1.8 mbarr) and room temperature (~ 291 K), we could observe the stable resonant response and resonant frequency does not change significantly as shown in Fig. 6.4. Measured quality factor of resonant spectrum is approximately 61,000.

To observe the dynamic response of thermal modes by applied red-detuned sideband ($f_2 - f_1$), we adopted the optical measurement technique which measures the intensity modulation of incident laser light from the surface of mechanical resonator. Stabilized He-Ne laser light ($\lambda = 632.8\text{nm}$) is focused by the objective lens and incident on the surface of mechanical resonator. Thermal motion or thermal self-oscillation of mechanical resonator modulate the intensity of laser beam which is re-collected by the objective lens. Then laser beam is re-focused to the surface of PIN detector by small plano-convex lens to increase the sensitivity to the incident light.

In case of small amplitude of higher modes, external amplifier (MITEQ Co.) is also used to increase the amplitude of resonant response of mechanical resonator and recorded by the spectrum analyzer.(PXA series, Agilent Co.). To reduce the low-frequency noise in the incoming electrical signal from the photo-detector(PD), DC-block(Minicircuits Co.) is also used to suppress the low frequency (~ 60 Hz, ~ 120 Hz et al.)noise which is mixed to measured signal. Low pass filters(Minicircuits Co.) which reduce the unwanted power spectrum at higher frequency were also used and they helped to reduce the entire noise level of response spectrum of mechanical resonator. To avoid the signal loss by the rf-cable, low-loss rf cable (Huber-Suhner Co.) is used to reduce the signal loss and total loss of power of rf signal while transmitted from PD to spectrum analyzer was measured to be ~ 0.26 dB without connector, DC-block and low-pass filters.

To apply rf-signal at the frequency around the red-detuned sideband ($f_2 - f_1$), DC power supply(Yokogawa Co.) to polarize the dielectric resonator and rf signal generator (Rohde and Schwarz Co.) and function generator (Agilent Co.) to apply rf signal at the frequency around the red-detuned sideband. To polarize the dielectric mechanical resonator with high-mechanical quality factor (Q), DC ± 5 or 10 V was applied across the electrodes which are positioned 200 nm below the moving component in vertical direction with a gap 500 nm in planar direction as shown in fig. 6.5. To reduce the low-frequency electrical noise from the function generator or rf signal generator which is generated by the signal mixer, DC-block was also before connected to electrode. In case of applied rf signal with higher power, although DC-block to protect the low-frequency electrical noise, 120 Hz electrical noise was also carried on the output signal, which is thought to be from function generator in the signal mixing process. In case of high-power rf signal gen-

eration, amplitude of main peak in which we are interested has much more power than the sidebands from the function generator and there difference is approximately more than ~ 90 dB. But when measurement signal is relatively very small to the power of applied rf-signal (≥ 5 dBm), sidebands from the function generator has relatively large amplitude compared to measured amplitude of resonant response (≤ 110 dBm). Thus, in experiment, measured spectral response can contain the electrical noise.

With applied rf-signal around the frequency of red-detuned sideband ($f_2 - f_1$) with 1dBm power, we could observe the splitting of fundamental mode by sideband. We applied rf-signal from the $f_2 - f_1 - 500$ to $f_2 - f_1 + 500$ to investigate change of response spectrum by applied pumping signal. As the frequency of applied rf signal approaches to the exact frequency of red-detuned sideband, resonant response of thermal motion in mechanical resonator begins their splitting into two resonant peaks with tails, one of which from lower resonant spectrum and the other follows the upper resonant spectrum along the applied rf signal.(fig. 6.6) As the applied rf frequency is defined as $f_2 - f_1$ with 1 kHz span, applied rf signal sweeps from lower-right side to upper-left side. When the applied red-detuned sideband shares the energy of 1st resonant mode, 1st mode is parametrically coupled to 2nd mode by applied sideband and mode splitting occurs.

With more pumping power (4 dBm) of applied rf signal of red-detuned sideband frequency, we can observe the decrease of amplitude of resonant response of 1st mechanical mode. With stronger pumping signal, response spectrum shows more clear mode splitting of 1st mechanical mode. resonant frequency in the response spectrum is shifted after sweeping red-detuned sideband and this is attributed to the stronger coupling by stronger driving of red-detuned sideband.

At the pumping power of 8 dBm, we can observe the clear mode-splitting where amplitude of 1st mode of thermal oscillation is decreased to the noise level outside the resonant peak. Resonant frequency of resonant peak is definitely shifted after applying red-detuned sideband. In this measurement, electrical noise with equal spacing of approximately 120 Hz was combined as shown in Fig. 6.8. It was found that function generator which is a source of red-detuned sideband has intrinsic sideband of output signal and their amplitude is relatively larger than expected.

With the pumping power of 12 dBm, mode-splitting of 1st mode is also clearly observed and frequency of resonant spectrum is shifted approximately 300 Hz after sweeping of red-detuned sideband. This shift is attributed to the strong coupling of 1st resonant mode by red-detuned sideband. To reduce the electrical noise which was observed in Fig. 6.8, signal source for red-detuned sideband sweep was replaced from function generator of Agilent Co. to rf-signal generator from Rohde and Schwarz Co. whose sideband noise has smaller than function generator of Agilent.

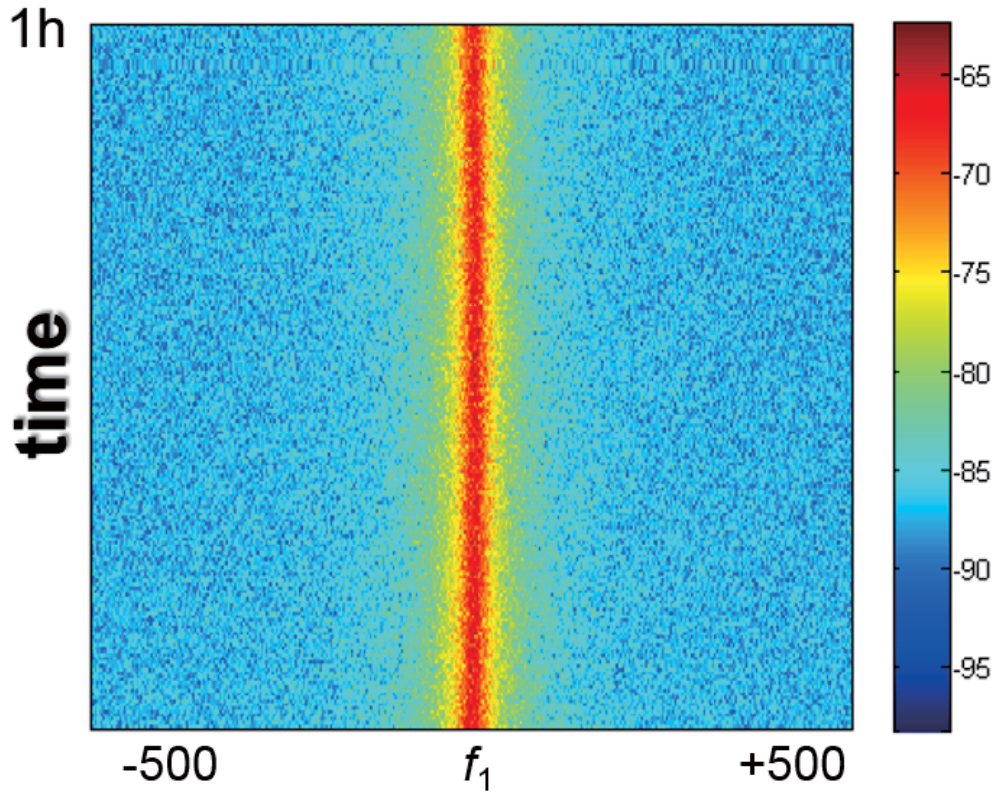


Figure 6.4: Stability of 1st mode in thermal oscillation. To investigate the resonant response spectrum while applying red-detuned sideband, stability of 1st and 2nd mechanical mode is important to apply exact red-detuned sideband frequency as red-detuned sideband frequency is defined as $f_2 - f_1$. To check the stability of mechanical resonant mode, we measured the spectral response of 1st thermal mode of mechanical resonator for approximately 1 hour. As shown in upper figure, mechanical resonant response is confirmed to be sufficiently stable during measurement step. During this measurement, external amplifier was used to amplify the response spectrum from the photo-detector

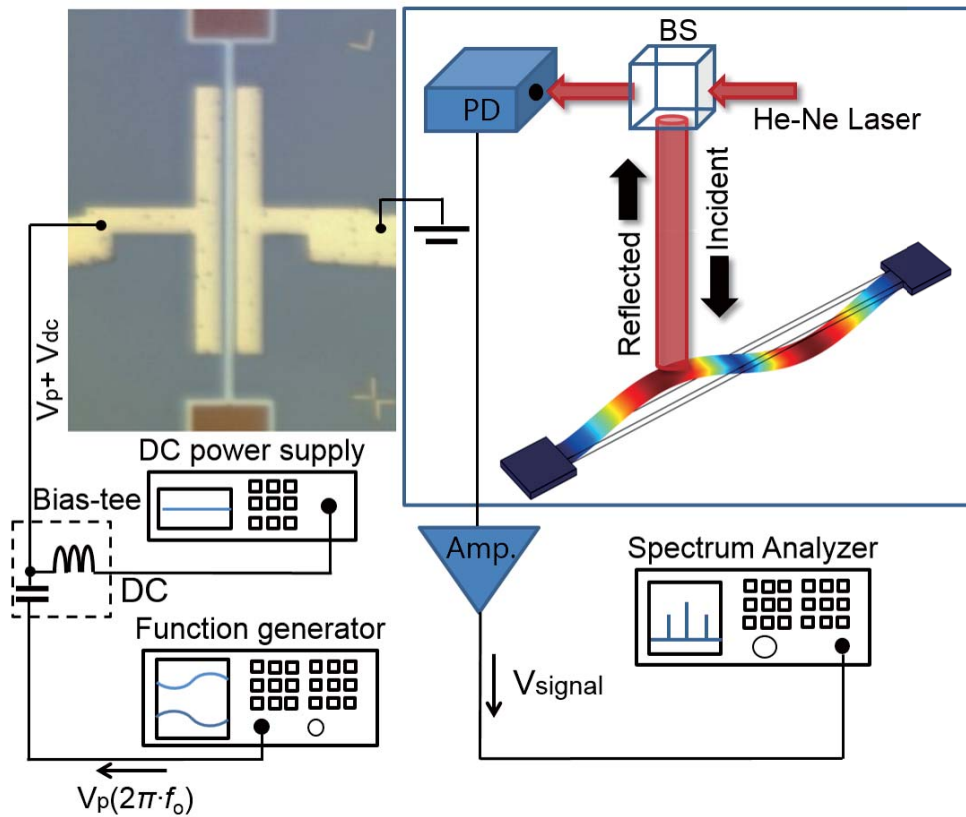


Figure 6.5: To observe the thermal modes of mechanical resonator with optical technique, intensity of laser beam reflected on the surface of mechanical resonator is measured by the photo-detector (PD). To apply the red-detuned sideband to the electrode, one electrode of mechanical resonator is grounded and the other electrode is connected to the rf line from function generator and DC power supply. Intensity modulation by mechanical resonator in thermal mode is recorded by the PD and its spectral response is recorded by the spectrum analyzer. Because of their small intensity at the higher modes, an external amplifier is also used when needed.

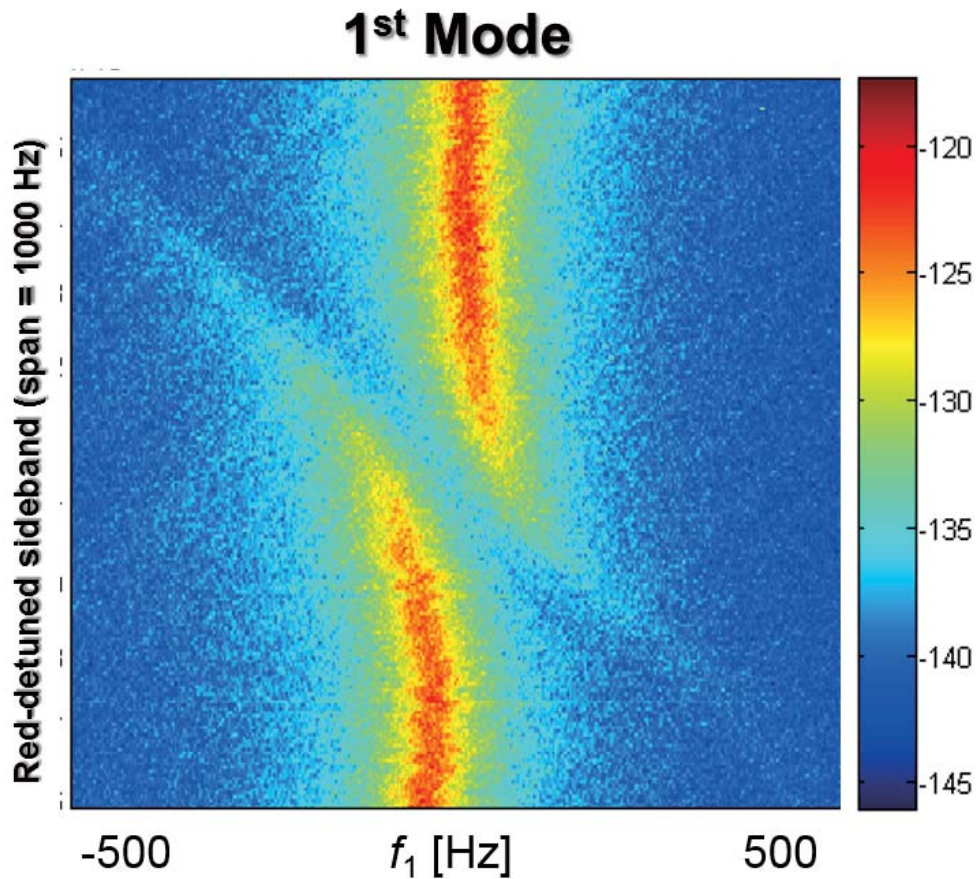


Figure 6.6: Mode-splitting by red-detuned sideband of 1 dBm power. As red-detuned sideband sweeps the resonant response of 1st mode of mechanical resonator, from higher frequency to lower frequency in the resonant response spectrum, mode splitting of 1st mode occurs and amplitude of resonant amplitude decreases when applied rf frequency meets the red-detuned sideband ($f_2 - f_1$). Red-detuned sideband shares the mechanical energy of 1st mode and transfer energy to 2nd mode by parametric coupling between 1st and 2nd mode via applied sideband.

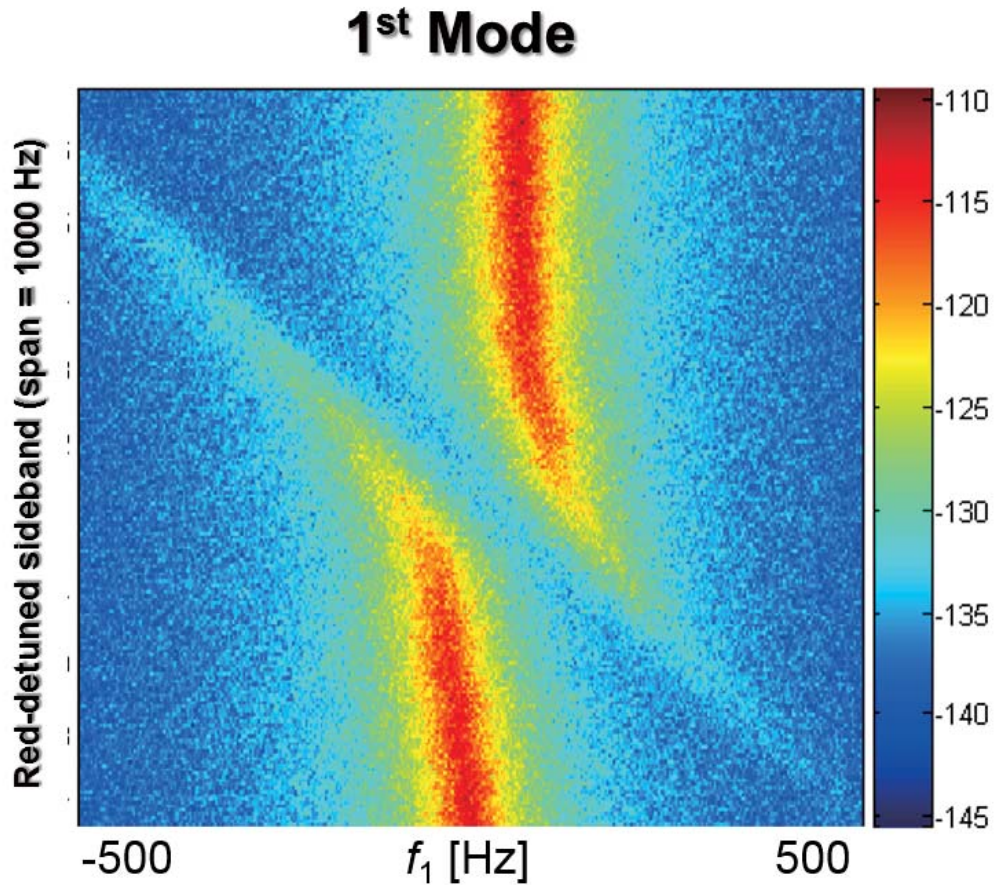


Figure 6.7: Mode-splitting by red-detuned sideband 4 dBm power. As red-detuned sideband sweeps the resonant response of 1st mode of mechanical resonator, from higher frequency to lower frequency in the resonant response spectrum, mode splitting of 1st mode occurs and amplitude of resonant amplitude decreases when applied rf frequency meets the red-detuned sideband ($f_2 - f_1$). Amplitude of resonant response decreases more when applied rf frequency meets the exact red-detuned sideband and amplitude of applied rf power is increased.

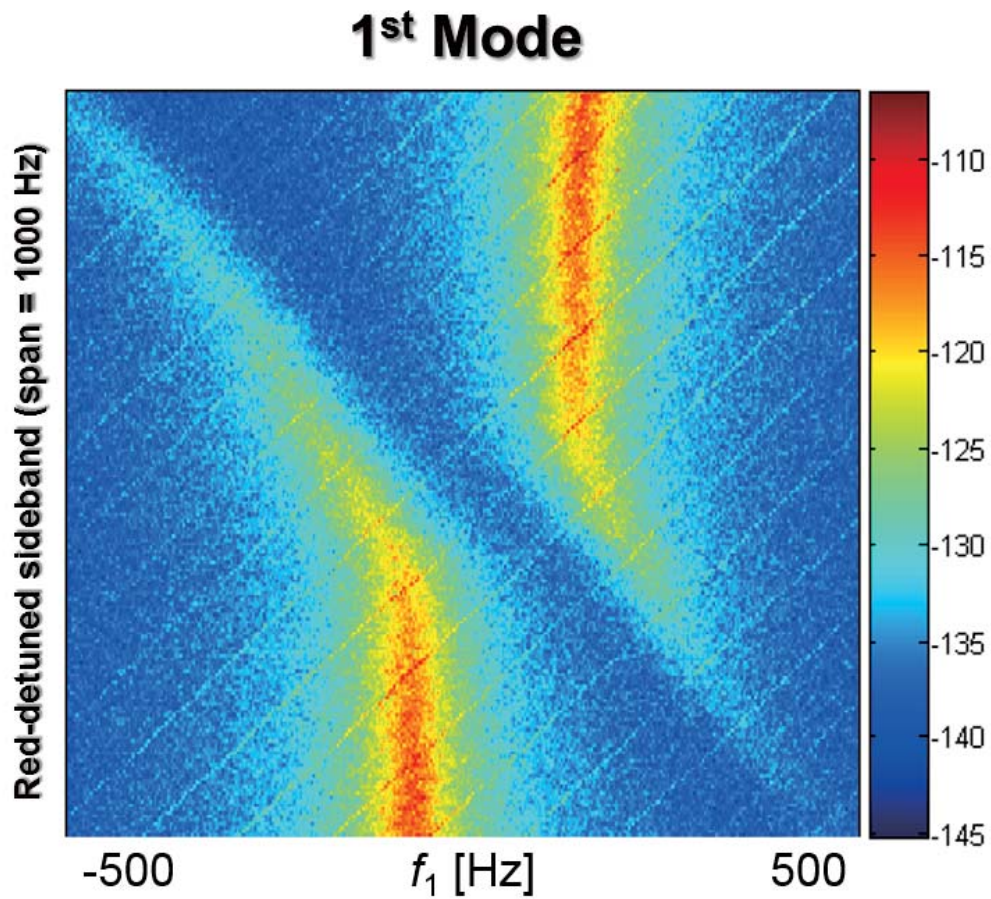


Figure 6.8: Mode-splitting by red-detuned sideband 8 dBm power. With 8 dbm red-detuned sideband pumping, clearer mode splitting is observed and amplitude of resonant response is decreased down to the level of noise outside the resonant response. Regular electrical noise peak with 120 Hz spacing is also observed.

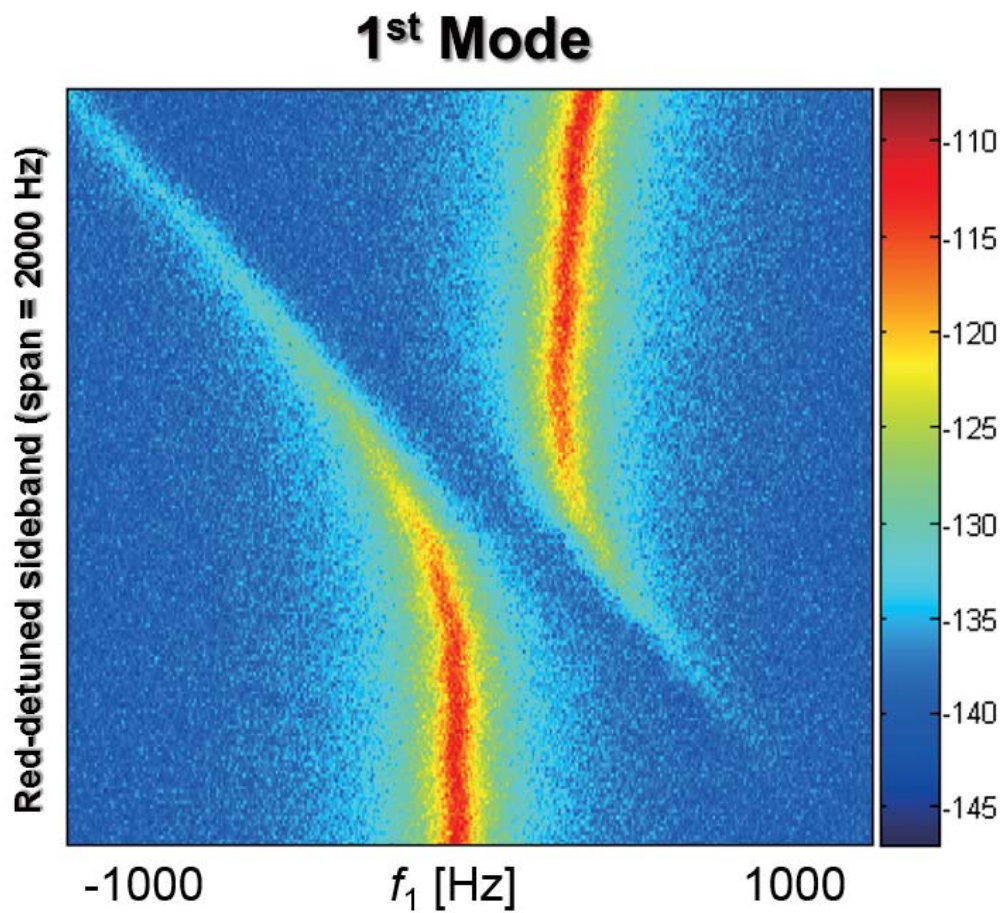


Figure 6.9: Mode-splitting by red-detuned sideband 12 dBm power. Using the rf signal generator with sideband noise of smaller amplitude, electrical noise with 120 Hz regular spacing was removed. By increased red-detuned sideband pumping power, 1st mode is more strongly coupled and resonant frequency of 1st mode is shifted to higher frequency.

6.4 Mode-splitting of 2nd mode by red-detuned mechanical sideband

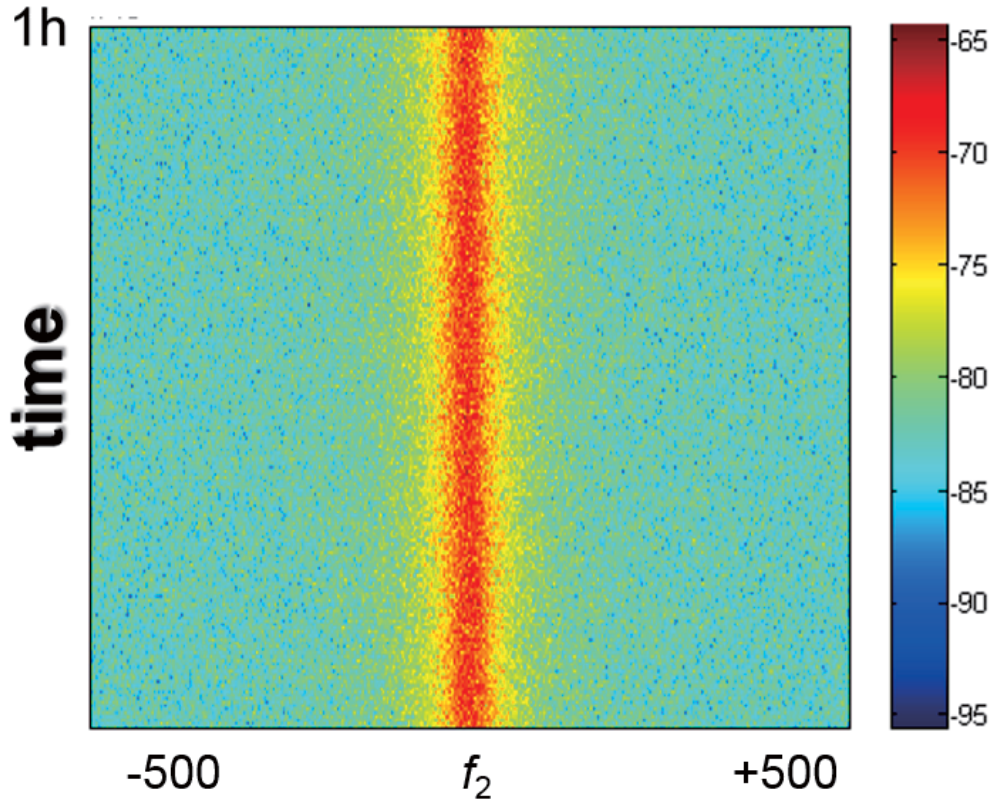


Figure 6.10: Stability of 2nd mode in thermal oscillation. To investigate the resonant response spectrum while applying red-detuned sideband, stability of 2nd mechanical mode is also important to apply exact red-detuned sideband frequency as mentioned in the case of 1st mode. To check the stability of mechanical resonant mode, we measured the spectral response of 2nd thermal mode of mechanical resonator for approximately 1 hour. As shown in the figure, mechanical resonant response is confirmed to be sufficiently stable during measurement step. External amplifier was also used to amplify the response spectrum from the photo-detector

To investigate the response of 2nd (f_2) oscillation mode of mechanical resonator by applied the red-detuned sideband, we should be able to control and observe the resonant motion of 2nd mode during the measurement of

spectrum. Thus we observe the resonant spectrum of 2nd mode of mechanical resonator(f_2) without applying rf signal. During the measurement for 1 hour under same condition for measurement of 1st mode,($P\sim 1.8$ mW, $T\sim 291$ K), we could also observe the stable resonant response and resonant frequency does not change significantly as shown in Fig. 6.10. Measured quality factor of resonant spectrum is approximately 63,000.

In case of 2nd mode, amplitude of resonant response is smaller than 1st mode. But with high sensitivity of optical measurement and electrical measurement technique, we did not need to use external amplifier and we could observe the mode-splitting and amplitude increase of 2nd mode by red-detuned sideband ($f_2 - f_1$).

With applied rf-signal around the frequency of red-detuned sideband ($f_2 - f_1$) with 1dBm power, mode-splitting of 2nd mode was observed. Rf-signal from the $f_2 - f_1 - 500$ to $f_2 - f_1 + 500$ was applied to the electrodes to investigate change of response spectrum. As the frequency of applied rf signal approaches to the exact frequency of red-detuned sideband, 2nd resonant response of thermal motion is separated by red-detuned sideband which is swept from lower-left spectrum to upper-right spectrum.

We can observe the increase of amplitude of resonant response of 2nd mechanical mode by stronger red-detuned sideband. With stronger pumping signal, response spectrum shows more clear mode splitting of 2nd mechanical mode. Coupling strength increases by strong red-detuned sideband pumping and the intensity of resonant peak by both 2nd mode and red-detuned sideband has maximum amplitude around the exact red-detuned frequency ($f_2 - f_1$).

At the pumping power of 8 dBm, we can observe the clear mode-splitting where amplitude of 2nd mode of thermal oscillation is increased, but the

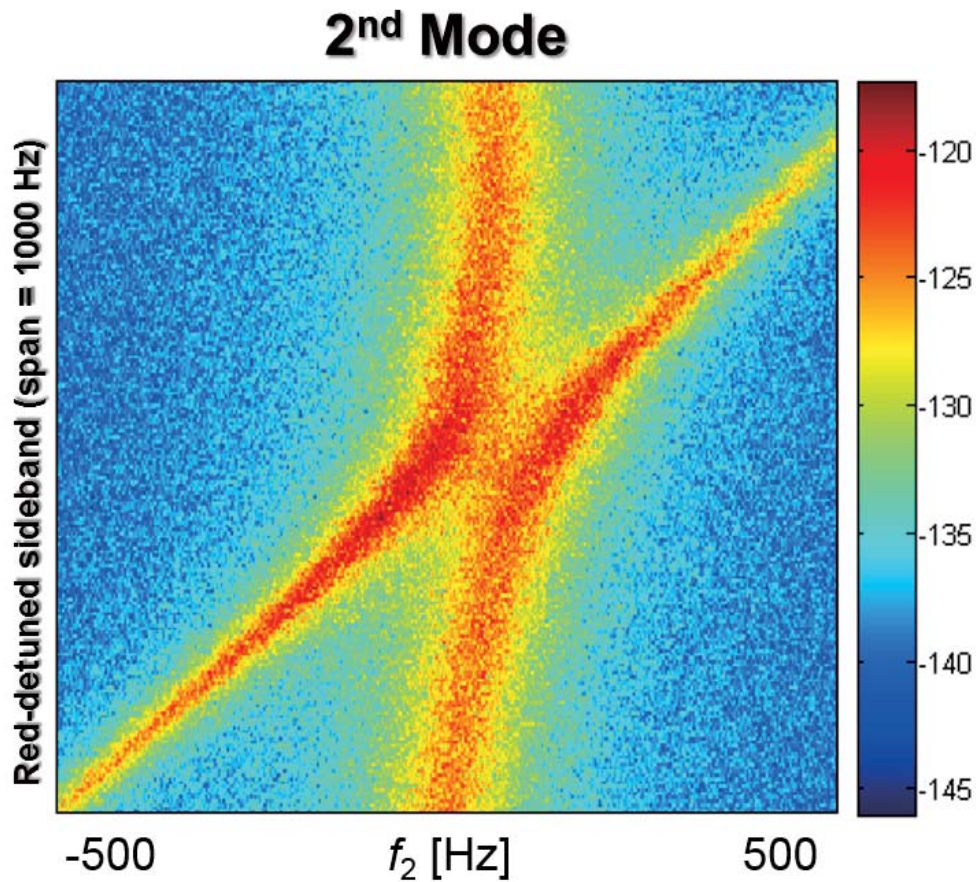


Figure 6.11: Mode-splitting by red-detuned sideband 1 dBm power. As red-detuned sideband sweeps the resonant response of 2nd mode, mode-splitting of 2nd mode occurs and amplitude of resonant amplitude increases when applied rf frequency meets the red-detuned sideband ($f_2 - f_1$). Red-detuned sideband shares the mechanical energy of 1st mode is transferred to 2nd mode by parametric coupling between 1st and 2nd mode via applied sideband and amplitude increase can be observed during mode-splitting

amplitude of 2nd mode where applied rf-frequency is exactly $f_2 - f_1$ do not decrease to the level of noise outside the resonant response. Electrical noise with equal spacing of approximately 120 Hz was combined as shown in Fig. 6.13 and noise is clearly observed around the point of mode-splitting. Function generator was a source of electrical noise which is mixed with red-detuned sideband as already mentioned in the case of mode-splitting of 1st mode.

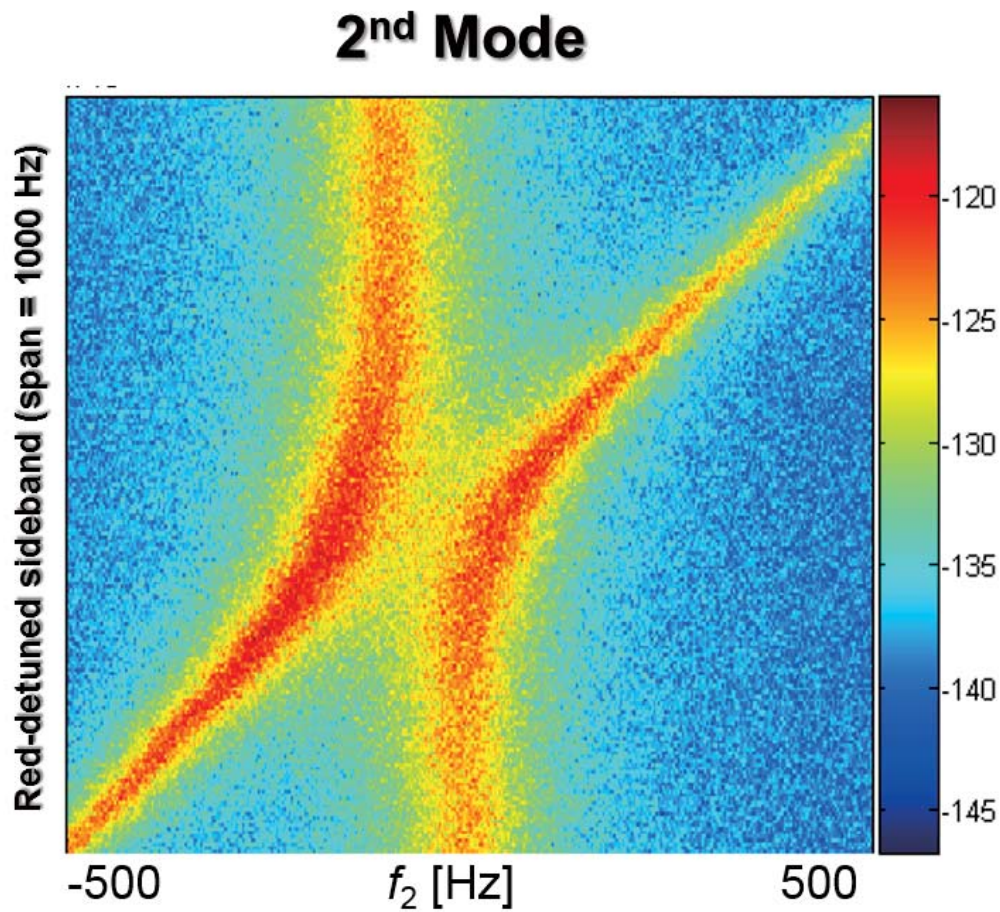


Figure 6.12: Mode-splitting by red-detuned sideband 4 dBm power. As red-detuned sideband sweeps the resonant response of 2nd mode, from lower frequency to higher frequency in the resonant response spectrum, mode splitting of 2nd mode was increased and amplitude of resonant amplitude increased when applied rf frequency meets the red-detuned sideband ($f_2 - f_1$).

With the pumping power of 12 dBm, mode-splitting of 2nd mode is also clearly observed but amplitude does not decrease to the noise level where red-detuned sideband is exactly $f_2 - f_1$. To reduce the electrical noise which was observed as shown in Fig. 6.13, signal source for red-detuned sideband was replaced from function generator of Agilent Co. to rf-signal generator from Rohde and Schwarz Co.

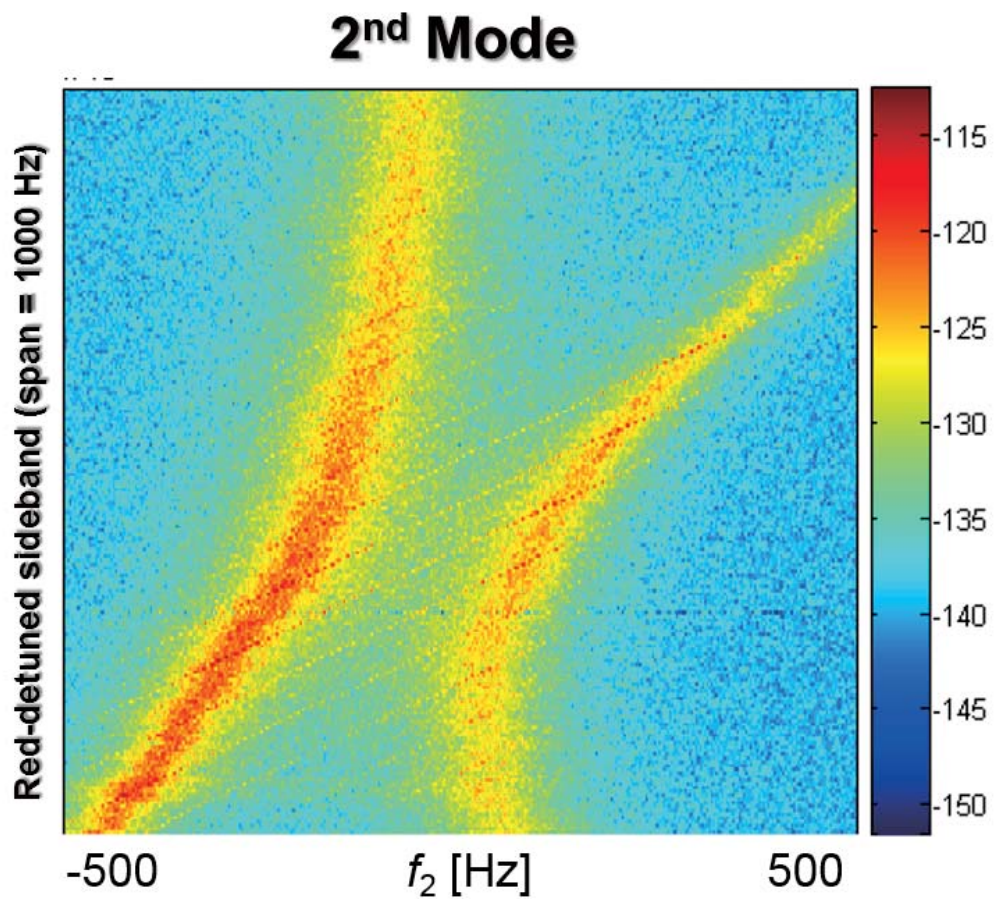


Figure 6.13: Mode-splitting by red-detuned sideband 8 dBm power. With 8 dbm red-detuned sideband pumping, clearer mode-splitting is observed and amplitude of resonant response is increased as shown in resonant spectrum with smaller pumping power. Because of intrinsic noise of function generator, regular electrical noise peak with 120 Hz spacing is also observed as shown in the mode-splitting of 1st mode by 8 dBm red-detuned sideband pumping.

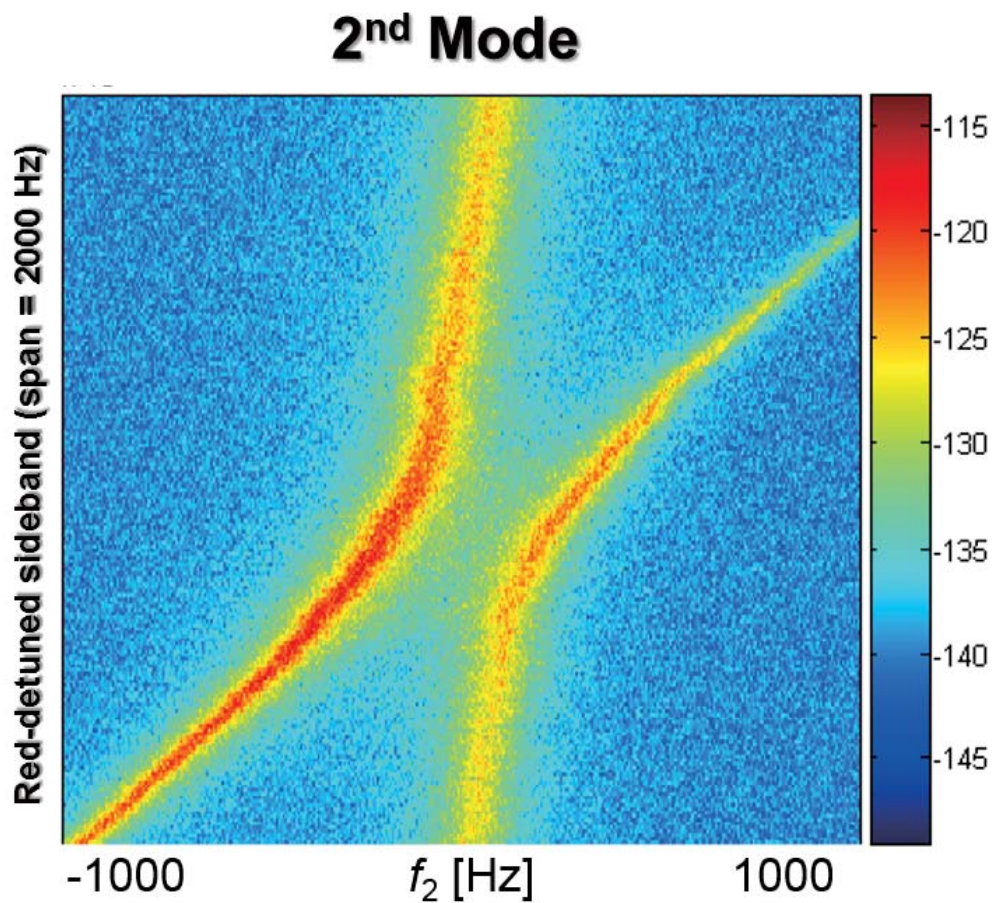


Figure 6.14: Mode-splitting by red-detuned sideband 12 dBm power. Using the rf signal generator with sideband noise of smaller amplitude, electrical noise with 120 Hz regular spacing is also removed like the 1st mode resonant response with same pumping power. By increased red-detuned sideband pumping power, 2nd mode is more strongly coupled by red-detuned sideband.

Chapter 7

Mechanical amplification of thermal motion in micromechanical resonator by mechanical sideband

As the NEMS devices are fashioned into smaller dimensions, sensitive measurement of fine electrical signal become more important. With the development of measurement technique such as sensitive detector (Avalanche photo-detector et al.) and high-gain amplifier with low-noise profile (Josephson parametric amplifier et al.), researches to increase the sensitivity of mechanical resonator to external signal based on physical phenomena were tried to hurdle the challenges in precise measurement. Nonlinear parametric amplification have shown its potentials in amplifying displacement amplitude of mechanical resonators and its deamplification by squeezing of mechanical motion. But, along with these successes in amplification by parametric amplification, there were some limitations in parametric amplification. Due to

its nature of amplification that amplification gain depends on the amplitude of response without pumping, efficiency in parametric amplification is limited when we should amplify the small displacement amplitude.

To overcome this limitation in parametric amplification, we applied the scheme of controlling the motion of mechanical resonator by mechanical sideband. With the sideband technique to induce mode-splitting for 1st and 2nd mechanical mode and cooling effect by transferring the energy of 1st mode to 2nd mode of mechanical resonator, which is stated in previous chapter, we can also use blue-sideband technique to amplify the displacement amplitude of mechanical resonator. By applying the blue-sideband pumping rf-signal ($f_1 + f_2$), we can observe the amplification of displacement amplitude for both 1st and 2nd mode.

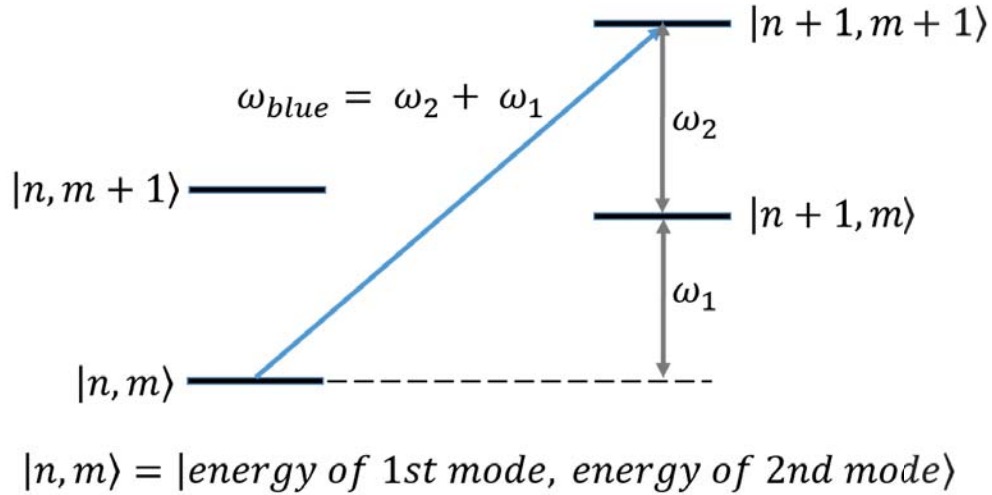


Figure 7.1: Schematic diagram of amplification by blue-detuned sideband. By applying blue-detuned sideband of 1st and 2nd mode ($f_1 + f_2$) of the mechanical resonator, mechanical resonator in the state $|n, m\rangle$ is excited to $|n + 1, m + 1\rangle$. By distributing the energy of blue-detuned sideband to both 1st and 2nd vibrational mode of mechanical resonator, 1st and 2nd mode of mechanical resonator are excited and their displacement amplitude is amplified.

To investigate the response of mechanical resonator by applied the red-detuned sideband of 1st (f_1) and 2nd (f_2) oscillation mode of mechanical resonator, we should be able to control and observe the resonant motion of 1st and 2nd mode during the measurement of spectrum. As a preliminary process for experiment with red-detuned sideband, we observe the resonant spectrum of fundamental mode of mechanical resonator (f_1) without applying rf signal. During the measurement for 1 hour under moderate vacuum (~ 1.8 mbarr) and room temperature (~ 291 K), we could observe the stable resonant response and resonant frequency does not change significantly as shown in Fig. 6.4. Measured quality factor of resonant spectrum is approximately 61,000.

7.1 Mechanical amplificataion of 1st mode by blue-detuned sideband

To observe the dynamic response of thermal modes by applied blue-detuned sideband (f_1+f_2), we used the same measurement technique which was used to observe the dynamic response by red-detuned sideband pumping. Stabilized He-Ne laser light ($\lambda = 632.8nm$) is focused by the objective lens and incident on the surface of mechanical resonator. 1st and 2nd vibrational mode of mechanical resonator modulate the intensity of laser beam which is re-collected by the objective lens and re-focused to the surface of PIN detector by small plano-convex lens. Spectral response of 1st and 2nd vibrational mode of mechanical resonator was recorded by the spectrum analyzer.(PXA series, Agilent Co.). DC-block(Minicircuits Co.) and low-pass filters (Minicircuits Co.) are also used to suppress the low frequency (~ 60 Hz, ~ 120 Hz et al.) and high frequency noise which is carried with the signal. To avoid the signal loss by the rf-cable, low-loss rf cable (Huber-Suhner Co.) was also used to reduce the signal loss.

To apply rf-signal at the frequency around the blue-detuned sideband (f_1+f_2), DC power supply(Yokogawa Co.) was used to polarize the dielectric resonator. Either Rf signal generator (Rohde and Schwarz Co.) or function generator (Agilent Co.) was used to apply rf signal at the frequency around the blue-detuned sideband. Rf signal generator from Rohde and Schwarz Co. showed better noise figure and above certain blue-detuned pumping power, intrinsic noise of input signal was also amplified. To polarize the dielectric mechanical resonator, DC ± 5 or 10 V was applied across the electrodes which are positioned 200 nm below the moving component in vertical direction with a gap 500 nm in planar direction as shown in previous chapter (fig. 6.5). In

case of applied rf signal with higher power, although DC-blocks were used to protect the low-frequency electrical noise, 120 Hz electrical noise was also carried along with the output signal, which is thought to be from function generator in the signal mixing process.

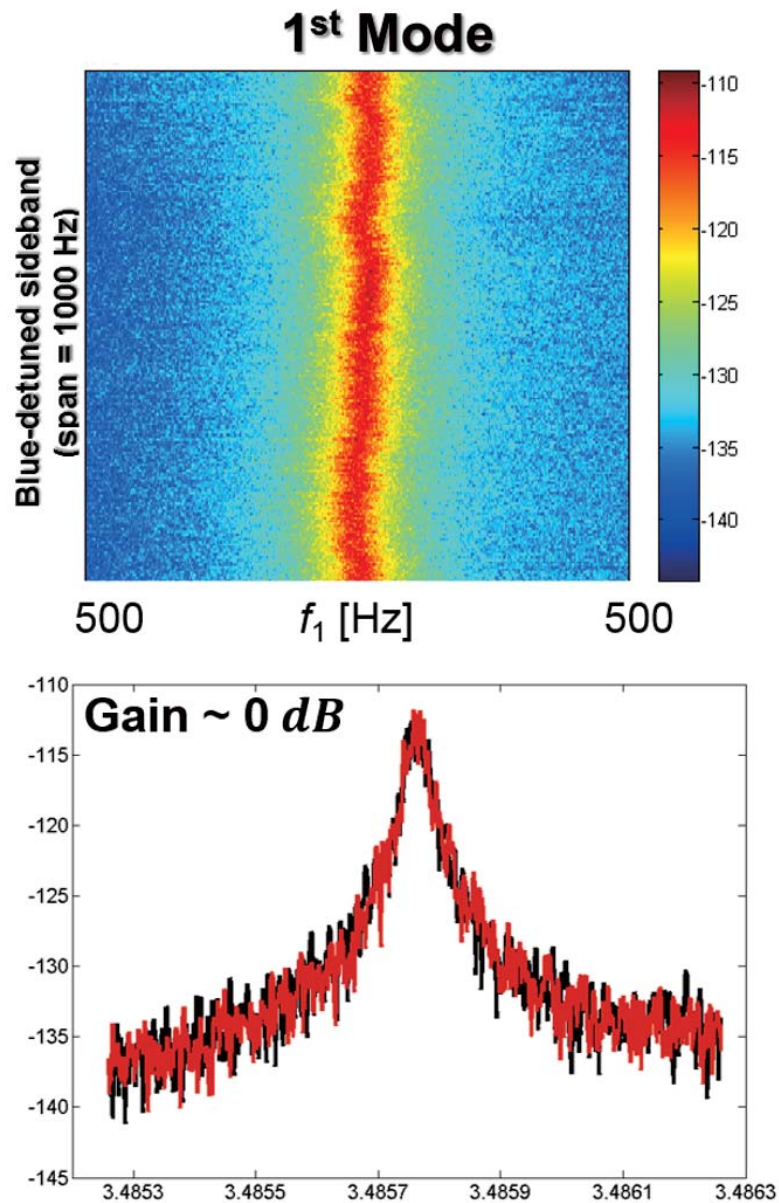


Figure 7.2: Amplification by blue-detuned sideband of -4 dBm. Response of 1st mode resonant peak to the applied blue-detuned sideband pumping with -4 dBm power(upper). While sweeping the frequency of blue-detuned sideband from $f_1 + f_2 - 500$ to $f_1 + f_2 + 500$ Hz, we observe resonant response of 1st mode of thermal self-oscillation in mechanical resonator. With the pumping power of -4 dBm, we cannot observe any meaningful change of response spectrum of 1st mode. Thus there is no gain in displacement amplitude (lower)

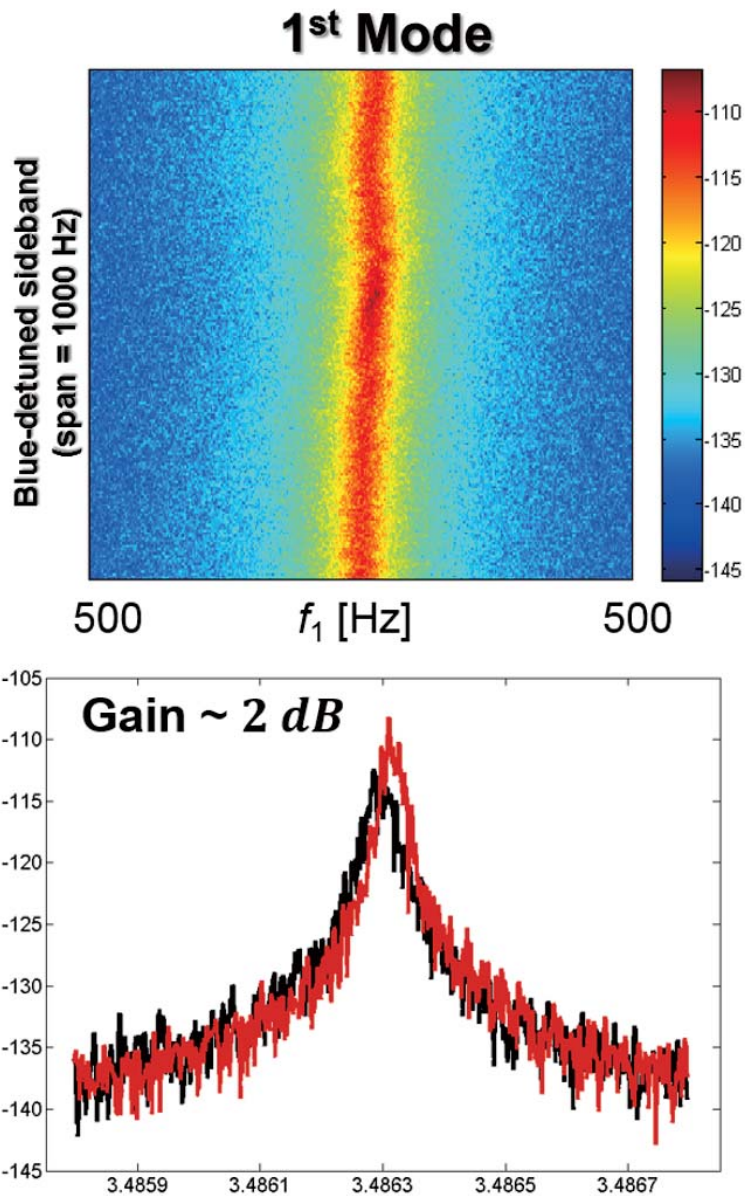


Figure 7.3: Amplification by blue–detuned sideband of -1 dBm. Response of 1st mode resonant peak to the applied blue–detuned sideband pumping with -1 dBm power(upper). While sweeping the frequency of blue–detuned sideband from $f_1 + f_2 - 500$ to $f_1 + f_2 + 500$ Hz, we observe resonant response of 1st mode of thermal self-oscillation in mechanical resonator. Comparing the amplitude of resonant peak between with pumping (red) and without pumping (black), we can observe the gain of 2 dB by blue–detuned sideband of -1 dBm power (lower).

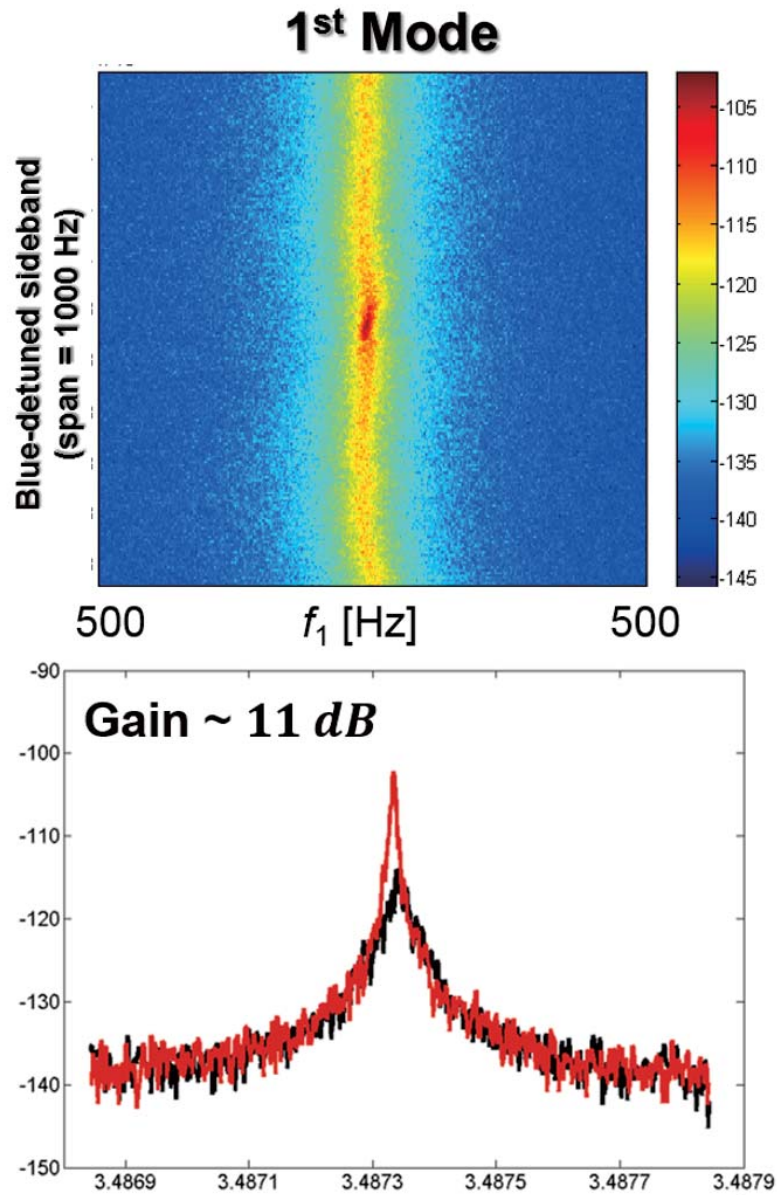


Figure 7.4: Amplification by blue-detuned sideband of 2 dBm. Response of 1st mode resonant peak to the applied blue-detuned sideband pumping with 2 dBm power(upper). While sweeping the frequency of blue-detuned sideband from $f_1 + f_2 - 500$ to $f_1 + f_2 + 500$ Hz, we observe resonant response of 1st mode of thermal self-oscillation in mechanical resonator. Comparing the amplitude of resonant peak between with pumping (red) and without pumping (black), we can observe the gain of 11 dB by blue-detuned sideband of 2 dBm power (lower)

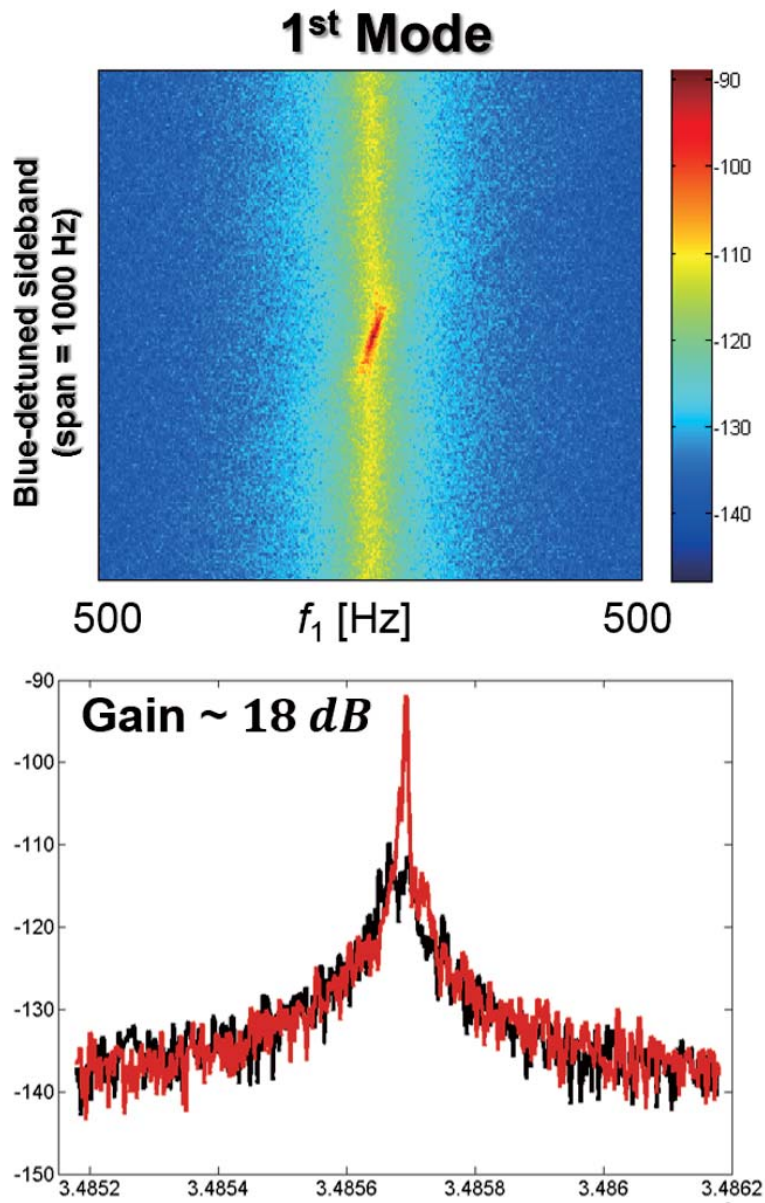


Figure 7.5: Amplification by blue-detuned sideband of 4 dBm. Response of 1st mode resonant peak to the applied blue-detuned sideband pumping with 4 dBm power(upper). While sweeping the frequency of blue-detuned sideband from $f_1 + f_2 - 500$ to $f_1 + f_2 + 500$ Hz, we observe resonant response of 1st mode of thermal self-oscillation in mechanical resonator. Comparing the amplitude of resonant peak between with pumping (red) and without pumping (black), we can observe the gain of 18 dB by blue-detuned sideband of 4 dBm power (lower)

7.2 Mechanical amplification of 2nd mode by blue-detuned sideband

Under the same condition and with same apparatus for the measurement of 1st mode amplification in chapter 7.1, we observed the response of 2nd mode of thermal self-oscillation in mechanical resonator to blue-detuned sideband pumping. To observe the response of 2nd mode, we moved the spot of laser beam to the position of 20 μm distant from the clamp. 2nd mode oscillation of mechanical resonator has anti-nodal point at this position and we can investigate the response of 2nd mode by blue-detuned sideband with maximum displacement amplitude. The intensity modulated laser beam is focused onto the photo-detector and their intensity is recorded by spectrum analyzer and DC-block(Minicircuits Co.), low-pass filter (Minicircuits Co.), and low-loss rf-cables are also used to suppress the low frequency (~ 60 Hz, ~ 120 Hz et al.) and high frequency noise which is carried with the signal to investigate the 2nd mode which shows weaker optical signal.

While applying the blue-detuned sideband and observing the dynamic response of 2nd mode, 2nd mode showed higher gain and responded more sensitively to the applied sideband. Amplification gain began to increase with smaller power of blue-detuned sideband and showed higher gain at the same pumping power. Even with the highest pumping power which can avoid the quenching of optical signal by unwanted amplification of sideband noise from rf signal generator(or function generator), we can get higher gain in case of 2nd mode of mechanical resonator.

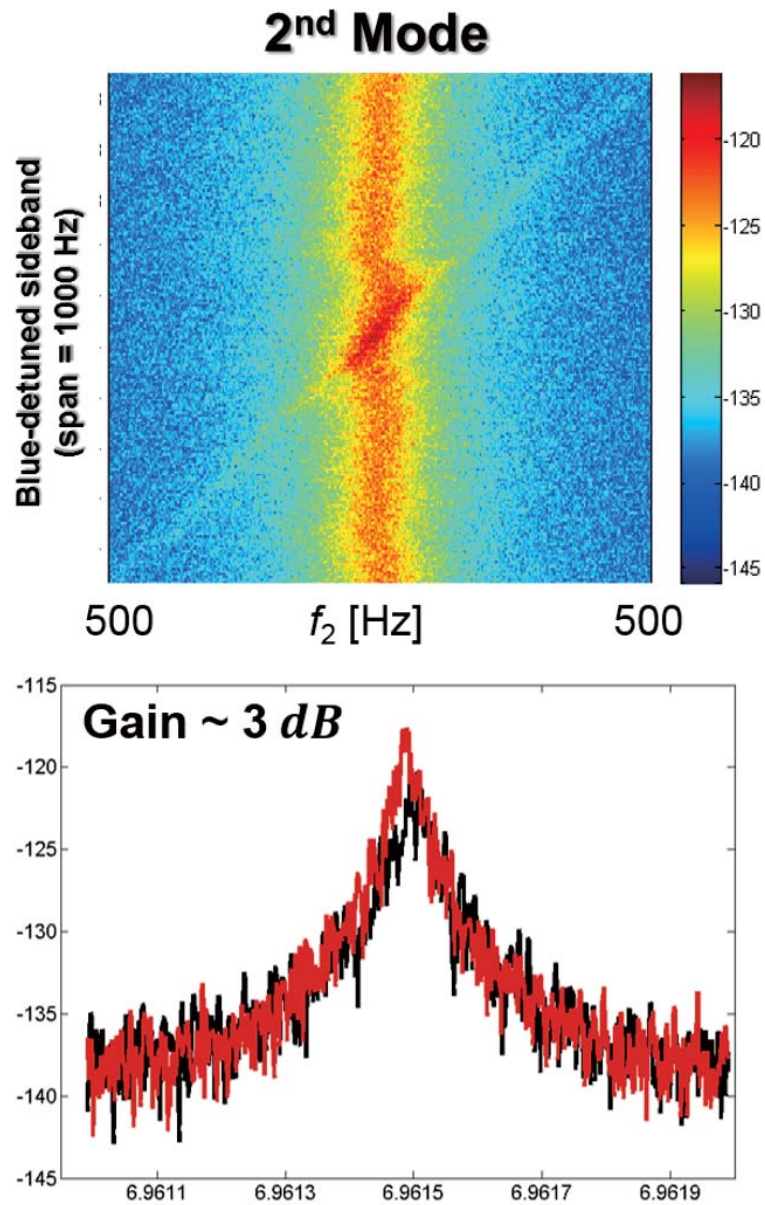


Figure 7.6: Amplification by blue-detuned sideband of -4 dBm. Response of 2nd mode resonant peak to the applied blue–detuned sideband pumping with -4 dBm is observed(upper). While sweeping the frequency of blue–detuned sideband from $f_1 + f_2 - 500$ to $f_1 + f_2 + 500$ Hz, we observe resonant response of 2nd mode fo thermal self-oscillation in mechanical resonator. Comparing the amplitude of resonant peak between with-pumping (red) and without-pumping (black), we can observe the gain of 3 dB by blue–detuned sideband of -4 dBm power (lower)

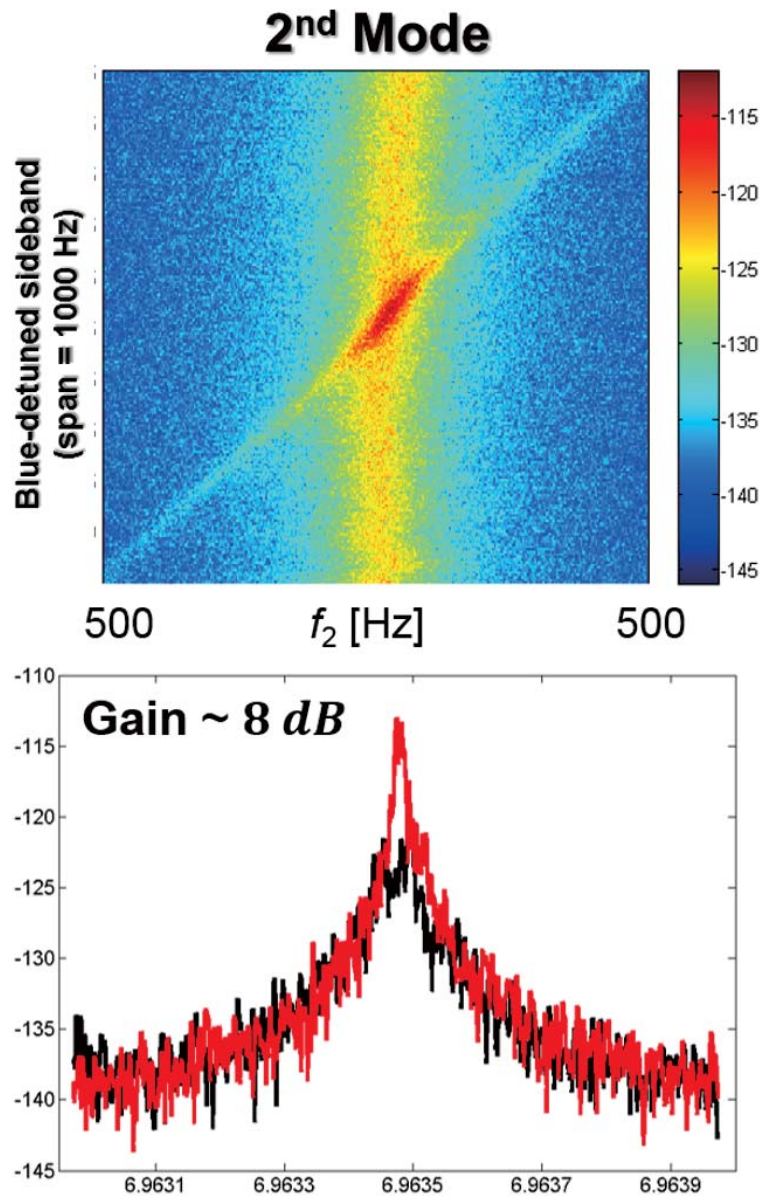


Figure 7.7: Amplification by blue-detuned sideband of -1 dBm. Response of 2nd mode resonant peak to the applied blue–detuned sideband pumping with -1 dBm is observed(upper). While sweeping the frequency of blue–detuned sideband from $f_1 + f_2 - 500$ to $f_1 + f_2 + 500$ Hz, we observe resonant response of 2nd mode fo thermal self-oscillation in mechanical resonator. Comparing the amplitude of resonant peak between with-pumping (red) and without-pumping (black), we can observe the gain of 8 dB by blue–detuned sideband of -1 dBm power (lower)

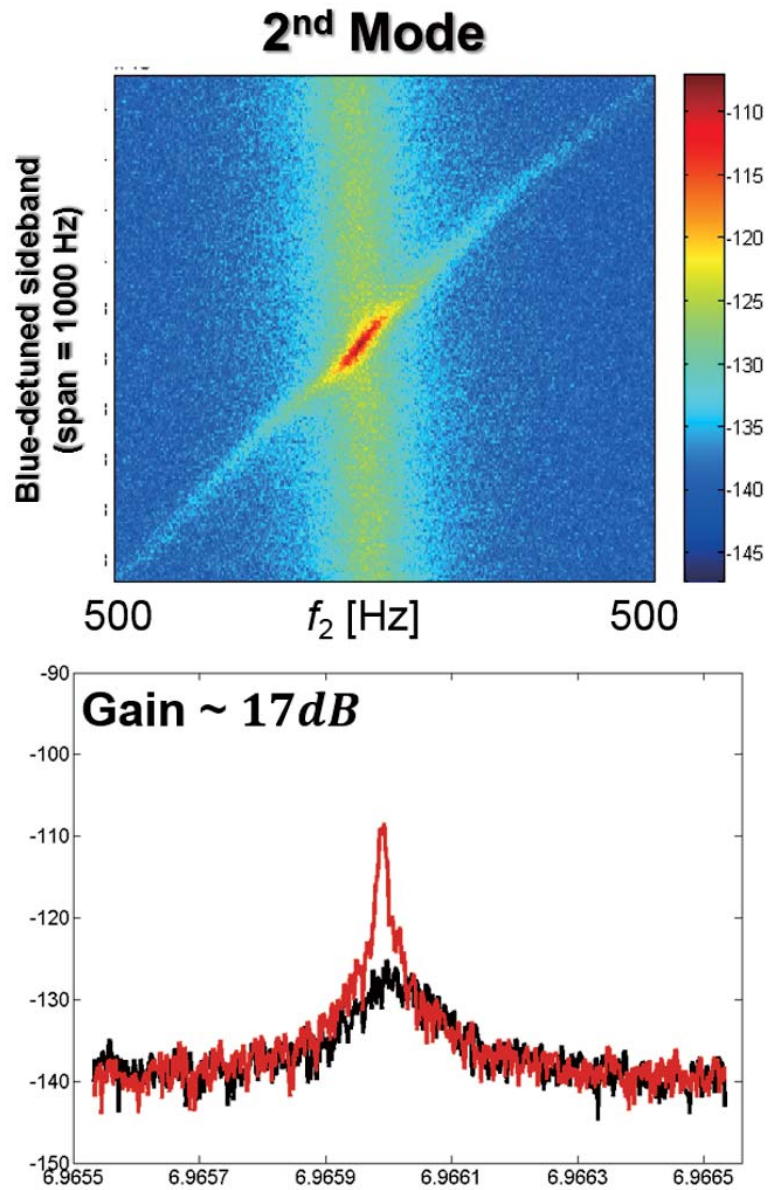


Figure 7.8: Amplification by blue-detuned sideband of 2 dBm. Response of 2nd mode resonant peak to the applied blue–detuned sideband pumping with 2 dBm is observed(upper). While sweeping the frequency of blue–detuned sideband from $f_1 + f_2 - 500$ to $f_1 + f_2 + 500$ Hz, we observe resonant response of 2nd mode fo thermal self-oscillation in mechanical resonator. Comparing the amplitude of resonant peak between with-pumping (red) and without-pumping (black), we can observe the gain of 17 dB by blue–detuned sideband of 2 dBm power (lower)

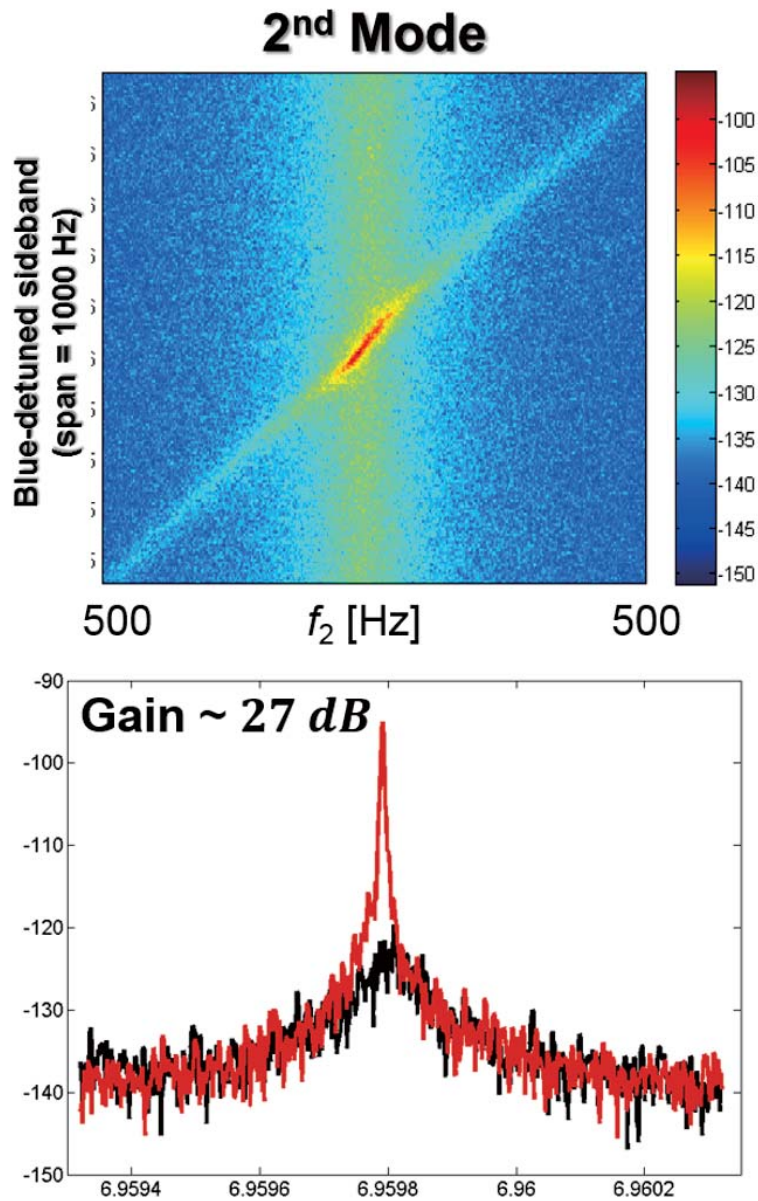


Figure 7.9: Amplification by blue-detuned sideband of 4 dBm. Response of 2nd mode resonant peak to the applied blue–detuned sideband pumping with 4 dBm is observed(upper). While sweeping the frequency of blue–detuned sideband from $f_1 + f_2 - 500$ to $f_1 + f_2 + 500$ Hz, we observe resonant response of 2nd mode fo thermal self-oscillation in mechanical resonator. Comparing the amplitude of resonant peak between with-pumping (red) and without-pumping (black), we can observe the gain of 27 dB by blue–detuned sideband of 4 dBm power (lower)

Chapter 8

Summary and outlook

Nano- and Micro-mechanical resonators of doubly-clamped and square-membrane geometry are basic components of NEMS (Nano-ElectroMechanical System) and MEMS (Micro-ElectroMechanical System) and they showed great potentials in recent research and applications. To fully take advantage of mechanical resonator, we fabricated mechanical resonator with high mechanical Q from high-stress silicon nitride (Si_3N_4). Because of high mechanical stress of approximately 800 MPa, elastic energy is preserved in the mechanical structure and mechanical quality factor can increase more than 100,000. This high-stress can also allow high-frequency operation of mechanical resonator compared to silicon compatible materials with less or without stress. Their resonant frequencies of n -th mechanical resonant mode become close to n -integer of resonant frequency of fundamental mode.

To prevent the increased damping by measurement and actuation technique which can be great challenges in research and application such as mechanical transducer and precise sensor, actuation and measurement technique different from techniques already used in NEMS and MEMS, Actuation with electrical field gradient force drives mechanical resonators of dielectric ma-

terial with dielectric interaction between dipole moment in mechanical resonator and applied rf-signal. This technique do not need additional component on the moving components, thus, preserve the high mechanical quality factor of mechanical resonator from high-stress Si_3N_4 . By combining the optical measurement technique, we can measure the resonant response of mechanical resonator of doubly-clamped and square-membrane geometry

With realized doubly-clamped and membrane mechanical, we applied nonlinear parametric oscillation phenomena to mechanical resonator to amplify the displacement amplitude by applying 2ω where ω is $2\pi \cdot f$ and f is the resonant frequency of mechanical resonator. We also observed the amplification and deamplification of displacement amplitude corresponding to pumping power and relative phase between ω and 2ω . Maximum gain by parametric amplification goes up to approximately 9.7 with phase difference at $\theta = 90^\circ$ and deamplification with phase difference at $\theta = 0^\circ$.

With optical technique combined with improved electronics, we investigated the thermal self-oscillation of mechanical resonator to higher vibrational modes. By mapping the power spectral density along the mechanical resonator with 500 nm step, we could resolve and reconstruct mode shape of thermal self-oscillation to 4th mode and compare the relative displacement among mechanical modes. Different from the relative displacement among mechanical modes in driven oscillation, displacement of higher modes are reduced in thermal self-oscillation.

Using mechanical modes of thermal self-oscillation, we could manipulate the mechanical modes by mechanical sideband. Mechanical resonator as a nonlinear device, mechanical resonator can generate mechanical sidebands by mixing mechanical vibrational modes. With red-detuned mechanical sideband ($f_2 - f_1$), we can couple the 1st mechanical mode with 2nd mechanical

mode by applying rf-signal of red-detuned sideband frequency. Parametric coupling of mechanical mode was confirmed by mode-splitting in both 1st and 2nd mode. With blue-detuned mechanical sideband ($f_2 + f_1$), we can amplify the amplitude of vibrational mode of thermal self-oscillation. We can observe the real gain of amplification approximately 20 dB in 1st mode and 30 dB in 2nd mode. This sideband amplification technique do not require phase sensitive pumping and smaller vibrational mode such as thermal vibrational mode can be amplified, and using multiple vibrational modes, mechanical resonator with fixed dimensions can operate in wide bandwidth of frequency.

Mechanical resonator with high mechanical quality factor can have great potential in research and applications. With improved measurement and actuation technique, we can observe and control the fine oscillatory motion of mechanical resonator. For more precise measurement of mechanical resonator, we need to design and stabilize measurement system which is not susceptible to external optical and acoustic noise. From the measurement of thermal self-oscillation and control of mechanical resonator by red- and blue-sideband, isolation of external electrical noise become also important. To fully understand the mode dynamics of mechanical oscillator, we need more study on the mechanism of energy transfer and coupling between different mechanical modes. With understanding of parameters which determine the coupling, such as dissipation rate and oscillation amplitude, we can find profound principles for mode dynamics of mechanical resonator and interactions in between different oscillation modes.

Bibliography

- [1] A. D. O'Connell, M. Hofheinz, M. Ansmann, Radoslaw C. Bialczak, M. Lenander, Erik Lucero, M. Neeley, D. Sank, H. Wang, M. Weides and J. Wenner, John M. Martinis and A. N. Cleland. Quantum ground state and single-phonon control of a mechanical resonator. *Nature* **464**, 697 (2010)
- [2] D. Rugar, R. Budakian, H. J. Mamin and B. W. Chui. Single spin detection by magnetic resonance force microscopy. *Nature* **430**, 329 (2004)
- [3] David Hunger, Stephan Camerer, Theodor W. Hansch, Daniel König, Jorg P. Kotthaus, Jakob Reichel and Philipp Treutlein. Resonant coupling of a Bose-Einstein condensate to a micromechanical oscillator.
- [4] S. Groblacher, K. Hammerer, M. F. Vanner and M. Aspelmeyer. Observation of strong coupling between a micromechanical resonator and an optical cavity field. *Nature* **460**, 724 (2009). *Phys. Rev. Lett.* **104**, 143002 (2010)
- [5] A. Gillespie and F. Raab. Thermally excited vibrations of the mirrors of laser interferometer gravitational-wave detectors. *Phys. Rev. D* **52**, 577 (1995)
- [6] A. A. Clerk, Florian Marquardt and J. G. E. Harris. Quantum measurement of phonon shot noise. *Phys. Rev. Lett.* **104**, 213603 (2010)

- [7] T. P. Purdy, R. W. Peterson, C. A. Regal. Observation fo radiation pressure shot noise on a macroscopic object. *Science* **339**, 301 (2013)
- [8] J. D. Teufel, T. Donner, J. W. Harlow, M. S. Allman, K. Cicak, A. J. Sirois, J. D. Whittaker, K. W. Lehnert and R. W. Simmonds. Observation fo radiation pressure shot noise on a macroscopic object. *Nature* **475**, 359 (2011)
- [9] Jasper Chan, T. P. Mayer Alegre, Amir H. Safavi-Naeini, Jeff T. Hill, Alex Krause, Simon Groblacher, Markus Aspelmeyer and Oskar Painter. Laser cooling of a nanomechanical oscillator into its quantum ground state. *Nature* **478**, 89 (2011)
- [10] G. Zolfagharkhani, A. Gaidarzhy, P. Degiovanni, S. Kettemann, P. Fulde and P. Mohanty. Nanomechanical detection of itinerant electron spin flip. *Nature Nanotech.* **3**, 720 (2008)
- [11] O. Arcizet, V. Jacques, A. Siria, P. Poncharal, P. Vincent and S. Seidelin. A single nitrogen-vacance defect coupled to a nanomechanical oscillator. *Nature Phys.* **7**, 897 (2011)
- [12] Mahmood Bagheri, Menno Poot, Mo Li, Wolfram P. H. Pernice and Hong X. Tang. Dynamic manipulation of nanomechanical resonators in the high-amplitude regime and non-volatile mechanical memory operation. *Nature Nanotechnol.* **6**, 726 (2011)
- [13] F. Massel, T. T. Heikkila, J. M. Pirkkalainen, S. U. Cho, H. Saloniemi, P. J. Hakonen and M. A. Sillanpaa. Microwave amplification with nanomechanical resonators. *Nature* **480**, 351 (2012)
- [14] Andreas Jockel, Matthew T. Rakher, Maria Korppi, Stephan Camerer, David Hunger, Matthias Mader and Philipp Treutlein. Spectroscopy

- of mechanical dissipation in micro-mechanical membranes. *Appl. Phys. Lett.* **99**, 143109 (2011)
- [15] P. L. Yu, T. P. Purdy and C. A. Regal. Control of material damping in high-Q membrane microresonators. *Phys. Rev. Lett* **108**, 083603 (2012)
- [16] J. Liu, K. Usami, A. Naesby, T. Bagci, E. S. Polzik, P. Lodahl and S. Stobbe. High-Q optomechanical GaAs nanomembranes. *Appl. Phys. Lett.* **99**, 243102 (2011)
- [17] Scott S. Verbridge, Jeevak M. Parpia Roberet B. Reichenbach, Leon M. Bellan and H. G. Craighead. High quality factor resonance at room temperature with nanostrings under high tensile stress. *J. Appl. Phys.* **99**, 124304 (2006)
- [18] Jiansheng Wu and Clare C. Yu. How stress can reduce dissipation in glasses. *Phys. Rev. B* **84**, 174109 (2011)
- [19] Seung-Bo Shim, Matthias Imboden and Pritiraj Mohanty. Synchronized oscillation in coupled nanomechanical oscillators. *Science* **316**, 95 (2007)
- [20] A. N. Cleland and M. L. Roukes. A nanometre-scale mechanical electrometer. *Nature* **392**, 160(1998)
- [21] R. Knobel and A. N. Cleland. Piezoelectric displacement sensing with a single-electron transistor. *Appl. Phys. Lett* **81**, 2258 (2002)
- [22] D. W. Carr and H. G. Craighead. Fabrication of nanoelectromechanical systems in single crystal silicon using silicon on insulator substrates and electron beam lithography. *J. Vac. Sci. Technol. B* **15**, 2760 (1997)
- [23] Quirin P. Unterreithmeier, Thomas Faust and Jorg P. Kotthaus. Damping of nanomechanical resonators. *Phys. Rev. Lett* **105**, 027205 (2010)

- [24] B. Ilic, S. Krylov, K. Aubin, R. Reichenbach and H. G. Craighead. Optical excitation of nanoelectromechanical oscillators. *Appl. Phys. Lett* **86**, 193114 (2005)
- [25] Sotiris C. Masmanidis, Rassul B. Karabalin, Iwijn De Vlaminck, Gustaaf Borghs, Mark R. Freeman and Michael L. Roukes. Multifunctional nanomechanical systems via tunably coupled piezoelectric actuation. *Science* **317**, 780 (2007)
- [26] I. Bargatin, I. Kozinsky and M. L. Roukes. Efficient electrothermal actuation of multiple modes of high-frequency nanoelectromechanical resonators. *Appl. Phys. Lett* **90**, 093116 (2007)
- [27] Kimberly L. Turner, Scott A. Miller, Peter G. Hartwell, Noel C. MacDonald, Steven H. Strogatz and Scott G. Adams. Five parametric resonances in a microelectromechanical system. *Nature* **396**, 149 (1998)
- [28] Quirin P. Unterreithmeier, Eva M. Weig and Jorg P. Kotthaus. Universal transduction scheme for nanomechanical systems based on dielectric forces. *Nature* **458**, 1001 (2009)
- [29] W. H. Louisell, Coupled mode and parametric electronics, Wiley, New York, 1960
- [30] D. Rugar and P. Grutter. Mechanical parametric amplification and thermomechanical noise squeezing. *Phys. Rev. Lett.* **67**, 699 (1991)
- [31] D. W. Carr, S. Evoy, L. Sekaric, H. G. Craighead and J. M. Parpia. Parametric amplification in a torsional microresonator. *Appl. Phys. Lett.* **77**, 1545 (2000)

- [32] I. Mahboob and H. Yamaguchi. Parametrically pumped ultrahigh Q electromechanical resonator. *Appl. Phys. Lett.* **92**, 253109 (2008)
- [33] R. B. Karabalin, X. L. Feng and M. L. Roukes. Parametric nanomechanical amplification at very high frequency. *Nano Lett.* **9**, 3116 (2009)
- [34] Junho Suh, Matthew D. Lahayer, Pierre M. Echternach, Keith C. Schwab and Michael L. Roukes. Parametric amplification and back-action noise squeezing by a qubit-coupled nanoresonator. *Nano Lett.* **10**, 3990 (2010)
- [35] Alexander Eichler, Julien Chaste, Joel Moser and Adrian Bachtold. Parametric amplification and self-oscillation in a nanotube mechanical resonator. *Nano Lett.* **11**, 2699 (2011)
- [36] H. J. Kimble, Benjamin L. Lev and Jun Ye. Optical interferometers with reduced sensitivity to thermal noise. *Phys. Rev. Lett.* **101**, 260602 (2008)
- [37] J. M. Dobrindt and T. J. Kippenberg. Theoretical analysis of mechanical displacement measurement using a multiple cavity mode transducer. *Phys. Rev. Lett.* **104**, 033901 (2010)
- [38] Robert B. Reichenbach, Maxim Alalutdinov, Keith L. Aubin, Richard Rand, Brian H. Houston, Jeevak M. Parpia and Harold G. Craighead. *J. Microelectromech. S.* **14**, 1244 (2005)
- [39] I. Mahboob, K. Nishiguchi, H. Okamoto and H. Yamaguchi. Phonon-cavity electromechanics. *Nature Phys.* **8**, 387 (2012)
- [40] Seung Bo Shim, June Sang Chun, Seok Won Kang, Sung Wan Cho, Sung Woon Cho, Yun Daniel Park, Pritiraj Mohanty, Nam Kim and Jinhee Kim. Micromechanical resonators fabricated from lattice-matched and

- etch-selective GaAs/InGaP/gAaS heterostructures. *Appl. Phys. Lett.* **91**, 133505 (2007)
- [41] Jason M. Gray, Kris A. Bertness, Norman A. Sanford and Charles T. Rogers. Low-frequency noise in gallium nitride nanowire mechanical resonators. *Appl. Phys. Lett.* **101**, 233115 (2012)
- [42] H. X. Tang, X. M. H. Huang, M. L. Roukes, M. Bichler and W. Wegscheider. Two-dimensional electron-gas actuation and transduction for GaAs nanoelectromechanical systems. *Appl. Phys. Lett.* **81**, 3879 (2002)
- [43] Anthony Ayari, Pascal Vincent, Sorin Perisanu, May Choueib, Vincent Gouttenoire, Mikhael Bechelany, David Cormu and Stephen T. Purcell. Self-oscillations in field emission nanowire mechanical resonators : A nanometric dc-ac conversion. *Nano Lett.* **7**, 2252 (2007)
- [44] Young Duck Kim, Kwang Heo, Myung Rae Cho, Sungwan Cho, Duhee Yoon, Hyeonsik Cheong, Jikang Jian, Seunghun Hong and Yun Daniel Park. Determination of Mechanical Properties of Single-Crystal CdS Nanowires from Dynamic Flexural Measurements of Nanowire Mechanical Resonators. *Appl. Phys. Express* **4**, 065004 (2011)
- [45] Vera Sazonova, Yuval Yaish, Hande Ustunel, David Roundry, Tomas A. Arias and Paul L. McEuen. *Science* **431**, 284 (2004)
- [46] J. Scott Bunch, Arend M. van der Zand, Scott S. Verbridge, Ian W. Frank, David M. Tanenbaum, Jeevak M. Parpia, Harold G. Craighead and Paul L. McEuen. Electromechanical resonators from graphene sheets. *Science* **315**, 490 (2007)

- [47] P. Ovartchaiyapong, L. M. A. Pascal, B. A. Myers, P. Lauria and . C. Bleszynski Jayich. High quality factor single-crystal diamond mechanical resonators. *Appl. Phys. Lett.* **101**, 163505 (2012)
- [48] Jung Hoon Bak, Young Duck Kim, Seung Sae Hong, Byung Yang Lee, Seung Ran Lee, Jae Hyuk Jang, Miyoung Kim, Kookrin Char, Seunghun Hong and Yun Daniel Park. High-frequency micromechanical resonators from aluminium-carbon nanotube nanolaminates. *Nature Mater.* **7**, 459 (2008)
- [49] F. Hoehne, Yu. A. Pashkin, O. Astafiev, L. Faoro, L. B. Ioffe, Y. Nakamura and J. S. Tsai. . *Phys. Rev. B* **81**, 184112 (2010)
- [50] A. Venkatesan, K. J. Lulla, M. J. Patton, A. D. Armour, C. J. Mellor and J. R. Owers-Bradley. Dissipation in a gold nanomechanical resonator at low temperatures. *J. Low Temp. Phys.* **158**, 685 (2010)
- [51] Benjamin Lassagne, Yury Trakanov, Jari Kinaret, Daniel Garcia-Sanchez, Adrian Bachtold. Coupling mechanics to charge transport in carbon nanotube mechanical resonators. *Science* **325**, 1107 (2009)
- [52] G. A. Steele, A. K. Huttel, M. Poot, H. B. Meerwaldt, L. P. Kouwenhoven, H. S. J. van der Zant. Strong coupling between single-electron tunneling and nanomechanical motion. *Science* **325**, 1103 (2009)
- [53] Dustin Kleckner, William Marshall, Micheiel J. A. de Dood Khodadad Nima Dinyari, Bart-Jan Pors, William T. M. Irvine and Dirk Bouwmeester. High finesse opto-mechanical cavity with a movable thirty-micron-size mirror. *Phys. Rev. Lett.* **96**, 173901 (2006)

- [54] J. G. E. Harris, D. D. Awschalom, F. Matsukura, H. Ohno, K. D. Maranowski and A. C. Gossard. Integrated micromechanical cantilever magnetometry of $\text{Ga}_{1-x}\text{Mn}_x\text{As}$. *Appl. Phys. Lett.* **75**, 1140 (1999)
- [55] Robert G. Knobel and Andrew N. Cleland. Nanometre-scale displacement sensing using a single electron transistor. *Nature* **424**, 291 (2003)
- [56] B. Ilic, H. G. Craighead, S. Krylov, W. Senaratne, C. Ober and P. Neuzil. Attogram detection using nanoelectromechanical oscillators. *J. Appl. Phys.* **95**, 3694 (2004)
- [57] K. L. Ekinici, X. M. H. Huang and M. L. Roukes. Ultrasensitive nanoelectromechanical mass detection. *Appl. Phys. Lett.* **84**, 4469 (2004)
- [58] J. A. Sidles, J. L. Garbini, K. J. Bruland, D. Rugar, O. Zuger, S. Hoen and C. S. Yannoni. Magnetic resonance force microscopy. *Rev. Mod. Phys.* **67**, 249 (1995)
- [59] Thomas Kenny. Nanometer-scale force sensing with MEMS devices. *IEEE SENSORS JOURNAL* **1**, 148 (2001)
- [60] C. L. Degen, M. Poggio^{a,b}, H. J. Mamina, C. T. Rettner and D. Rugar. Nanoscale magnetic resonance imaging. *PNAS* **106**, 1313 (2009)
- [61] Peter Aufmuth and Karsten Danzmann. Gravitational wave detectors. *New J. Phys.* **7**, 2 (2005)
- [62] J. L. Arlett, E. B. Myers and M. L. Roukes. Comparative advantages of mechanical biosensors. *Nature Nanotechnol.* **6**, 203 (2011)
- [63] M. D. LaHaye, O. Buu, B. Camarota and K. C. Schwab. Approaching the quantum limit of a nanomechanical resonator. *Science* **304**, 74 (2004)

- [64] Norihiko Nishiguchi. Elastic deformation blockade in a single-electron transistor. *Phys. Rev. B* **68**, 121305(R) (2003)
- [65] E. Buks, E. Segev, S. Zaitsev, B. Abdo and M. P. Blencowe. Quantum nondemolition measurement of discrete Fock states of a nanomechanical resonator. *Eruophys. Lett.* **81**, 10001 (2008)
- [66] M. P. Blencowe and E. Buks. Quantum analysis of a linear dc SQUID mechanical displacement detector. *Phys. Rev. B* **76**, 014511 (2007)
- [67] A. D. Armour, M. P. Blencowe and K. C. Schwab. Entanglement and decoherence of a micromechanical resonator via coupling to a cooper-pair box. *Phys. Rev. Lett.* **88**, 148301 (2002)
- [68] Ying-Dan Wang, K. Semba and H Yamaguchi. Cooling of a micro-mechanical resonator by the back-action of lorentz force. *New J. Phys.* **10**, 043015 (2008)
- [69] F. Xue, Y.D. Wang, Y.X. Liu and F. Nori. Cooling a micro-mechanical beam by coupling it to a transmission line. *Phys. Rev. B* **76**, 205302 (2007)
- [70] A. N. Cleland and M. L. Roukes. Fabrication of high frequency nanometer scale mechanical resonators from bulk Si crystals. *Appl. Phys. Lett.* **69**, 2653 (1996)
- [71] Dustin W. Carr, S. Evoy, L. Sekaric, H. G. Craighead and J. M. Parpia. Measurement of mechanical resonance and losses in nanometer scale silicon wires *Appl. Phys. Lett.* **75**, 920 (1999)
- [72] X. M. H. Huang, C. A. Zorman, M. Mehregany and M. L. Roukes. Nanodevice motion at microwave frequencies. *Nature* **421**, 496 (2003)

- [73] K. Usami, A. Naesby, T. Bagci, B. Melholt Nielsen, J. Liu, S. Stobbe, P. Lodahl and E. S. Polzik. Optical cavity cooling of mechanical modes of a semiconductor nanomembrane. *Nature Phys.* **8**, 168 (2012)
- [74] S. Schmid, K. D. Jensen, K. H. Nielsen and A. Boisen. Damping mechanisms in high- Q micro and nanomechanical string resonators. *Phys. Rev. B* **84**, 165307 (2011)
- [75] Chih-Ming Lin, Yun-Ju Lai, Jin-Chen Hsu, Yung-Yu Chen, Debbie G. Senesky and Albert P. Pisano. High- Q aluminum nitride Lamb wave resonators with biconvex edges. *Appl. Phys. Lett.* **99**, 143501 (2011)
- [76] A. B. Hutchinson, P. A. Truitt, K. C. Schwab, L. Sekaric, J. M. Parpia, H. G. Craighead and J. E. Butler. Dissipation in nanocrystalline-diamond nanomechanical resonators. *Appl. Phys. Lett.* **84**, 972 (2004)
- [77] Edward A. Laird, Fei Pei, Wei Tang, Gary A. Steele and Leo P. Kouwenhoven. A high quality factor carbon nanotube mechanical resonator at 39 GHz. *Nano Lett.* **12**, 193 (2012)
- [78] Changyao Chen, Sami Rosenblatt, Kirill I. Bolotin, William Kalb, Philip Kim, Ioannis Kymissis, Horst L. Stormer, Tony F. Heinz and James Hone. Performance of monolayer graphene nanomechanical resonators with electrical readout. *Nature Nanotechnol.* **4**, 861 (2009)
- [79] A. Eichler, J. Moser, J. Chaste, M. Zdrojek, I. Wilson-Rae and A. Bachtold. Nonlinear damping in mechanical resonators made from carbon nanotubes and graphene. *Nature Nanotechnol.* **6**, 339 (2011)
- [80] Andrew N. Cleland. *Foundations of nanomechanics : from solid-state theory to device applications*. Springer, Berlin ; New York, 2003

- [81] Yakov Greenberg, Yurii A. Pashkin and Evgenii Ilichev. Nanomechanical resonators. *Phys.-Usp.* **55**, 382 (2012)
- [82] A. Bokaian. Natural frequencies of beam under tensile axial loads. *J. Sound. Vib.* **142**, 481 (1990)
- [83] Seong Chan Jun, X. M. H. Huang, M Manolidis, C. A. Zorman, M Mehregany and J Hone. Electrothermal tuning of AlSiC nanomechanical resonators. *Nanotechnology* **17**, 1506 (2006)
- [84] D. J. Wilson, C. A. Regal, S. B. Papp and H. J. Kimble. Cavity Optomechanics with Stoichiometric SiN Films. *Phys. Rev. Lett.* **103**, 207204 (2009)
- [85] S. Timoshenko. *Vibration problems in engineering*. Wolfender Press, 2nd reprinti edition (March 15, 2007)
- [86] Sungwan Cho, Myung Rae Cho, Seung-Bo Shim, and Yun Daniel Park. Electrical field gradient pumping of parametric oscillation in a high-frequency nanoelectromechanical resonator. *Jpn. J. Appl. Phys.* **51**, 074003 (2011)
- [87] Bianca E. N. Keeler, Dustin W. Carr, John P. Sullivan, Thomas A. Friedmann and Joel R. Wendt. Experimental demonstration of a laterally deformable optical nanoelectromechanical system grating transducer. *Opt. Lett.* **29**, 1182 (2004)
- [88] N. O. Azak, M. Y. Shagam, D. M. Karabacak, K. L. Ekinici, D. H. Kim and D. Y. Jang. Nanomechanical displacement detection using fiber-optic interferometry. *Appl. Phys.Lett.* **91**, 093112 (2007)

- [89] Bahaa E. A. Saleh and Malvin C. Teich. *Fundamentals of photonics, 2nd edition*. Wiley-Interscience, 2007
- [90] Herbert R. Philipp. Optical properties of silicon nitride. *J. Electrochem. Soc. : Solid-State Science and Technology* **120**, 295 (1973)
- [91] Detector selection guide. webpage of Menlo Systems(<http://www.menlosystems.com>)
- [92] Chung-Chiang Wu and Zhaohui Zhong. Parametric amplification in single-walled carbon nanotube nanoelectromechanical resonators. *Appl. Phys. Lett.* **99**, 083110 (2011)
- [93] T. Beckmann, H. Linnenbank, H. Steigerwald, B. Sturman, D. Haertle, K. Buse and I. Breunig. Highly tunable low-threshold optical parametric oscillation in radially poled whispering gallery resonators. *Phys. Rev. Lett.* **106**, 143903 (2011)
- [94] Daniel Midtvedt, Yury Tarakanov and Jari Kinaret. Parametric Resonance in nanoelectromechanical single electron transistors. *Nano Lett.* **11**, 1439 (2011)
- [95] A. Sampathkumar, T. W. Murray and K. L. Ekinci. Photothermal operation of high frequency nanoelectromechanical systems. *Appl. Phys. Lett.* **88**, 223104 (2006)
- [96] J. D. Thompson, B. M. Zwickl, A. M. Jayich, Florian Marquardt, S. M. Girvin and J. G. E. Harris. Strong dispersive coupling of a high-finesse cavity to a micromechanical membrane. *Nature* **452**, 72 (2008)
- [97] R. Lifshitz, M. Cross. *Reviews of nonlinear dynamics and complexity*. Wiley-VCH, 2008

- [98] A. Erbe, C. Weiss, W. Zwerger and R. H. Blick. Nanomechanical resonator shuttling single electrons at radio frequencies. *Phys. Rev. Lett.* **87**, 096106 (2001)
- [99] D. R. Koenig and E. M. Weig. Voltage-sustained self-oscillation of a nanomechanical electron shuttle. *Appl. Phys. Lett.* **101**, 213111 (2012)
- [100] Y. Hadjar, P. F. Cohadon, C. G. Aminoff, M. Pinard and A. Heidmann. High-sensitivity optical measurement of mechanical Brownian motion. *Europhys. Lett.* **75**, 545 (1999)
- [101] Yuichi Yuasa, Atsushi Yoshinaka, Takayuki Arie and Seiji Akita. Visualization of vibrating cantilevered multilayer graphene mechanical oscillator. *Appl. Phys. Express* **4**, 115103 (2011)
- [102] Yoav Linzon, Daniel J. Joe, Bojan Ilic, Juraj Topolancik, Jeevak M. Parpia, Harold G. Craighead and Slava Krylov. Synchronous imaging for rapid visualization of complex vibration profiles in electromechanical microresonators. *J. Appl. Phys* **111**, 023507 (2012)
- [103] Javier Tamayo, Valerio Pini, Priscila Kosaka, Nicolas F Martinez, Oscar Ahumada and Montserrat Calleja. Imaging the surface stress and vibration modes of a microcantilever by laser beam deflection microscopy. *Nanotechnology* **23**, 315501 (2012)
- [104] D. Garcia-Sanchez, A. San Paulo, M. J. Esplandiu, F. Perez-Murano, L. Forr, A. Aguasca and A. Bachtold. Mechanical Detection of Carbon Nanotube Resonator Vibrations. *Phys. Rev. Lett.* **99**, 085501 (2007)
- [105] Daniel Garcia-Sanchez, Arend M. van der Zande, A. San Paulo, B. Lassagne, Paul L. McEuen and Adrian Bachtold. Imaging Mechanical Vibrations in Suspended Graphene Sheets. *Nano Lett.* **8**, 1399 (2008)

- [106] Quirin P. Unterreithmeier, Thomas Faust, Stephan Manus and Jorg P. Kotthaus. On-chip interferometric detection of nanomechanical motion. *Nano Lett.* **10**, 887 (2010)
- [107] A. N. Cleland and M. L. Roukes. Noise processes in nanomechanical resonators. *J. Appl. Phys.* **92**, 2578 (2002)
- [108] H. G. Dehmelt. Entropy reduction by motional sideband excitation. *Nature* **262**, 777 (1976)
- [109] D. J. Wineland and W. M. Itano. Laser cooling of atoms. *Phys. Rev. A* **20**, 1521 (1979)
- [110] F. Diedrich, J. C. Bergquist, W. M. Itano and D. Wineland. Laser cooling to the zero-point energy of motion. *Phys. Rev. Lett* **62**, 403 (1989)
- [111] C. Monroe, D. M. Meekhof, B. E. King, S. R. Jefferts, W. M. Itano, D. J. Wineland, and P. Gould . Resolved-sideband raman cooling of a bound atom to the 3D zero-point energy. *Phys. Rev. Lett.* **75**, 4011 (1995)
- [112] Florian Marquardt, Joe P. Chen, A. A. Clerk and S. M. Girvin. Quantum theory of cavity-assisted sideband cooling of mechanical motion. *Phys. Rev. Lett.* **99**, 093902 (2007)
- [113] A. Schliesser, R. Riviere, G. Anetzberger, O. Arcizet and T. J. Kippenberg. Resolved-sideband cooling of a micromechanical oscillator. *Nature Phys.* **4**, 415 (2008)
- [114] Young-Shin Park and Hailin Wang. Resolved-sideband and cryogenic cooling of an optomechanical resonator. *Nature Phys.* **5**, 489 (2009)

- [115] R. Rivière, S. Deleglise, S. Weis, E. Gavartin, O. Arcizet, A. Schliesser and T. J. Kippenberg. Optomechanical sideband cooling of a micromechanical oscillator close to the quantum ground state. *Phys. Rev. A* **83**, 063835 (2011)
- [116] H. J. R. Westra, M. Poot, H. S. J. van der Zant and W. J. Venstra. Non-linear modal interactions in clamped-clamped mechanical resonators. *Phys. Rev. Lett.* **105**, 117205 (2010)
- [117] Warner J. Venstra, Hidde J. R. Westra, and Herre S. J. van der Zant. Q-factor control of a microcantilever by mechanical sideband excitation. *Appl. Phys. Lett.* **99**, 151904 (2011)
- [118] K J Lulla, R B Cousins, A Venkatesan, M J Patton, A D Armour, C J Mellor and J R Owers-Bradley. Nonlinear modal coupling in a high-stress doubly-clamped nanomechanical resonator. *New J. Phys.* **14**, 113040 (14)
- [119] I. Mahboob, K. Nishiguchi, A. Fujiwara and H. Yamaguchi. Phonon lasing in an electromechanical resonator. *Phys. Rev. Lett.* **110**, 127202 (2013)

초 록

나노 역학 진동자와 마이크로 역학 진동자는 나노역학시스템(Nano-Electro-Mechanical System)와 마이크로 역학 시스템(Micro-Electro-Mechanical System)에서 가장 기본적인 요소이며 입력된 신호를 다른 형태의 신호나 물리적인 에너지 형태로 변환시키는 역할을 한다. 높은 역학적 품질 인자(Q)를 가진 역학적 진동자는 외부 자극에 대해 민감하게 반응할 수 있으면 전환 과정에서 손실되는 에너지를 줄일 수 있는 장점이 있다. 이러한 높은 품질 인자를 가진 역학적 진동자를 구현하기 위해, 내부 응력을 가진 규소 질화물에 대한 관심이 증가되어 왔으며 이러한 내부 응력은 1 기가 파스칼을 넘어서는 수준에 도달하게 되었다. 이러한 높은 역학적 응력은 역학적 진동자의 진동수를 기존의 규소 기반 역학적 진동자나 역학적 응력이 작은 진동자에 비해 높일 수 있게 되었다. 그리고 역학적 진동자의 움직임, 외부의 자극이나 추가적인 시호를 제외한 상태에서 높은 품질 인자를 가진 상태로 측정하기 위해 광학적 측정 방법이 사용되었다. 본 논문에서는 우선, 일반적인 반도체 공정 법을 이용하여 만들어진 자가 현수 형식의 끝단 고정형 역학적 진동자와 정사각형 박막 형태의 진동자의 움직임을 광학적으로 측정한 결과를 제시한다. 이러한 끝단 고정형 역학적 진동자와 정사각형 박막 역학 진동자는 전기장 기울임 방법을 이용하여 거동하였다. 광학적 방법을 이용한 측정의 세기를 높이기 위해 파라메트릭 증폭 방법을 이용한 역학적 진동자의 거동 증폭 방법이 사용되었다. 역학적 진동자의 공명진동수와 그 진동수의 2배에 해당하는 신호를 함께 소자에 가함으로서, 외부적인 신호의 증폭 없이도 역학적인 거동 자체가 증가하는 현상을 관찰할 수 있었다. 향상된 광학적 측정법과 전기적인 측정법을 이용하여, 역학적 진동자가 외부의 전기적인 자극 없이 열적인 자극에 의해 움직이는 열-자기진동 현상을 관찰 하였다. 이러한 열-자기진동 현상의 진동수 관측과 함께 측정 세기를

역학적 진동자의 형태와 결합 함으로서 역학적 진동자의 열-자기진동 현상에 의한 모드의 형태를 재현할 수 있었다. 아울러 red-detuned sideband와 blue-detuned sideband 를 이용하여 첫 번째 역학적 진동 모드와 두 번째 역학적 진동모드간 상호 결합 현상 및 진동의 조절 현상을 관찰할 수 있었다.

주요어 : 마이크로역학진동자, 나노역학진동자, 광학적 측정법, 파라메트릭 증폭현상, 열-자기진동 현상, 역학적인 옆 주파수

학 번 : 2008-30121